Passive and Active Fiber Laser Array Beam Combining

by
Wei-Zung Chang

A dissertation submitted in partial fulfillment
of the requirements for the degree of
Doctor of Philosophy
(Electrical Engineering)
in The University of Michigan
2012

Doctoral Committee:

Professor Almantas Galvanauskas, Chair
Professor Karl M. Krushelnick
Professor Duncan G. Steel
Professor Herbert G. Winful

DEDICATION

To my family and friends

ACKNOWLEDGEMENTS

At this moment when I am writing this ACKNOWLEDGEMENTS section, all I feel is full of appreciation to those who give me so much support and love during my Ph.D. study in Ann Arbor.

First, I would like to express appreciation to my advisor, Prof. Almantas Galvanauskas, for academic guidance in fiber laser field.

Second, I would like to express gratitude to all the committee members: Prof. Karl Krushelnick, Prof. Duncan Steel, and Prof. Herbert Winful for contributing precious time to provide feedback regarding my research and thesis.

Third, I would like to thank Prof. Ted Norris' classes: Classical Optics & Ultrafast Optics; Prof. Almantas Galvanauskas' classes: Optical Wave in Crystals & Photonic Crystals; Prof. Duncan Steel's classes: Quantum Mechanics I & II; and Prof. Herbert Winful's class: Nonlinear Optics for strengthening my background of optics.

Fourth, I would like to acknowledge Dr. Tsai-Wei Wu's cooperation with passive beam combining project and Dr. Leo Siiman & Tong Zhou's company for pulse coherent combining and pulse synthesis projects.

Fifth, I am indebted to Chao Zhang, Dr. Chi-Hung Liu, Cheng Zhu, I-Ning Hu, Dr. Matthew Rever, Dr. Shenghong Huang, Michael Haines, Alex Kaplan, Max Himmel, Dr.

Kai-Chung Hou, Dr. Michael Swan, Dr. Xiuquan Ma, and Caglar Yavuz for all the help in the lab and effective discussion in research.

Sixth, I am obliged to Wayne Gray, George Tsai, Marvin Eisenberg, Warren Manning, Mitsunobu Umeda, Richardo Yi, Kok-Heng Chong, Abhishek Aphale, Jefferson Timacdog, John Coleman, Irwin Salim, Dennis Deng, Drew Pilarski, Stephen Reynolds, and many others for their friendship.

Finally, I am thankful for my family's unconditional love and endless support as well as Buddha's enlightenment that gives me the wisdom to pass through the most difficult time. Om Mani Padme Hum!

TABLE OF CONTENTS

LIST OF FIGURES

LIST OF TABLES

CHAPTER 1

Introduction

Generation of high power and high peak-intensity laser beams has always been one of the main avenues for developing laser technology. In a number of emerging applications such as laser-driven wake-field acceleration, X-ray, γ-ray, electron and proton beam generation resulting from laser-matter interactions in the relativistic regime, both high intensities of greater than 10^{18} W/cm^2 [1-2] and, simultaneously, very high multi-kW average powers are needed for their practical use. Existing high peak power lasers cannot provide with a combination of both these requirements, because of their low average power (<100 W), low repetition rate (<0.1 Hz) and low efficiency (~1% electrical-to-optical efficiency). To achieve such performance, a novel laser concept known as CAN for Coherent Amplification Network based on fiber amplifiers was proposed to achieve simultaneously high peak and high average powers while exhibiting high efficiency (>30%) [3-4].

Although today's single-mode fiber lasers have reached 10 kW of average power (IPG Photonics), short-pulse (sub-nanosecond regime) energies are limited to ~1 mJ range. Energy of these short pulses is limited by nonlinearity (SRS, SBS, SPM, FWM), while energies of longer, multi-nanosecond pulses is limited by the saturation fluence (~50 J/cm^2), and the fiber dielectric breakdown fluence (~50 J/cm^2). Since high intensity

applications especially in the relativistic regime need each single pulse energy on the order of 1 J in a sub-picosecond regime to reach intensity of 10^{18} W/cm^2 or higher, this condition indicates the coherent combination of N=10^3 fibers where each one will contribute ~1 mJ at 10 kHz, i.e. 10 W, making the entire bundle to be 10 kW [3].

Coherent combination can also be implemented by solid-state lasers. However, consider the world's largest, most complex optical system, the 192-beam National Ignition Facility (NIF) laser that requires complicated free-space alignment for precision and gigantic space for housing (~150 m x 90 m) [5], it would be extremely difficult to coherently combine, for instance, 1000 similar solid-state lasers due to complexity and space requirements. In contrast, fiber lasers exhibit monolithic integration, compactness, as well as other unparalleled characteristics such as superior efficiency, robustness, thermal management (high surface-to-volume ratio), beam quality (single-mode), and cost, making them a better choice for scaling to large combining number. This is the rationale behind the ambitious CAN system to be built using fiber amplifiers and to address the importance on developing coherent beam combining techniques for huge fiber array sizes, particularly in the femtosecond regime.

Fiber laser array beam combining has been studied since 1990s [6] and focused mainly on finding the scalable architectures with high combining efficiency and high brightness to achieve high average power in the continuous-wave regime. For years, many approaches have been developed such as incoherent beam combining, wavelength beam combining, and coherent beam combining [7]. In this thesis, we explore coherent beam combining (CBC). CBC is characterized into two types: One is active CBC in which electronic feedback is used to control the phases of the individual channels so they are all

in phase at the output. The other is passive CBC in which the array is composed of channels with different optical path lengths and forms a composite Michelson interferometric resonator to interfere the longitudinal modes from each channel. Then the array self-adjusts to select the coincident modes (supermodes) with the minimal loss within the gain bandwidth of the array channels to coherently combine all the power of individual channels.

The latest progress of active CBC has demonstrated 5-channel ~2-kW combined power with 79% combining efficiency and near-diffraction-limited beam quality (M^2=1.1) using a diffractive optical element combiner [8]. However, to ensure all output beams will coherently combine to produce a beat frequency, which is required for calculating feedback to the path length adjustors, the coherence length of each fiber output must be longer than the path difference between fibers. This physical criterion imposes the requirement of narrow linewidth (typically a few GHz), which lowers the threshold of stimulated Brillouin scattering (SBS) and therefore reduces the power output of each fiber. On the other hand, passive CBC uses inexpensive broadband non-PM fiber amplifiers, making it possible to reach even higher combined power than active one. Moreover, passive CBC is technologically attractive since it does not require any active phase-control of parallel channels in the array and, therefore, could potentially lead to much simpler coherently self-locked fiber arrays. However, due to limited experimental data [60] and simple theoretical estimates [63-66], the scalability of this approach is still not sufficiently understood and thus requires further exploration.

The exploration of paths towards high power and high intensity lasers constitutes the broad topic of this thesis, in which we address the scalability of passive CBC and

femtosecond pulse coherent combining. To understand the basic physics of coherent combining, we use single-mode fibers for the initial investigations and proof-of-concept demonstrations. We perform this exploration by standard single-mode fiber based systems for the sake of simplifying the procedure, but in high power lasers final amplification stages are built using large-core single-mode fibers such as chirally-coupled-core (CCC) fiber developed in our lab.

The research achievements in this thesis are summarized as follows: For passive CBC, we explore, by means of experiments and simulation, the power of combining efficiency and power fluctuation of coherently phased up to 16-channel fiber-laser arrays with a 2-channel building block using fused 50:50 couplers. The measured evolution of power combining efficiency with array size agrees with simulation based on a new propagation model, which is developed in collaboration with Prof. H. Winful group. For our particular system the power fluctuations due to small wavelength-scale length variations are seen to scale with array size as N^3. Beat spectra investigation supports the notion that a lack of coherently-combined supermodes in arrays of increasing size leads to a decrease in combined-power efficiency.

For pulsed coherent combining, we report on femtosecond pulse coherent combining with up to four parallel fiber amplifier channels. Active phase locking is implemented using the LOCSET single detector feedback technique. We achieve good combining efficiency and negligible distortions in the combined pulses. Theoretical analysis of temporal amplitude and phase errors shows that multi-channel pulse combining with LOCSET feedback is scalable to larger numbers of channels.

Using the established 4-channel pulse coherent combining experimental test bed, we demonstrate femtosecond pulse simultaneous combining and synthesis by coherently spectrally combining 3 fiber chirped pulse amplifiers. We explore different phase-feedback strategies using linear detection schemes when sufficient partial spectral overlap is present, and using two-photon-absorption detector when this spectral overlap becomes vanishingly small. This demonstration shows a path towards simultaneous power scaling and pulse shape and spectral shape control in coherently-combined femtosecond-pulse laser arrays. For example, this could be used to overcome gain narrowing effects in a rare-earth doped fiber amplifier.

In this thesis, the layout of each chapter is followed by the style of *Optics Express* for publications and its detail is elucidated in the following order:

Chapters 2 and 3 [9,10] cover a new multiple-longitudinal-mode numerical modeling that resembles the real experimental conditions for analyzing the scalability issue as well as evaluating the nonlinear effect on combining efficiency.

Chapter 4 [11] describes systematic experimental studies regarding the scalability up to 16 channels, accompanied by the power fluctuation and the evolution of supermodes. Simulation results are also provided to support the consistency with experiments.

Chapter 5 [12] includes a thorough experimental investigation on femtosecond pulse coherent combining up to 4 channels from the scalable architecture, the active phase control, the locking time, and the effect of phase modulation amplitude on combining efficiency. An analytical formula for combining efficiency in terms of combining number, power amplitude, phase difference, and phase modulation depth is also derived to generalize the scalability of arbitrary channel number.

Chapter 6 [13] comprises a new idea to overcome the gain narrowing effect in a single fiber amplifier under a scalable architecture. The phase locking strategies and combining efficiency are addressed conceptually and the proof-of-principle pulse synthesis by coherently combining 3 distinct spectral slices is experimentally demonstrated via partial spectral overlap using a linear detector or no spectral overlap using a TPA detector. The features between these two methods are compared and discussed.

Chapter 7 provides the brief summary of overall work and some advice for future work.

CHAPTER 2

Model for Passive Coherent Beam Combining in Fiber Laser Arrays

2.1 Introduction

There is much current interest in scaling up the output power of a single fiber laser by coherently combining the fields of several amplifying fibers into a high-brightness, diffraction-limited beam [14-19]. One approach that has been pursued with some success is the use of discrete 50:50 directional couplers to create an interferometric system of coupled amplifier pairs in a composite cavity. This pair-wise combining scheme forms the basis of a tree architecture that can, in principle, be scaled up to any even number 2x*N* of fiber lasers. Several groups have demonstrated highly efficient coherent beam combining using up to eight erbium-doped fiber lasers [15-19].

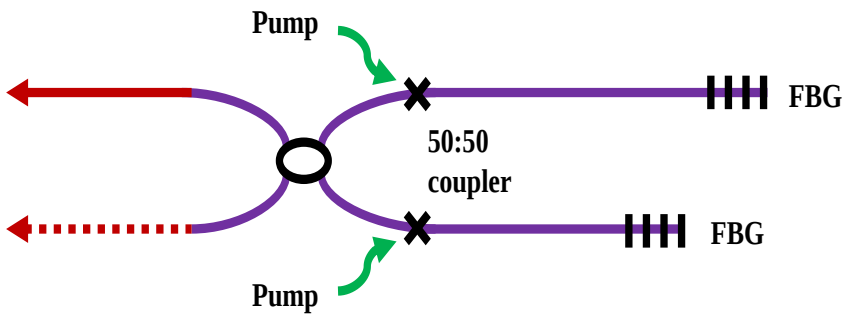

Figure 2.1 A two-channel fiber laser array structure.

In principle, a two-channel fiber laser array is just a Michelson interferometer except that both arms are replaced by rare-earth-doped fibers. The 50:50 directional coupler acts like a beam splitter as shown in Figure 2.1. Constructive or destructive interference occurs depending on the relative phase of the incident fields if their coherence is assumed. The waves generated from the individual active fibers then add on or cancel out with each other accordingly at the coupler outputs. Since uneven fiber lengths directly relate to the accumulated phase difference of the propagating waves, one might suppose that successful beam combination would require accurate control of fiber lengths. However, experimentation has verified the robust and reliable operation of power addition of two-channel fiber laser arrays even when their lengths are not carefully adjusted. Furthermore the combining efficiency has been seen to drop dramatically when the number of fiber amplifiers exceeds eight, thus limiting the scalability of this method.

Several theoretical analyses have been published aimed at explaining the limitation of power scaling and elucidating the nature of the beam combining process [18, 20-26]. These include static calculations of the spectral response of passive multi-arm interferometers [18, 20-23] and dynamic simulations based on iterative maps for the rate equations and a single-longitudinal-mode cavity field [23,24]. Currently there appears to be some debate as to whether the coherent phasing of multiple fiber amplifiers is a "self-organization" process involving coupled nonlinear oscillators [24-26] or the result of an accidental coincidence between the frequency combs of multiple resonators. Any attempt to resolve this debate must take into account the multiple-longitudinal-mode nature of fiber lasers and allow for arbitrary length differences of the amplifying fibers. Yet the

only published dynamic studies include only a single mode, require a fixed phase difference, and yield no spectral information.

Here we present a model based on the amplifying Nonlinear Schrödinger Equation that incorporates the multiple longitudinal modes of a fiber laser and allows for the natural selection of the resonant array modes that experience the minimum loss. It is a propagation model that takes into account gain saturation, fiber nonlinearity, group velocity dispersion, and the loss dispersion of bandwidth limiting elements in the complex cavity. In agreement with experimental observations, the model shows that efficient coherent beam combining occurs without the need for interferometric control of fiber lengths so long as there is sufficient bandwidth available. It is the first model, to the best of our knowledge, that provides detailed spectral information on the output of coherently combined fiber lasers.

2.2 Model and Benchmark

Figure 2.2 depicts two independent single mode fibers coupled discretely by a directional coupler. The continuous-wave pump beams are launched into each fiber by a wavelength division multiplexer (WDM) at $z = 0$ and excite active ions that give rise to gain at longer wavelengths. Assuming single polarization, the coherent waves generated in each amplifying fiber are governed by the nonlinear Schrödinger equation in conjunction with the rate equation for the population inversion [27]

$$\frac{\partial E_j}{\partial z} = \frac{1}{2}\left(g_j - \alpha\right)E_j - \beta_1 \frac{\partial E_j}{\partial t} + \frac{1}{2}(b - i\beta_2)\frac{\partial^2 E_j}{\partial t^2} + i\gamma\left|E_j\right|^2 E_j \tag{2.1}$$

$$\frac{\partial \Delta N_j}{\partial t} = R_p(t) - \frac{\Delta N_j}{\tau} - \frac{\sigma\left|E_j\right|^2}{h\upsilon A_{eff}}\Delta N_j \tag{2.2}$$

$E_j(z,t)$ and ΔN_j refer to the slowly varying envelope of the electric field and the population inversion in the first and second fiber for j = 1,2 respectively. From left to right, the terms in Eq. (1) account for the effects of linear gain $g_j(\Delta N_j)$ fiber losses α, the inverse of the group velocity β_1, the frequency-dependent losses b, the group velocity dispersion β_2, and lastly the nonresonant Kerr nonlinearity γ. As for gain dynamics in Eq. (2), $R_p(t)$ specifies the pumping rate. Its second and third terms describe the process of excited population relaxation with upper-state lifetime τ and laser gain saturation at high intensity fields. The electric field amplitudes are normalized such that $|E_j|^2$ represents power distributions.

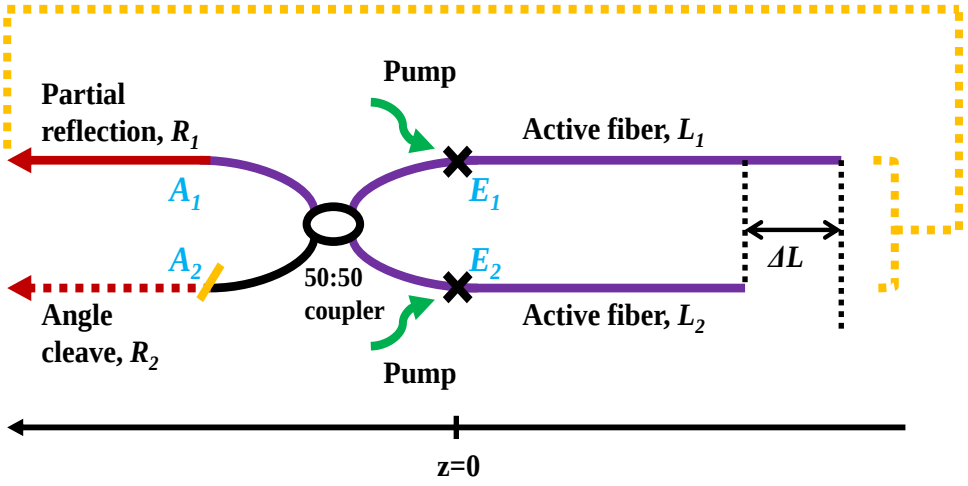

Figure 2.2 A two-channel fiber laser array in the unidirectional configuration.

Note that only forward propagating waves are considered in Fig. 2.2. Because the reflectivity at the output port of fiber laser arrays is typically about 4%, the backward wave is always much weaker than the forward wave and hence standing wave effects as well as cross-saturation by backward waves can be neglected. The unidirectional model describes quite accurately the behavior of a ring fiber laser [27] and is expected to yield useful insight into the beam combining properties of fiber lasers under the high-output

coupling condition. We note that unidirectional fiber laser arrays have also been demonstrated and their phase-locked operation is reported in Refs. [28,29].

The fields exiting the fibers at $z = 0$ pass through the 50:50 directional coupler, which connects the inputs E_1, E_2 and the outputs A_1, A_2 by the linear matrix

$$\begin{pmatrix} A_1 \\ A_2 \end{pmatrix} = \frac{1}{\sqrt{2}} \begin{pmatrix} 1 & -j \\ -j & 1 \end{pmatrix} \begin{pmatrix} E_1 \\ E_2 \end{pmatrix} \tag{2.3}$$

The field A_2 exits the cavity through the angle-cleaved end at the left while 4% of the power in A_1 is split equally and fed back to the fiber inputs at the right as indicated by the yellow dotted line in Fig. 2.2. The remaining 96% serves as the output of that port.

Before verifying the numerical scheme on a single fiber laser as described above, we make a further simplification of the rate equation. Typical roundtrip time for a fiber of tens of meters long is of order hundreds of nanoseconds, while the population relaxation constant is roughly ten milliseconds for Er-doped and one millisecond for Yb-doped fiber lasers. Another important time scale is the gain recovery time, which is also quite long and is of order milliseconds for Er-doped fibers [30-32]. The difference in time scales permits us to solve for the gain dynamics by setting the time derivative in the rate equation to zero. Assuming $P_{sat} = \frac{h\upsilon}{\sigma\tau} \times A_{eff}$, $g_j = 2\sigma\Delta N_j$, and $g_{0j} = 2\sigma R_p(t)\tau$, Eq. (2.2) becomes

$$g_j = \frac{g_{0j}}{\left(1 + \frac{\int_0^T |E_j|^2 dt}{TP_{sat}}\right)} \tag{2.4}$$

where σ is the sum of absorption and emission cross sections and T is the computational time window. Equations (2.1) and (2.4) are integrated numerically and iteratively together with the coupling matrix to model the laser behavior of this composite cavity. In this paper, we adopt standard split-step Fourier methods (SSFM), which have been used

extensively for studying nonlinear pulse propagation in fibers, to handle the multi-longitudinal-mode nature of continuous-wave fiber lasers.

A single 24 m long unidirectional Er-doped fiber laser with 4% power feedback is simulated for the purpose of benchmarking. Table 2-1 lists the parameters and their corresponding values as taken from Ref. [27]. The process of spontaneous emission is represented by very small complex numbers which are generated randomly and incorporated into each roundtrip for initiating the lasing process. Figure 2.3 shows the steady state output power distributions in both temporal (left) and spectral (right) domains for two cases: (a) with a Kerr nonlinearity $\gamma = 0.003$ $W^{-1}m^{-1}$ and (b) with $\gamma = 0$ $W^{-1}m^{-1}$. The time window T is chosen to be eight times the roundtrip duration to ensure dense discretization and higher resolution in the frequency domain. An average of approximately 28 mW power is obtained by $\int_0^T |E_j|^2 dt/T$ for either case. Because the large output coupling coefficient leads to significant amplitude changes along the fiber, the step size parameter of SSFM needs to remain small in order to obtain accurate integrations. Here we choose six or more steps for each roundtrip. Growing out of incoherent random noise, the laser output is characterized by a time-varying output and its spectrum consists of irregular spikes. The irregular time series is the result of the complex beating between a large numbers of longitudinal modes with random phases. The steady states are therefore defined by measuring the average powers between consecutive roundtrips. The shape of the spectral envelope is determined by the loss dispersion. It is evident that the inclusion of the nonlinear refractive index broadens the power spectrum significantly, which was first verified and reported by *Roy et al* for fiber lasers [27]. This is a result of four-wave-mixing which can be approximately phase-

matched because of the dense nature of the longitudinal modes. It is clear that this propagation model should be capable of describing the spectral properties of fiber laser arrays with multiple longitudinal modes.

Table 2-1 Parameters and values

Parameters	Description	Value
λ	wavelength	1.545 μm
n	refractive index	1.5
α	propagation loss	0.058 m^{-1}
g_0	unsaturated gain	2.67 m^{-1}
b	loss dispersion	0.13 ps^2/m
β_2	phase dispersion	-0.003 ps^2/m
T	population relaxation time	10 ms
γ	nonlinear coefficient	0.003 $W^{-1}m^{-1}$
P_{sat}	saturation power	0.6 mW
RT	roundtrip number	2000
$rtsteps$	step number of one roundtrip	6

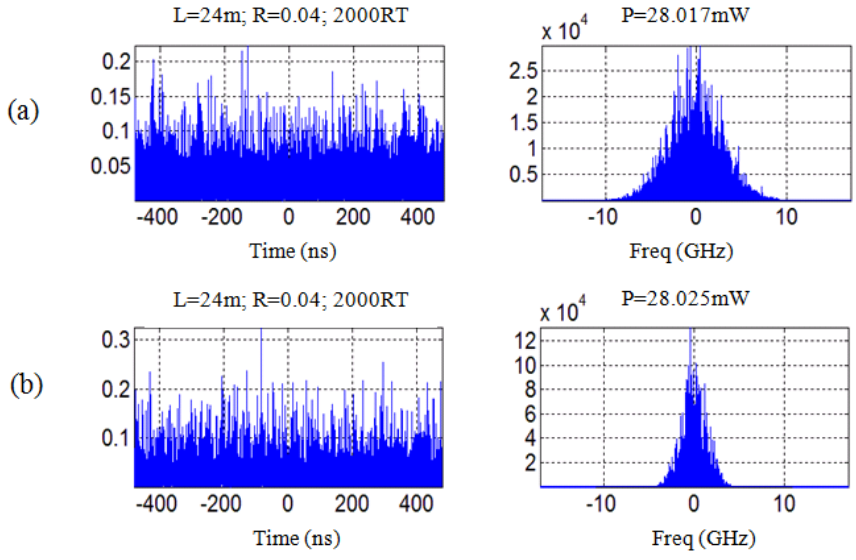

Figure 2.3 Output powers of single Er-doped fiber laser in the time (left) and spectral (right) domains for (a) $\gamma = 0.003\ m^{-1}W^{-1}$ and (b) $\gamma = 0\ m^{-1}W^{-1}$. The power reflectivity is 4% as indicated in the figure.

2.3 Simulation for Two-Channel Fiber Laser Arrays

We begin with a two-channel fiber laser array by setting L_2 to 24.0 m and R_1, R_2 to 4%, and 0% respectively in Fig. 2.2. The length difference ΔL is arbitrarily selected to be 30 cm and hence L_1 equals 24.3 m. Using parameters from Table 2-1, Fig. 2.4 illustrates the simulation results for both temporal (left) and spectral (right) domains. It is interesting to see that essentially all the power, 56.26 mW, emerges from the first output port while very little (less than 0.05 mW) escapes from the other, angle-cleaved, one. (Note the orders-of-magnitude difference in the ordinate scales between Fig. 2.4(a) and (b).) For the efficiency calculations, a simulation of individual fiber lasers of lengths L_1, L_2 and equal 4% output coupling generated 28.27, 28.02 mW respectively. Their sum gives a total power of 56.29 mW and it is used, together with the array output power 56.26 mW, to define the combining efficiency in this paper. Here, the efficiency is high and close to 100%.

A rather striking feature of the array output is the discrete nature of the power spectra compared to the quasi-continuous spectrum displayed by the single fiber laser. While the spectrum of the single laser is made up of the densely packed axial modes of a long cavity, the array resonances in Fig. 2.4 comprise a set of spikes equally separated by an interval of 0.667 GHz. This spectrum is the result of a Vernier effect involving the superposition of the frequency combs of the two coupled cavities with a length mismatch ΔL. For ring cavities it leads to a modulation of the comb spectrum with a beat frequency of $\Delta\upsilon = \frac{c}{n\Delta L}$ Using a refractive index of n = 1.5 and 0.3 m for ΔL, we obtain 0.667 GHz which agrees exactly with the simulation result. For laser arrays with standing wave cavities, the optical path lengths double, so the mode separation becomes $\Delta\upsilon =$

$\frac{c}{n(2\Delta L)}$ [33]. *The Vernier effect results in the suppression of certain longitudinal modes and has been utilized in the Vernier-Michelson cavity to achieve single-frequency operation* for gas lasers [34].

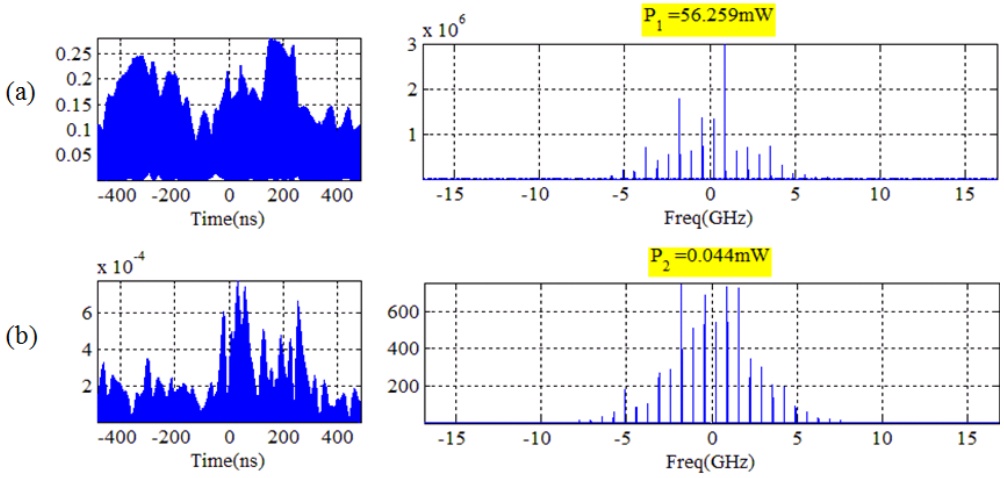

Figure 2.4 A unidirectional Er-doped fiber laser array with L_1 = 24.3 and L_2 = 24.0 m in Fig. 2.2. The output powers from (a) upper port with partial reflectivity and (b) lower, angle-cleaved, port. The separation between spikes is measured to be 0.667 GHz.

To further demonstrate the natural emergence of the array modes and the self-adjustment feature of our model regardless of the length differences, another simulation result is given with all the coefficients fixed as before except that L_1 is changed to 24.08 m, so that ΔL = 8 cm. Since Δv is inversely proportional to ΔL, greater spacing is expected for a smaller length mismatch. Indeed the spectral intervals are measured to be 2.5 GHz in Fig. 2.5(a) and (b), which is consistent with the theoretical calculations. Note also that the main peak in the spectrum has shifted from 0.9074 GHz in Fig. 2.4(a) to -0.1848 GHz in Fig. 2.5(a) as the laser self-adjusts its frequency. This dependence of the beat spectrum on ΔL is routinely seen in experiments [16-19, 29, 33]. Further details of the spectrum can be seen by zooming in on one of the spikes in Fig. 2.5(a) (circled in green). It is seen that the spikes are actually the envelope of the individual cavity axial

modes, which are equally spaced in the absence of the Kerr nonlinearity (Fig. 2.5(c), γ = 0 $W^{-1}m^{-1}$) and somewhat broadened and shifted in the presence of nonlinearity (Fig. 2.5(d), γ = 0.003 $W^{-1}m^{-1}$). The shift of the peak due to nonlinearity is only about 1 MHz at these power levels. We remark that some frequency pulling of the individual modes has been observed in experiments and attributed to nonlinearity [26]. Based on those results the authors suggested that the mechanism for spontaneous self-organization without cavity length control is a nonlinear process (in the sense of requiring an intensity-dependent refractive index). Our results however indicate that this spontaneous self-adjustment occurs even in the absence of nonlinearity as the laser seeks to operate on the lowest loss mode of the composite cavity. The presence of nonlinearity simply leads to a slight modification of the actual mode frequencies but cannot be seen as the fundamental mechanism leading to the coherent phasing of the two amplifying fibers.

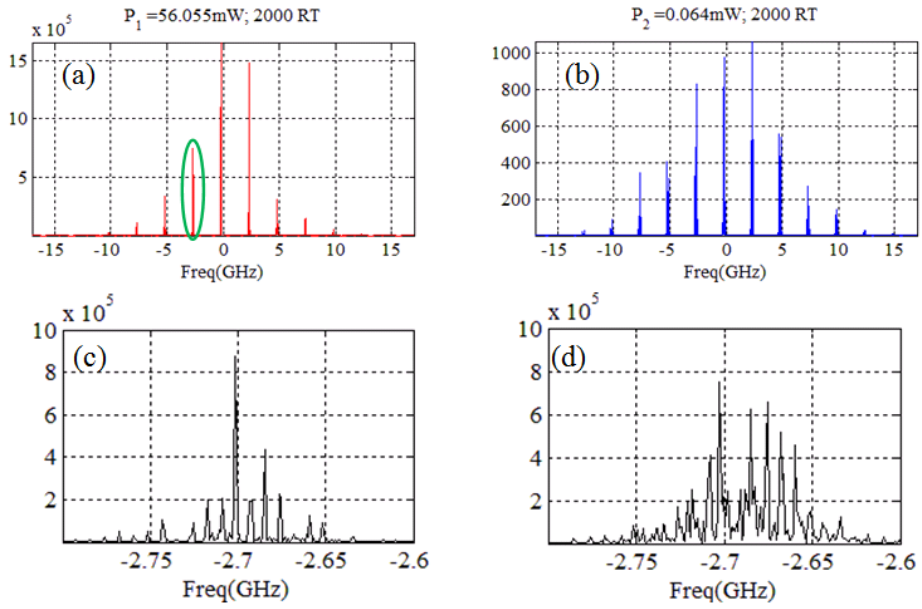

Figure 2.5 Power spectrum of a two-channel fiber laser array with L_1 = 24.08 m and L_2 = 24.0 m. P_1 in (a) refers to the output power from the port of 4% reflectivity, and P_2 (b) is from the angle-cleaved one. The spikes are separated by 2.5 GHz. The spectrum of the green-circled spike of (a) is further zoomed in for (c) linear and (d) nonlinear arrays.

The ability of two lasers to combine efficiently regardless of their length difference is a feature that emerges naturally from our model. It is merely a reflection of the fact that in the presence of a large number of longitudinal modes, the fields self adjust to select a new oscillation that corresponds to a common resonance of the combined cavity [15]. This self-adjustment should be possible so long as there is sufficient bandwidth available to encompass at least one of these composite-cavity modes. In our model, the effect of bandwidth-limiting elements in the cavity is described by the parameter *b.* It represents a frequency-dependent quadratic loss term of the form $-b(\omega - \omega_0)^2$. To investigate the role of available bandwidth in beam-combining efficiency we consider a case where ΔL is small enough that the frequency spans are greater than the limited bandwidth imposed by a filter. First we assume 1 mm for ΔL and set the loss dispersion coefficient to zero. The simulation results are illustrated in Fig. 2.6(a). Note the modulation period is calculated to be 200 GHz. In the absence of bandwidth limiting the fiber lasers combine successfully with an efficiency close to 100%. The first two peaks near the center, pointed out with arrows in Fig. 2.6(a), are measured to be -117.9 GHz (left) and 82.02 GHz (right), the main peak. Again 200 GHz is verified by subtracting -117.9 from 82.02. Next the simulation is repeated with b = 0.13 ps^2m^{-1} which corresponds to a filter with a bandwidth of roughly 60 GHz. Since now higher frequencies experience more losses, only one peak with the least attenuation lases in Fig. 2.6(c) and the sum of P_1 and P_2 is also reduced. The combining efficiency decreases to 76% since there is now only a single mode within the gain bandwidth.

Note that the location of the main peak is now measured to be 55.87 GHz as opposed to 82.02 GHz in Fig. 2.6(b) without bandwidth limiting. In addition, a significant amount

of power, 8.6 mW, appears at the lossy port. The occurrence of the frequency shift and the large output from the angle-cleaved port implies that the array, in the presence of frequency-dependent losses, does not necessarily lase at the cold cavity composite resonances but at frequencies that minimize the overall cavity losses. It shows that the model, just like actual fiber laser arrays, does adjust itself and select the suitable resonant frequencies.

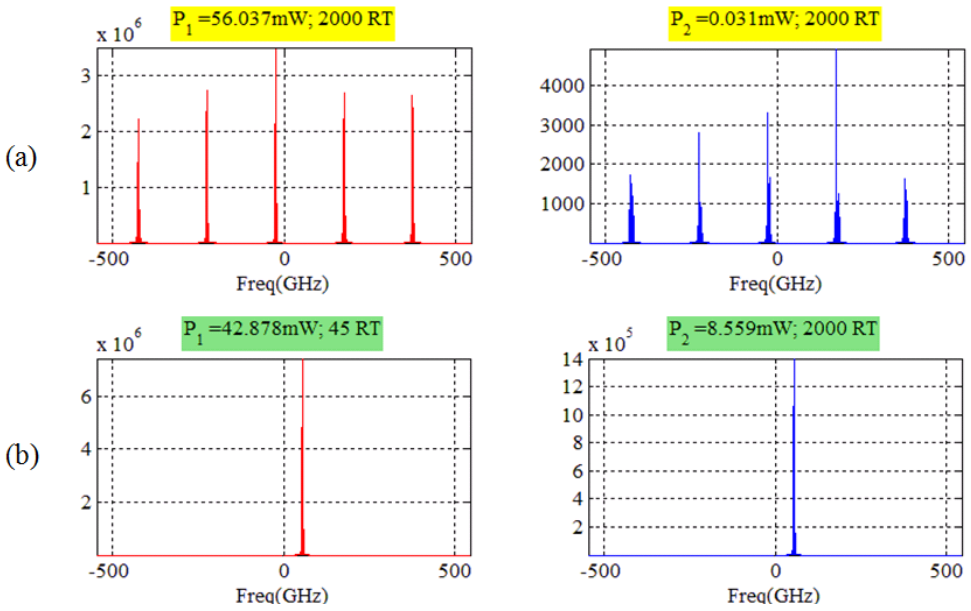

Figure 2.6 Er-doped fiber laser arrays configured in Fig. 2.2 with L_1 = 24.001 and L_2 = 24.0 m. The computation window in frequency domain covers more than 1 THz. The left plots refer to the output powers from the port with partial reflectivity, while the right ones show the other, angle-cleaved, one. No frequency-dependent losses are applied for (a) and *b* equals 0.13 ps^2m^{-1} in (b).

The final example given for two-channel fiber laser arrays is to examine the fine structure of the spectrum of amplified spontaneous emission for operation below threshold. Using realistic parameters from the experiment of Shirakawa *et al* [16], the simulation results are illustrated in Fig. 2.7(a) with 12.682, 12.0 m for L_1 and L_2 respectively. Note that we double the fiber lengths since our model is based on the ring cavity configuration. The carrier wavelength is kept at 1.545 μm and the refractive index

n is 1.45. The lasing threshold $g_{th} = \alpha - ln(R)\,/L$ is calculated to be 0.312 m^{-1}. We set g_0 to 0.31 m^{-1} and the amplified spontaneous emissions spectrum from the first port agrees qualitatively with that of the experimental results [16] shown in Fig. 2.7(b). As in the experiment, the spectral packets are separated by about 302 MHz. Unlike the very narrow spectral packets (essentially spikes) in the previous plots where arrays are pumped above the threshold, they exhibit broader FWHM's here and are seen clearly to comprise of small spikes separated by a free spectral range of 16.3 MHz. As for the second port, its spectrum is more complicated and features a split pattern around the peaks of the resonances. The spectra at the two ports are complementary in a manner similar to the reflection and transmission spectra of a Fabry-Perot. (For the second port the experimental spectrum of Ref. [16] has some similarities to the theoretical one but is complicated by the presence of features attributed to the presence of an extraneous polarization component.) As the pump power increases the spectral packets are seen to narrow as shown in Fig. 2.7(c). This is a result of gain narrowing due to our assumption of homogeneous broadening in which most longitudinal modes are suppressed as a result of serious competition between adjacent frequencies.

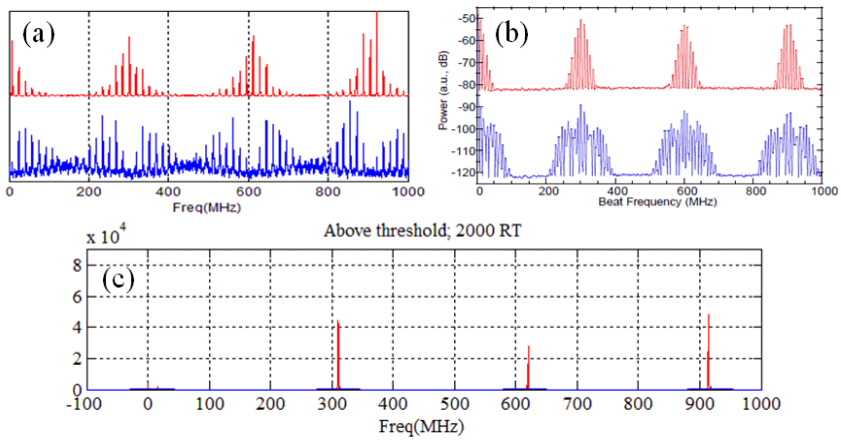

Figure 2.7 Fig. 7. Beat spectra of amplified spontaneous emission for the higher reflectivity port (red curves) and the zero-reflectivity port (blue curves) an Er-doped fiber laser array with round-trip path length

difference of 0.682 m. (a) Simulation result obtained by averaging the spectrum over 500 consecutive roundtrips (b) Experimental beat spectrum measurement from Ref [16], used with permission. (c) Simulation of spectrum above threshold.

2.4 Simulation for Four-Channel Fiber Laser Arrays

To further demonstrate the capacity of this model, we apply the simulation to a four-channel fiber laser array with randomly chosen lengths of 24.0, 24.3, 23.73, and 24.63 meters. The results are shown in Fig. 2.8. Unlike two-channel arrays where Δυ is determined by the length differences, it is now determined by the greatest common divisor L_{gcd} of the four lengths [35]. In this case, L_{gcd} equals 3 cm and indeed the amplified spontaneous emission spectrum (Fig. 2.8(a)) features a complicated interference pattern with a period of 6.67 GHz calculated from $\Delta\upsilon = \frac{c}{n}/L_{gcd}$ using 1.5 for the refractive index *n*. As the pumping is increased above threshold there is a narrowing of the beat packets. Most of the power, 107.44 mW, emerges from the second output port as seen in Fig. 2.8(b). Since the four uncoupled fiber lasers produce a total of 112.63 mW, the combining efficiency is calculated to be 95.4%.

The reason for the efficiency drop is the decrease in the probability of finding an accidental coincidence in the resonances of mismatched cavities as the number of such cavities increases [20-23]. In the absence of an exact coincidence, which corresponds to a lossless mode, the system still finds the least lossy mode, which will generally have significant energy coupled through the lossy ports because of the residual phase mismatch at the couplers.

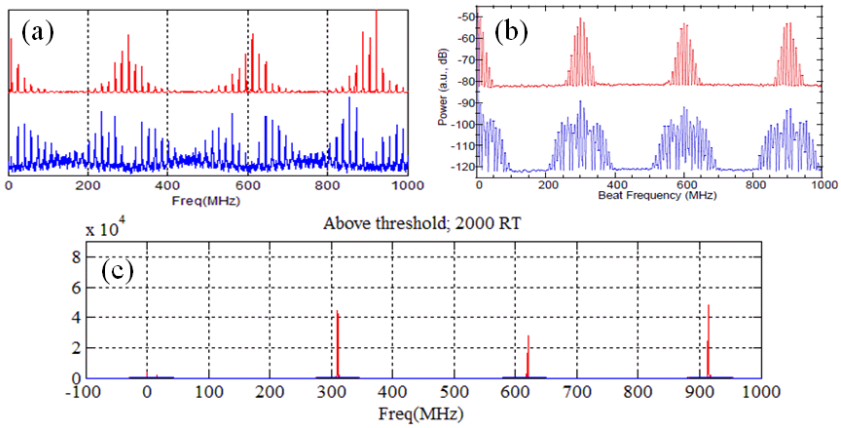

Figure 2.8 Four-channel fiber laser array (a) spectrum of amplified spontaneous emissions with pattern periods measured to be 6.67 GHz. (b) Major output powers in the temporal (left) and spectral (right) domains.

2.5 Discussion and Conclusion

The self-adjustment process that leads to the efficient and robust combining of fiber lasers depends on the existence of a dense set of longitudinal modes from which the laser can select those that satisfy the minimum loss condition at the coupler. In our model, changes in fiber length differences are automatically compensated by changes in the lasing wavelength and the spectral signature of the combined lasers. The spectral changes seen in our simulations agree with experimental observations. We find that at these power levels the non-resonant nonlinear refractive index is not a significant factor in beam combining.

While the simulations presented here involved following the progress of a unidirectional wave as it propagates around a composite cavity, the model is easily extended to include counterpropagating waves as well as different polarizations. Because the solution scheme is the highly efficient split-step Fourier method, the model can be used to simulate the dynamics of many coupled amplifiers.

In conclusion, we have proposed a new model for studying discretely coupled fiber laser arrays. The model incorporates propagation effects, multiple longitudinal modes, unbalanced mirror reflectivities, uncontrolled fiber lengths, the intensity-dependent refractive index, and gain saturation. It lends support to the picture of coherent beam combining as simply the natural selection of the supermodes of a composite cavity that has the lowest loss.

CHAPTER 3

Dynamical Bidirectional Model for Coherent Beam Combining in Passive Fiber Laser Arrays

3.1 Introduction

The possibility of multi-kW power scaling through passive coherent phasing of fiber laser arrays has spurred intense research into the physics and technology of beam combining. Several groups have successfully demonstrated highly efficient coherent combining of up to eight discretely coupled fiber lasers by 50:50 directional couplers [11,36-39]. Theoretical work has addressed various steady state aspects of beam combining, such as the scaling of combining efficiency with array size [40-44]. However there have been few detailed dynamical studies that probe the process in which the independent fiber amplifiers organize themselves to produce a mutually coherent output. We recently presented a theoretical model of fiber laser coherent beam combining that showed clearly that the mechanism of beam combining is the selection of the composite cavity mode that satisfies the condition of minimum loss [9]. In that work a ring cavity was assumed in order to avoid the computational complexities of counter-propagating waves while still gaining insight into the nature of the beam combining process. Although there have been some demonstrations of passive coherent phasing in ring cavity geometries, all the attempts to scale up beyond two coupled lasers have involved standing wave cavities. It

would be desirable to have a simulation tool that permits detailed studies of beam combining with Fabry-Perot cavities.

In this paper we present a full bidirectional model of passive coherent phasing based on mutually-coupled nonlinear Schrödinger equations for counterpropagating waves. These equations are coupled to dynamic rate equations that include the effects of cross saturation by the forward and backward waves. The model allows a detailed look at how the composite cavity modes evolve from noise and how the phase-difference between coupled amplifiers locks to a fixed value. It is evident from the model that the coherent phasing results from the selection of the composite cavity mode with the lowest loss. We show how the spacing between array modes is determined and examine the controversial role of the nonlinear refractive index. Our results yield insight into the mechanisms that limit beam combining efficiency.

3.2 Model

A two-channel fiber laser array is depicted in Fig. 3.1 with two independent single mode fibers coupled discretely by a directional coupler. The continuous-wave pump beams, launched into each fiber by a wavelength division multiplexer (WDM) at $z = 0$, excite active ions and give rise to gain at longer wavelengths. The fiber Bragg gratings (FBG) provide ~100% feedback at the right ends of the fibers, while differential power reflectivities, R_1 and R_2 in Fig. 3.1, are applied to the output ports of the 50:50 coupler at the left-hand sides. Assuming single polarization, the coherent waves propagating in +z and −z directions in each fiber laser are governed by the nonlinear Schrödinger equation together with the rate equation [45,46]:

$$\frac{\partial E_j^f}{\partial z} = \frac{1}{2}(g_j - \alpha)E_j^f - \beta_1 \frac{\partial E_j^f}{\partial t} + \frac{1}{2}(b - i\beta_2)\frac{\partial^2 E_j^f}{\partial t^2} + i\gamma(\left|E_j^f\right|^2 + 2\left|E_j^b\right|^2)E_j^f \tag{3.1}$$

$$\frac{\partial E_j^b}{\partial z} = -\frac{1}{2}(g_j - \alpha)E_j^b + \beta_1 \frac{\partial E_j^b}{\partial t} - \frac{1}{2}(b - i\beta_2)\frac{\partial^2 E_j^b}{\partial t^2} - i\gamma(2\left|E_j^f\right|^2 + \left|E_j^b\right|^2)E_j^b \tag{3.2}$$

$$\tau \frac{dg_j(z,t)}{dt} = g_{0j} - g_j(z,t) - \frac{\left|E_j^f\right|^2 + \left|E_j^b\right|^2}{P_{sat}} g_j(z,t) \tag{3.3}$$

E_j^f and E_j^b refer to the slowly varying envelopes of the forward and backward electromagnetic waves in the first (j = 1) and second (j = 2) fiber respectively. Various effects including linear gain g_j, fiber losses α, the inverse of the group velocity β_1, the frequency-dependent losses b, the group velocity dispersion β_2, and the nonresonant Kerr nonlinearity γ are all incorporated in Eqs. (3.1) and (3.2). In Eq. (3.3) for gain dynamics, g_{0j} specifies the unsaturated gain while the second and third terms respectively describe the process of excited population relaxation with upper-state lifetime τ and laser gain saturation at high intensity fields. We normalize the electric field amplitudes so $\left|E_j\right|^2$ corresponds to the power distribution. Based on the coupled mode theory [47], the 50:50 directional coupler connecting the inputs E_1^b, E_2^b to the outputs A_1, A_2 is represented by a linear matrix.

$$\begin{pmatrix} A_1 \\ A_2 \end{pmatrix} = \frac{1}{\sqrt{2}} \begin{pmatrix} 1 & -j \\ -j & 1 \end{pmatrix} \begin{pmatrix} E_1^b \\ E_2^b \end{pmatrix} \tag{3.4}$$

It is clear that the forward and backward waves are coupled through cross-phase modulation (the last terms in Eqs. (3.1) and (3.2)) as well as by the co-saturation of the gain fields described in Eq. (3.3) [46]. In our previous work on unidirectional fiber laser arrays, straightforward integration by the split step Fourier method (SSFM) was applied since there was no coupling between forward and backward waves to contend with [48]. Here, however the nonlinearly-coupled differential Eqs. (3.1-3.3) require some self-

consistent solutions of E_j^f and E_j^b existing for all $z \in [0, L]$ as well as for all t within the computation window. We handle this complication by using an iterative SSFM [49] such that E_j^f, E_j^b are in turn integrated along +z and –z directions respectively while the information of the updated field is stored and used to compute the other one at a later time. The iteration continues until certain convergences are reached.

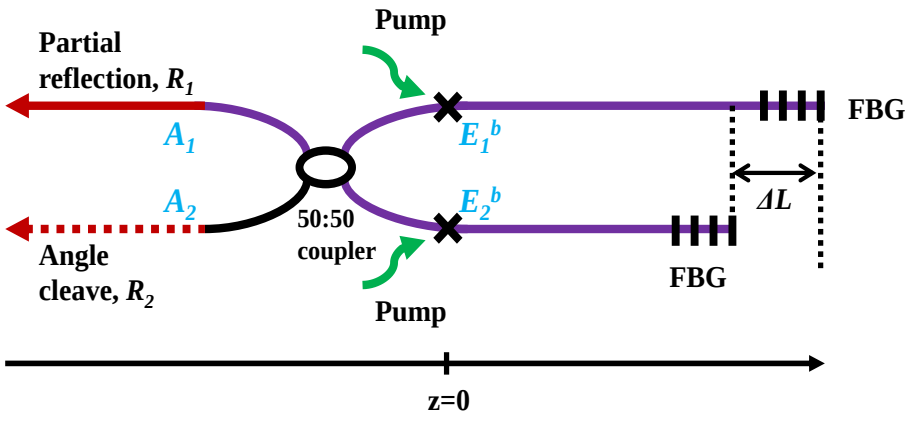

Figure 3.1 A two-channel fiber laser array

In the dynamical aspects of the array, rather than turning on g_j abruptly as assumed in many cases [48,50,51], we allow the gain to build up gradually and retain its dependence on both time and position. Due to the discrete nature of numerical computation, the fiber length is partitioned into segments and we will deal with an integrated gain variable $\tilde{g}_j = \int_{z_0}^{z_0+l} g_j dz$ over each segment instead of $g_j(z,t)$ in Eq. (3.3). The product term involving the gain variable and the intensity field on the right hand side of Eq. (3.3) is, however, difficult to integrate without losing accuracy; we thus follow Ref. [43] in replacing that term in the manner described below.

Based on Beer's law $\frac{d\left|E_j^f\right|^2}{dz} = +g_j\left|E_j^f\right|^2$ and $\frac{d\left|E_j^b\right|^2}{dz} = -g_j\left|E_j^b\right|^2$ the rate equation can be written as

$$\tau\frac{dg_j(z,t)}{dt} = g_{0j} - g_j(z,t) - \frac{1}{P_{sat}}\left(\frac{d\left|E_j^f\right|^2}{dz} - \frac{d\left|E_j^b\right|^2}{dz}\right) \tag{3.5}$$

By integrating g_j along $z \in [z_0, z_0 + l]$ and defining $\tilde{g}_j = \int_{z_0}^{z_0+l} g_j dz$, we find that Eq. (3.5) becomes

$$\begin{aligned}\tau\frac{d\tilde{g}_j(t)}{dt} = \tilde{g}_{0j} - \tilde{g}_j(t) - \frac{1}{P_{sat}}\Big(&\left|E_j^f(z_0+l)\right|^2 - \left|E_j^f(z_0)\right|^2 \\ &- \left|E_j^b(z_0+l)\right| + ^2\left|E_j^b(z_0)\right|^2\Big)\end{aligned} \tag{3.6}$$

Further approximation can be applied with the relation $\left|E_j^f(z_0+l)\right|^2 = e^{\tilde{g}_j(z_0)}\left|E_j^f(z_0)\right|^2$ and $\left|E_j^b(z_0)\right|^2 = e^{\tilde{g}_j(z_0+l)}\left|E_j^b(z_0+l)\right|^2$ for sufficiently small length ℓ. Its substitution into Eq. (3.6) produces the final expression for the rate equation.

$$\begin{aligned}\tau\frac{d\tilde{g}_j(t)}{dt} = \tilde{g}_{0j} - \tilde{g}_j(t) \\ - \frac{1}{P_{sat}}\left[\left|E_j^f(z_0)\right|^2\left(e^{\tilde{g}_j(z_0)} - 1\right) + \left|E_j^b(z_0+l)\right|^2\left(e^{\tilde{g}_j(z_0)} - 1\right)\right]\end{aligned} \tag{3.7}$$

Eqs. (3.1-3.2) and (3.7) are then solved together by iterative SSFM and the Euler method, where the latter is adopted for connecting the integrated gain variable at current and next time incidents, i.e. $\tilde{g}_j$ and $\tilde{g}_j'$ by

$$\tilde{g}_j' = \tilde{g}_j + \frac{d\tilde{g}_j}{dt}\Delta t \tag{3.8}$$

We set the increment step Δt to be four times the roundtrip duration in the simulation since numerical accuracy is ensured when Δt (~1 μs) is much smaller than the population relaxation time constant τ (10 ms). To validate our derivation of the dynamical model, an

example is given for a two-channel fiber laser array of fiber lengths 24.3 and 24.0 m. Here by setting γ=0 $W^{-1}m^{-1}$ the array is assumed to be linear so the nonlinear phases will not modify the distinct modes of the laser cavity [9]. Each of the active fibers is partitioned into 70 segments (*rtstps* = 70.) Other parameter values used are λ_0=1.545 μm, α=0.058 m^{-1}, β_2= -0.003 ps^2m^{-1}, n_1=1.5, b=0.13 ps^2m^{-1}, g_0=2.67 m^{-1} and P_{sat}=0.6 mW.

3.3 Simulation Results

The simulation results are shown in Fig. 3.2 to Fig. 3.4. In addition to the standard SSFM outputs (temporal and spectral domain profiles), the spatial distributions and dynamical evolutions of the array can also be retrieved from our model. The spatial distributions refer to the self-consistent solutions of the coupled equations and they are plotted with red circles in Fig. 3.2 for (a) both forward and backward waves and (b) the gain field within one of the fiber lasers (L_1 =24.3 m) at steady state. It is clear that the backward signal dominates in this efficient backward pumping configuration [52] and the resulting gain exhibits stronger saturation near the front end of the fiber. To verify the numerical solutions of the dynamic equations, the time derivatives and the nonlinear index terms of Eqs. (3.1-3.3) are set to zero since they do not affect the field distributions at steady states. We then solve the simplified ODEs together with the boundary conditions using the built-in BVP (boundary value problems) solver of Matlab. The solid black line represents such solution in Fig 3.2(a),(b) and its agreement with the red circles supports our simulation results. As for array dynamics, the time evolutions of (c) the output power, coming out of the partially-reflected port, and (d) the gain variable (averaged over z) in both fiber lasers are clearly observed in Fig. 3.2. The array exhibits transient oscillations in the beginning of the excitation and settles eventually after a few milliseconds. At

steady state, the averaged gain variables $\bar{g}_{1,2}$ amount to 0.1244 and 0.1251 m^{-1} and these equal the roundtrip losses of $\alpha - \frac{ln(R)}{2L_{1,2}}$ as expected from fundamental laser theory.

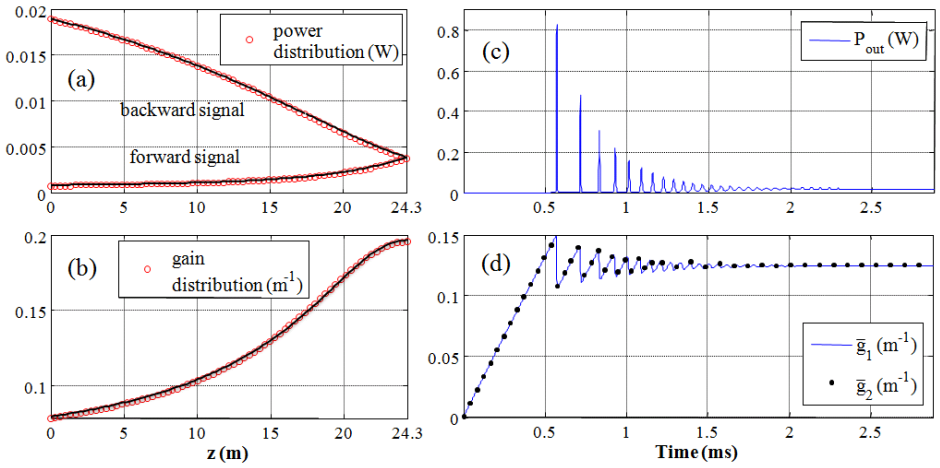

Figure 3.2 The spatial distributions of one of the fiber laser (L1 = 24.3 m) are plotted as an example for (a) both propagating waves and (b) the gain field along the z axis. The three curves consisting of red circles present the self-consistent steady-state solutions obtained from our model, while that of solid black lines are calculated from Matlab with its built-in BVP solver. As for array dynamics, the time evolution of the output power and the averaged gain variable (over z) of each fiber are displayed in (c) and (d). The output power refers to the combined power coming out of the partially-reflected, R1, port as seen in Fig. 3.1.

We now turn to the beam combining properties of the array. The temporal (left) and spectral (right) domain outputs are shown in Fig. 3.3. As expected, almost all the power comes out of the upper, partially reflected (R_1 = 0.04) port, while a negligible amount leaks through the lower, angle-cleaved (R_2 = 0) one. Taking P_{out} as the output of the straight-cleaved end and P_i as the power from the i^{th} single laser if uncoupled, we define the power combining efficiency for an N- channel array as

$$N\text{- channel combined power efficiency} = P_{out} / \sum_1^N P_i$$

The calculated combining efficiency is close to 100% and is consistent with experimental observations and with our previous calculations for unidirectional laser cavities. To understand the role of counterpropagating waves in array combining, we examine the modulated power spectrum in which a series of equi-distant spikes appears

as a result of a Vernier effect relating to the overlap of the frequency combs corresponding to two laser cavities of different length. The modulation period, found to be 0.333 GHz from the spectral plots of Fig. 3.3, is in agreement with the theoretical prediction of $\Delta\nu = c/(2n_1\Delta L)$ [53]. Compared with the $\Delta\upsilon$=0.667 GHz obtained for unidirectional fiber laser arrays of the same parameters [9], the factor of two difference can be readily understood by the fact that the optical path lengths double in the bidirectional configurations and the period halves accordingly. The simulation results suggest that, besides giving rise to additional phases through propagation, the backward waves merely serve to co-saturate the population inversion and they do not influence the coherent combining mechanism, in which the key component is the multilongitudinal modes of fiber lasers. The pseudo-random shape of the temporal profiles in Fig. 3.3 is the result of the complex beating between the many modes.

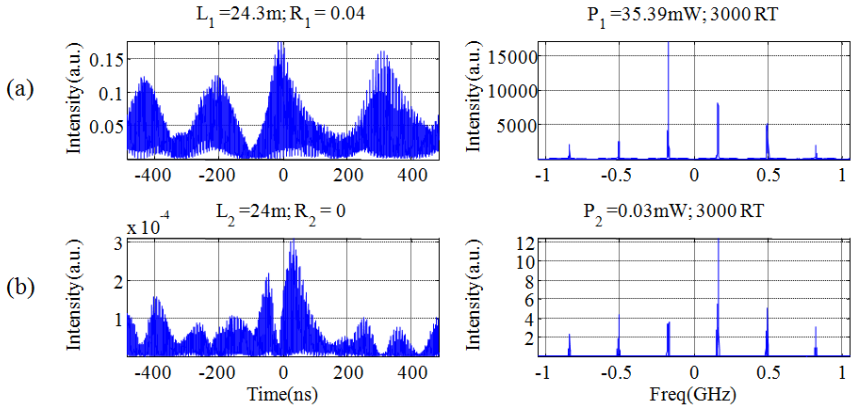

Figure 3.3 An Er-doped fiber laser array in Fig. 3.1 with L_1 24.3 and L_2 24.0 m. The output powers from (a) upper port with partial reflectivity and (b) lower, angle-cleaved, port are plotted for time (left) and frequency (right) domains respectively. The separation between spikes in the frequency domain is 0.333 GHz.

To fully characterize the array dynamics, the model is used to study the formation process of the coincident modes and also the associated phase-locked states. Fig. 3.4 illustrates the evolutionary spectrum for (a) the array modes, (b) the longitudinal modes

and (c) the relative phase difference $\Delta\phi$ between two incident (backward) waves at z= 0 before the 50:50 coupler, where $\Delta\phi$ is defined as $(\phi_1\text{-}\phi_2)$ modulo 2π. The initial noise in the frequency domain is modeled as uniformly distributed complex numbers with both signs of the real and imaginary parts of the field assigned stochastically to be positive or negative. The serial snapshots show that the array output grows out of noisy spontaneous emission and is continually filtered due to the interferometric nature of the composite cavity (Fig.3.4(a)). After a few milliseconds the initial random spectrum is transformed into a set of discrete mode clusters spaced by $\Delta\nu = \frac{c}{2n_1\Delta L} = 0.333$ GHz. (We show in the section 3.7: Appendix that for larger arrays the spacing between the mode clusters is given by $\Delta\nu = \frac{c_0}{2n_1\Delta L_{gcd}}$, where gcd stands for Greatest Common Divisor.) As time increases, the width of these clusters shrinks considerably owing to gain competition. Zooming in the spectrum further (Fig. 3.4(b)) shows that each mode cluster consists of the Fabry-Perot resonances of a single cavity with a free spectral range of 4.1 MHz, i.e. $c/(2n_1L)$. The result is particularly appealing since the fundamental characteristic of the laser cavity manifests itself naturally out of the model as anticipated. The phase difference between the two lasers also evolves from an initial random distribution to a linear function of frequency centered at the peak of the mode cluster. This indicates that those modes are phase locked. Note these oblique lines center around 1.5π on the vertical axes of Fig. 3.4(c) because this particular phase difference yields constructive interferences in the upper output port of the directional coupler and destructive ones in the other. Finally, cross-referencing the time orders in Fig. 3.2(c) and Fig. 3.4 reveals that both mode formation and the phase-locking behavior are established very early before the

transient oscillation begins. The transient relaxation oscillations are thus a collective phenomenon of the coupled lasers.

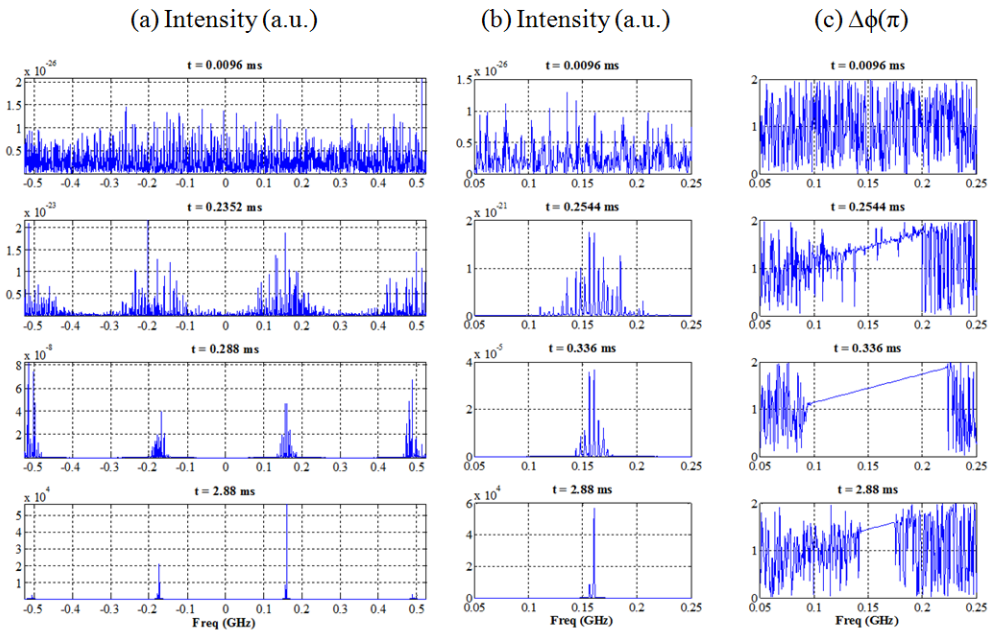

Figure 3.4 Evolution diagram of the output power spectrum for (a) the array modes, (b) the zoom-in longitudinal modes and (c) the relative phase difference $\Delta\phi(\pi)$ between two incident (backward) waves at $z = 0$. All of them start from random and noisy spontaneous emissions. The free spectral range in (b) is 4.1MHz.

3.4 Nonlinearity

The role of an intensity-dependent nonlinear phase shift in beam combining or in the phase locking process remains controversial. Some groups have claimed finding support for the enforcement of self locking through a non-resonant nonlinear index n_2 [54-56], while at the same time opposing evidence is demonstrated experimentally with high power, > 50W, fiber laser arrays [56,57]. This confusing state of affairs needs to be clarified and so we utilize the bidirectional model to study the role of nonlinear phases in coherent combining.

At low operating powers, our previous simulations have shown that the small electronic nonlinear coefficient n_2 has no apparent effect on the combining efficiency in a two-channel fiber laser array [9]. Here we increase the nonlinear coefficient γ by more than two orders of magnitude and thereby force the effects of nonlinearity to be manifested at much lower power levels. Assuming γ to be 0.9 $W^{-1}m^{-1}$, the previous simulation is repeated without changing other parameters. The two array outputs are plotted in Fig. 3.5(a) and (b) respectively for both temporal (left) and spectral (right) domains. Compared to Fig. 3.3, several apparent differences can be observed. Firstly, the FWHMs of each spectral packet broaden considerably. Second, in contrast to the centered power spectrum of the linear arrays, the nonlinearity causes the frequency components to spread and so the outermost packets are most intense. The resultant spectrum is not constrained to the parabolic loss profile and looks similar to that of pulse propagation in the presence of self-phase modulation. Third, the combining efficiency reduces to 85.5% with a significant amount of power leaking from the lossy port. The final comparison is made to the phase spectrum of the circled spectral packet in Fig. 3.5(a) and its linear counterpart of Fig. 3.3(a). The relative phase difference plots show that the range of $\Delta\phi$ expands from $\pm 0.1\pi$ in Fig. 3.5(d) to $\pm 0.5\pi$ in (c) as the nonlinear coefficient is turned on.

To completely account for the decrease of the combining efficiency owing to nonlinearity, we calculate the output powers using Eq. (3.4) assuming equal amplitudes of the incident waves before the coupler. Their power ratio is expressed as a function of their phase difference $\Delta\phi$ by [47]

$$\frac{P_1}{P_2} = \frac{1 - \sin(\Delta\phi)}{1 + \sin(\Delta\phi)} \tag{3.9}$$

A logarithmic plot of Eq. (3.9) is shown in Fig. 3.6 to illustrate how rapidly the powers transfer between one port to the other when $\Delta\phi$ changes. It is clear that the singularities occur at 1.5π and 0.5π representing the two extremes of power combining. Observe when $\Delta\phi$ is confined within 1.4π and 1.6π (in the case of the linear arrays), the power ratio is high and most of the power resides in P_1. On the other hand, when $\Delta\phi$ deviates far from 1.5π and approaches π or 2π, P_1 decreases and more power emerges out of the lower, angle-cleaved port as is evident in Fig. 3.5. The drop in combining efficiency is thus seen to be a result of the increasing bandwidth of the power spectrum, in particular, the broadening of each spectral packet under modulation.

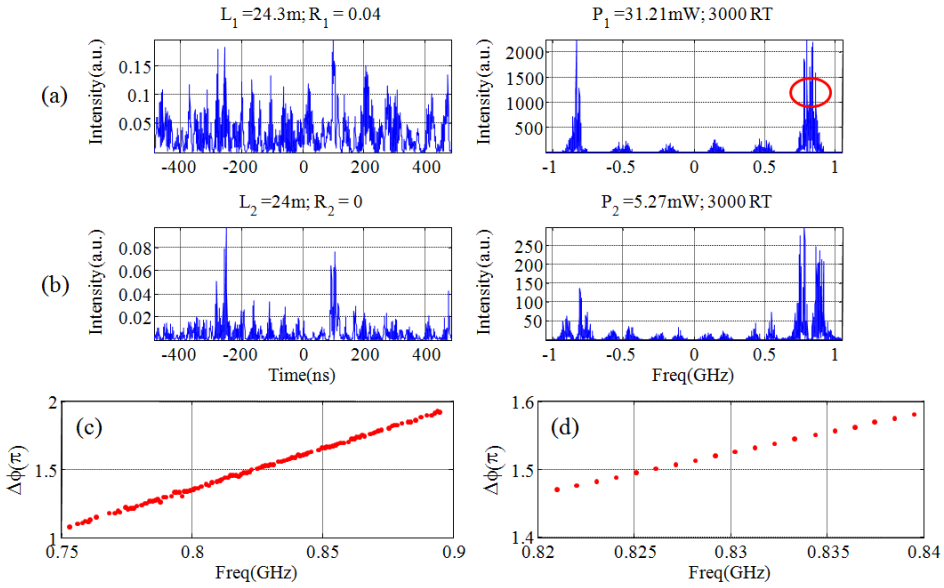

Figure 3.5 A two-channel fiber laser array is simulated with $\gamma = 0.9\ W^{-1}m^{-1}$. The array outputs are plotted in (a) and (b) respectively for both temporal (left) and spectral (right) domains. The relative phase difference of the circled spectral packets (in (a)) is plotted in (c) for nonlinear and in (d) for linear fiber laser arrays.

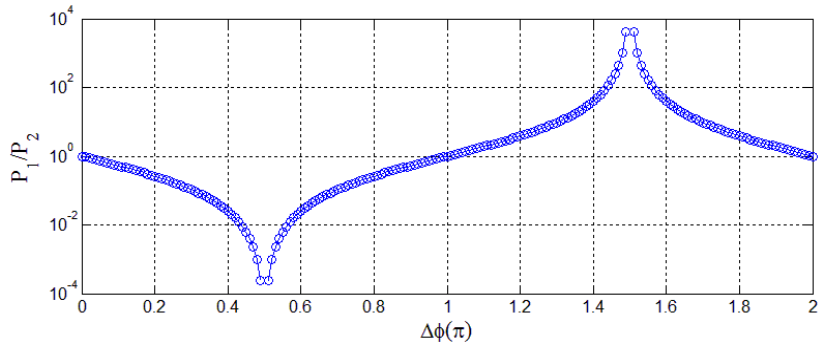

Figure 3.6 The logarithmic plot of the output power ratio in terms of relative phase $\Delta\phi$.

3.5 Array Lasing Frequencies - The Minimum Loss

As mentioned in Ref. [9], the nonzero loss dispersion coefficient *b* may give rise to reduced combining efficiency as well as shifted lasing frequencies in a two-channel fiber laser array. It is essential to understand how the resonant frequencies are determined and why the frequency shift occurs in the presence of additional loss sources. A reasonable expectation is that the array chooses to lase at the frequency that experiences the least overall losses. In order to verify this point, we present a simple loss analysis based on the unidirectional two-channel fiber laser array. The ring cavity configuration is adopted here as seen in Fig. 3.7 since it is simpler and we have shown earlier that the coherent beam combining is not affected by the backward propagating waves of standing-wave cavities.

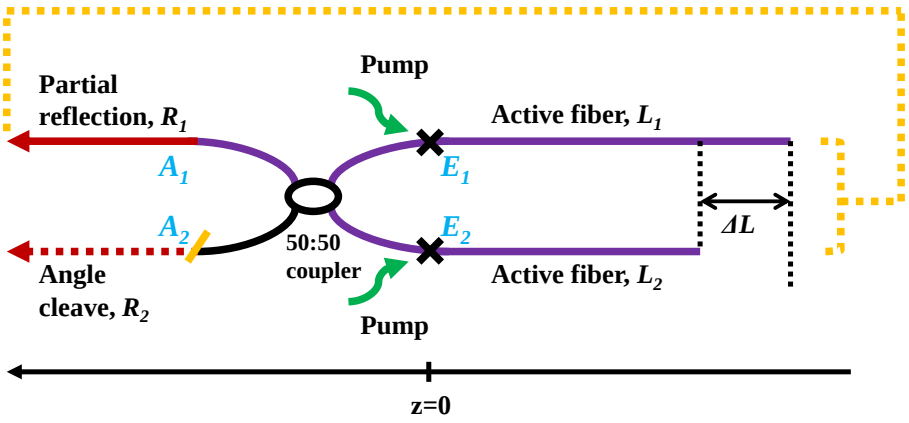

Figure 3.7 A unidirectional two-channel fiber laser array.

To derive the frequency-dependent array loss, the circulating power within each fiber laser before the coupler is assumed to be P. The coupler output powers are calculated, according to Eq. (3.9), as $P(1+sin(\Delta\phi))$ and $P(1-sin(\Delta\phi))$ depending on the accumulated phase difference of $\Delta\phi = \omega/cn_1(L_1 - L_2)$ between the two incident fields. Only one of the output powers is reflected and fed back into the other end of the two fibers. Take $P(1+sin(\Delta\phi))$ for example; the steady-state laser oscillation requires that the power be restored to P at the reference plane just before the coupler, so we can write

$$P(1+sin(\Delta\phi)) \times R \times \frac{1}{2} exp([g - \alpha - b\omega^2)L] = P \tag{3.10}$$

where R is the power reflectivity, g is the saturated gain, α is the linear loss and b is the loss dispersion coefficient. We take the logarithm of Eq. (3.10) and the expression for the loss is given as the right hand side of Eq. (3.11).

$$g = \alpha + b\omega^2 - \frac{\log\left[\frac{R(1+\sin(\Delta\phi))}{2}\right]}{L} \tag{3.11}$$

The frequency dependent loss profile can thus be readily plotted by plugging in $\Delta\phi = \omega/cn_1(L_1 - L_2)$.

Consider an example of a two-channel fiber laser array of lengths 24.0005 m and 24.0 m, with the simulated power spectra shown in Fig. 3.8 for (a) b = 0 ps^2m^{-1} and (b) b = 0.13 ps^2m^{-1} respectively. (The very small length difference is chosen to ensure the spike separation and the frequency shifts are large enough for clear visualization.) It is clear the combining efficiency drops considerably and the lasing frequency shifts from 126.5 GHz to 45.79 GHz in the presence of nonzero loss dispersion. Utilizing Eq. (3.11), we plot the frequency-dependent loss on a logarithmic scale with blue solid lines and further overlap them with the output lasing frequencies (red solid lines) in Fig. 3.9 for better

visualization. The loss curves exhibit minimum values near -300 GHz and 100 GHz in Fig. 9(a) and around 50 GHz in Fig. 9(b). In both cases, the good agreement between array resonant modes and the location of the minimum losses validates the hypothesis that the coupled array finds the mode with minimum overall losses.

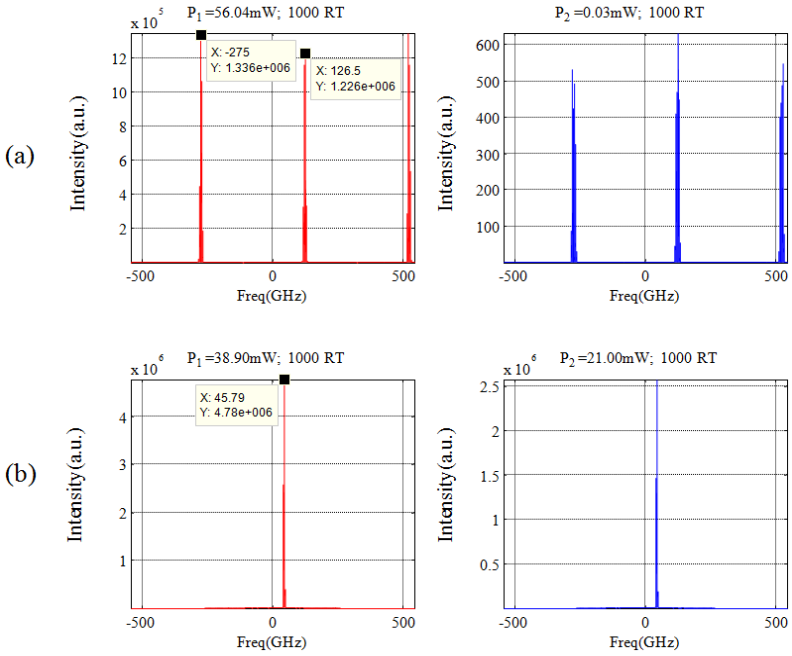

Figure 3.8 Power spectra of a two channel fiber laser array with fiber lengths 24.0005m and 24.0m for (a) $b = 0$ ps^{2}m^{-1} and (b) $b = 0.13$ ps^{2}m^{-1}.

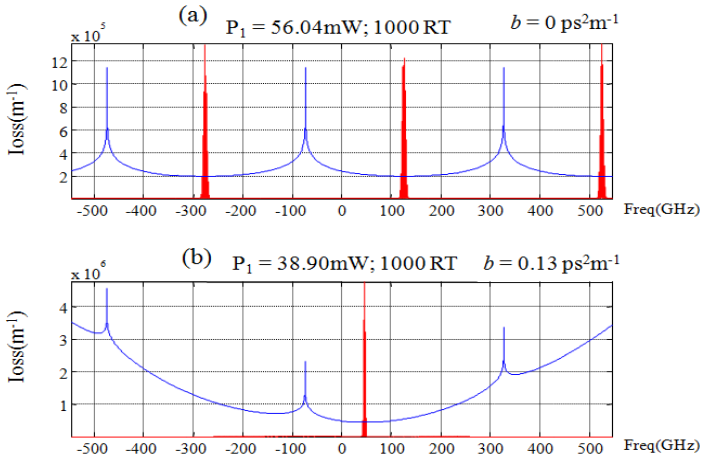

Figure 3.9 The frequency dependent losses (m^{-1}), plotted in the log scale with blue lines, are overlapped with the lasing spectrum of the output fields (red spikes) for (a) zero and (b) nonzero b coefficients respectively.

3.6 Conclusion

To conclude, we have extended our dynamic model of passive beam combining in fiber lasers to include transient gain dynamics and the interaction of counterpropagating waves. The model allows us to study the process in which composite cavity modes are selected and the establishment of a fixed phase relationship between the coupled amplifiers. We find that the phase locked state is established relatively soon within several hundred roundtrips and that the amplifiers exhibit collective transient relaxation oscillations upon turn-on. The unsettled issue of nonlinearity is also studied. Our simulation suggests the nonresonant n_2 induces spectral broadening and reduces the combining efficiency at high power levels. We explore the working principle of the array and demonstrate that it is based on the selection of composite cavity modes with the minimum overall losses.

3.7 Appendix: Array Mode Spacing - The Greatest Common Divisor

It is well known that when two lasers of length L_1 and L_2 are combined in a composite cavity, the individual Fabry-Perot frequency combs become modulated with an envelope whose peaks are separated by $\Delta\upsilon = c/(2n_1\Delta L)$, where $\Delta L = L_2 - L_1$. For N coupled lasers the separation between the maxima of the modulation envelope can be found by examining the condition for constructive interference at all the 50:50 couplers. Since lasing of the composite cavity should occur near these maxima (corresponding to frequencies of minimum loss) this analysis helps to make sense of the complicated spectra observed in multi-element arrays.

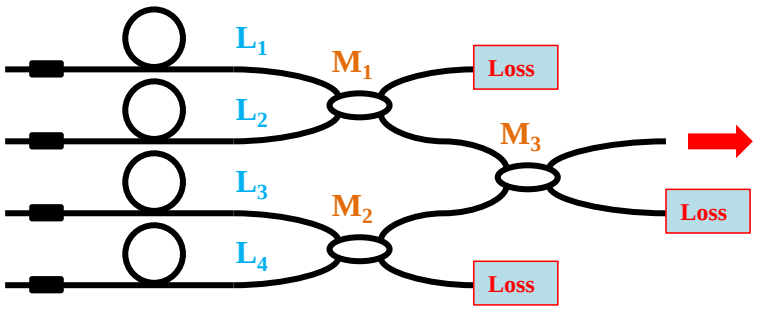

Figure 3.10 A four-channel fiber laser array. The figure is taken and modified from Ref. [58].

Consider a four-channel fiber laser array in Fig. 3.10, where the coherent combining is governed by the 50:50 directional couplers and the linear coupling matrix of Eq. (3.4). For any frequency f constructive interferences can occur at the lower output port of the couplers M_1 and the upper output ports of M_2 and M_3 respectively when

$$\begin{aligned} \frac{2\pi n_1 f}{c_0} 2(L_2 - L_1) &= \frac{3\pi}{2} + m_1 2\pi \\ \frac{2\pi n_1 f}{c_0} 2(L_3 - L_4) &= \frac{3\pi}{2} + m_2 2\pi \\ \frac{2\pi n_1 f}{c_0} 2(L_3 - L_2) &= \frac{3\pi}{2} + m_3 2\pi \end{aligned} \tag{3.12}$$

Here n_1 is refractive index of the fiber and m_1, m_2, m_3 are integers. Note the third equation of Eq. (3.12) describes the power addition criterion in M_3 and it depends only on the fiber lengths L_2 and L_3. This can be understood by calculating the phase of the output fields from the coupler M_1 by

$$\frac{1}{\sqrt{2}}\begin{bmatrix} 1 & -j \\ -j & 1 \end{bmatrix}\begin{bmatrix} e^{j2kL_1} \\ e^{j2kL_2} \end{bmatrix} = \frac{1}{\sqrt{2}}\begin{bmatrix} e^{j2kL_1} - je^{j2kL_2} \\ -je^{j2kL_1} + e^{j2kL_2} \end{bmatrix} \tag{3.13}$$

Assuming the input waves interfere destructively at the upper output port of M_1 such that $e^{j2kL_1} - je^{j2kL_2} = 0$, the emerging field of the lower port $-je^{j2kL_1} + e^{j2kL_2}$ can then be written as $2e^{j2kL_2}$ if we replace $2e^{j2kL_1}$ by je^{j2kL_2}. Similar calculation can be applied to

M_2 with the result of $2e^{j2kL_3}$ and so the phases of the two input fields into M_3 are merely characterized by fiber lengths L_2 and L_3 in Eq. (3.13).

Given random combinations of lengths L_1 to L_4, the exact solution f generally does not exist for all three equations in Eq. (3.12) even with the degrees of freedom provided by m_1, m_2, and m_3. In most cases only an optimal frequency $\bar{f}$ can be obtained. Let us assume $\bar{f}$ satisfies the following conditions:

$$\begin{aligned}
\frac{2\pi n_1 \bar{f}}{c_0} 2(L_2 - L_1) &= \frac{3\pi}{2} + m_1 2\pi + \Delta\phi_1 \\
\frac{2\pi n_1 \bar{f}}{c_0} 2(L_3 - L_4) &= \frac{3\pi}{2} + m_2 2\pi + \Delta\phi_2 \\
\frac{2\pi n_1 \bar{f}}{c_0} 2(L_3 - L_2) &= \frac{3\pi}{2} + m_3 2\pi + \Delta\phi_3
\end{aligned} \tag{3.14}$$

where $\Delta\phi_k$, k = 1⋯3, indicates the deviations of $\bar{f}$ away from the exact solution of each equation in Eq. (3.12) and is responsible for the imperfect power combining due to the residual phase mismatch. The optimal solution $\bar{f}$ is recognized as the frequency of minimum coupling loss in the four-channel array simulation as shown in Ref. [9]. We can then calculate the period of these modes $\Delta\upsilon$ by substituting $\bar{f} + \Delta\upsilon$ into $\bar{f}$ in Eq. (3.14);

$$\begin{aligned}
\frac{2\pi n_1 (\bar{f} + \Delta\upsilon)}{c_0} 2(L_2 - L_1) &= \frac{3\pi}{2} + (m_1 + p_1) 2\pi + \Delta\phi_1 \\
\frac{2\pi n_1 (\bar{f} + \Delta\upsilon)}{c_0} 2(L_3 - L_4) &= \frac{3\pi}{2} + (m_2 + p_2) 2\pi + \Delta\phi_2 \\
\frac{2\pi n_1 (\bar{f} + \Delta\upsilon)}{c_0} 2(L_2 - L_3) &= \frac{3\pi}{2} + (m_3 + p_3) 2\pi + \Delta\phi_3
\end{aligned} \tag{3.15}$$

where p_k, k = 1⋯3 are new integers. Upon eliminating $\bar{f}$ from the above two sets of equations we find

$$\frac{2\pi n_1 \Delta v}{c_0} 2(L_2 - L_1) = p_1 2\pi$$

$$\frac{2\pi n_1 \Delta v}{c_0} 2(L_3 - L_4) = p_2 2\pi \tag{3.16}$$

$$\frac{2\pi n_1 \Delta v}{c_0} 2(L_2 - L_3) = p_3 2\pi$$

The maxima of the modulation envelope are thus spaced by a frequency given by

$$\Delta v = \frac{c_0}{2n_1 \Delta L_c} = \text{LCM}\left[\frac{c_0}{2n_1(L_1 - L_2)}, \frac{c_0}{2n_1(L_2 - L_3)}, \frac{c_0}{2n_1(L_3 - L_4)}\right] \tag{3.17}$$

where LCM represents the least common multiple of the arguments and ΔL_c represents some equivalent path length difference. For this solution p_1, p_2, p_3 are integers with no common factor. From this result it can also be shown that Δv is determined by the greatest common divisor of the length differences. Thus the frequencies of minimum loss are spaced by

$$\Delta v = \frac{c_0}{2n_1 \Delta L_{gcd}} \tag{3.18}$$

where $\Delta L_{gcd} = \text{GCD}[L_1 - L_2, L_2 - L_3, L_3 - L_4] = \Delta L_c$. This result can be generalized to any number of lasers in the tree architecture described here.

It is important to note that the composite cavity modes have to satisfy the condition that the field at any point reproduces itself after a round trip, within a phase shift of an integral multiple of 2π. These modes form a very dense comb structure which is modulated by an envelope representing the transfer function of the multiple-coupler interferometer. Maximum combining efficiency occurs where these modes coincide with maxima of the transfer function.

To support the analysis, a numerical example is given for a unidirectional four-channel fiber laser array of lengths 24.0, 24.3, 23.733 and 24.633 m. The greatest common divisor

of their length differences is 3 mm and the mode periodicity is calculated to be 66.7 GHz according to $c_0/(n_1 \Delta L_{gcd})$ where the factor of two differences from Eq. (3.18) is due to the single pass nature of the laser cavity in this case. The simulation result is shown in Fig. 3.11 with Δv seen to be 66.7 GHz and is consistent with the theoretical prediction.

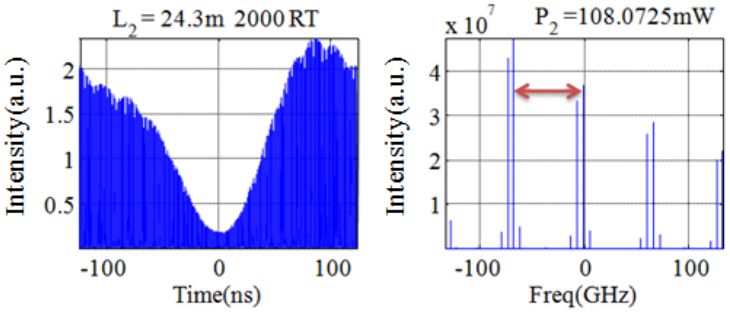

Figure 3.11 Coherent combining of a four-channel fiber laser array with lengths 24.0, 24.3, 23.733 and 24.633 m. The period of the power spectrum pattern indicated by the red arrow is measured to be 66.7 GHz.

CHAPTER 4

Array Size Scalability of Passively Coherently Phased Fiber Laser Arrays

4.1 Introduction

There has been much interest in passive coherent phasing of fiber laser arrays as a possible path for multi-kW power scaling. In principle, passive beam combining of an *N*-channel fiber laser array can be regarded as an interferometric system of *N* coupled amplifiers in a composite cavity. The multiple longitudinal modes of individual fiber lasers of varying lengths are superposed to form coherently-combined modes (or supermodes) of the composite cavity whenever there is a coincidence in the individual frequency combs. As the number of elements in the array increases, the probability of finding such an accidental coincidence in the resonances of the array system is decreased, and thus the combined-power efficiency drops.

Several methods have been proposed for passive coherent phasing, including distributed evanescent coupling [59], discrete directional coupling [60,61], and the use of self-Fourier cavities [62]. However, the most important question associated with this beam combining approach is how the coherent-combing efficiency scales with the array size. The initial experimental explorations using a fixed 8-channel array by Shirakawa et al [60] indicate that combining efficiency is expected to decrease with the increase of the array size. This appears to be supported by theoretical estimates as well [63-66].

However, due to the limited experimental data and the approximate character of the first theoretical estimates [64-66], this passively-phased array size scaling is still not sufficiently understood.

In this paper we present a systematic experimental and simulational study of 2- to 16-channel fiber-laser array coherent phasing. We find good agreement between the experimental combining efficiencies and the results of simulations using a new propagation model. We also explore for the first time the important question of the dependence of power fluctuations on array size. Finally, the beat spectra are studied to provide supportive evidence for the diminishing probability of finding supermodes in a larger array size.

4.2 Experimental Configuration

As a model system for exploring fiber-laser array passive-coherent phasing we choose an all-single-mode-fiber configuration, where the combining is accomplished using 50:50 single-mode fiber couplers [60]. This enables a simple and easily scalable experimental implementation, with unambiguous beam-combining interpretation. The experimental setup is shown in Fig. 4.1 as an example for 16-channel combining. Each single-mode fiber laser channel consists of a 980/1064-nm WDM, connected to a 3.5-m long Yb-doped single-mode fiber with a 1064-nm faraday mirror at one end of the cavity. These laser channels are combined into various-sized arrays using 50:50 single-mode couplers. The basic building block is a 2-laser array, thus all array sizes between 2 and 16 are explored as multiples of 2 (2, 4, 6, 8, 10, 12, 14, and 16). The individual configurations are arranged as in Fig. 4.2 with the total lengths of the 2, 4, 8, 16-channel lasers being 8.5m, 10.5m, 12.5m, and 14.5m, respectively. The output-end of the cavity of this array

is formed by a single straight-cleaved fiber-end, providing ~4% back reflection. All the other remaining output leads of 50:50 fiber couplers are angle-cleaved to prevent feedback from these ends. During experiments an optimized coherent combination has been attained by balancing pumping power for each 2-channel building block such that power equality of two inputs of each fused coupler is achieved. Due to the broad-band nature of Faraday mirrors, each laser channel was operating at ~8nm spectral bandwidth.

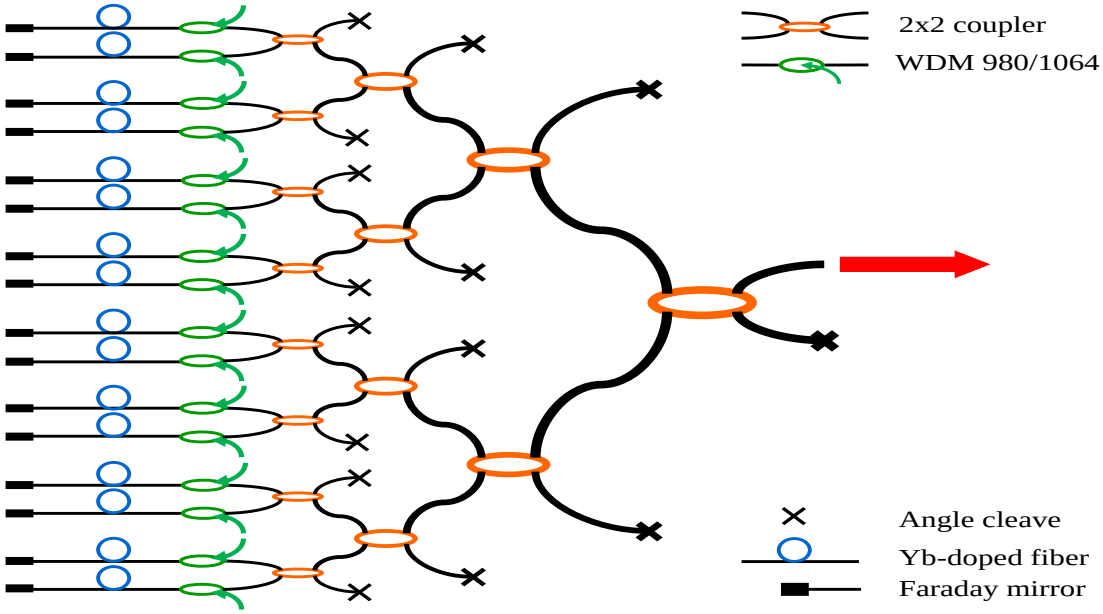

Figure 4.1 Experimental setup as an example of 16-channel combining.

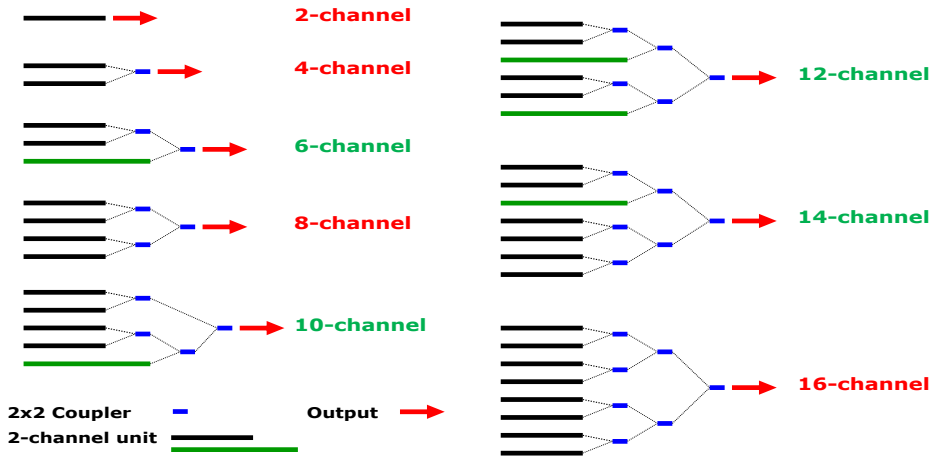

Figure 4.2 Configurations of 2- to 16-channel combining with a 2-laser array interval.

4.3 Power Combining Efficiency

Taking P_{out} as the output of the straight-cleaved end and P_i as the power from the i^{th} single laser if uncoupled, we define the power combining efficiency for an *N*-channel array as

$$N\text{-channel combined-power efficiency} = \frac{P_{out}}{\sum_i^N P_i} \tag{4.1}$$

The power is measured with a power meter with a response time of milliseconds. Because of power fluctuations on that time-scale we record the statistical mean over 5 minutes. The measured power combining efficiencies (blue solid dots) and their fluctuations (error bars) for 2, 4, 6, 8, 10, 12, 14, and 16-channel combining are shown in Fig. 4.3 and listed in Table 4-1. The measured fluctuation shown in the parenthesis of Table 4-1 is defined in Eq. (4.2).

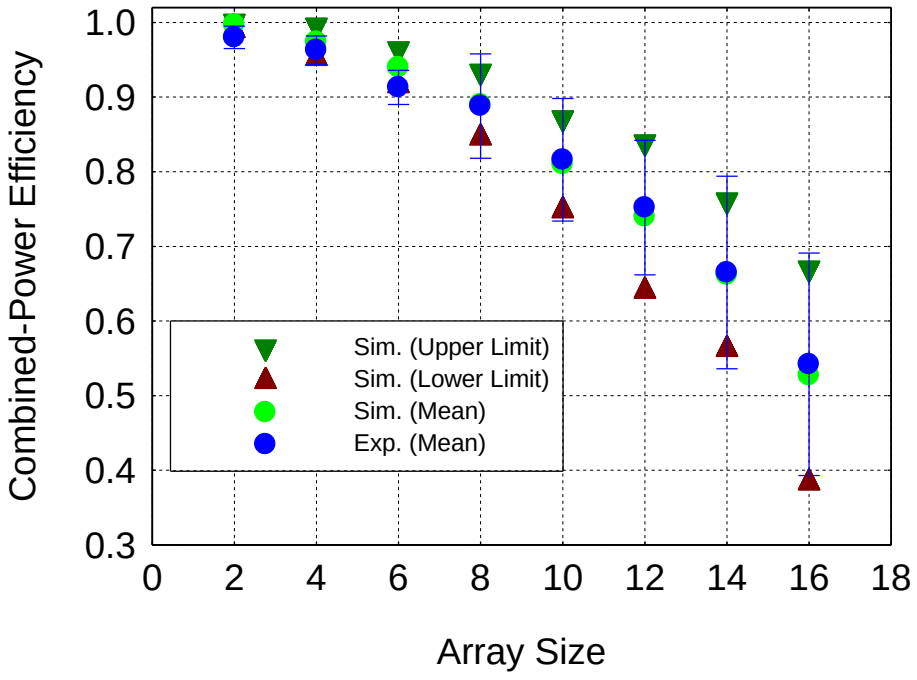

Figure 4.3 Combined-power efficiency and power fluctuation (error bars for experimental results) versus fiber array size.

Table 4-1 Combining efficiency and power fluctuations

Number of Channels	Measured Combining Efficiency (Fluctuation)	Calculated Efficiency
2	0.98 (±1.5%)	0.997
4	0.96 (±2%)	0.974
6	0.91 (± 2.5%)	0.94
8	0.89 (±4%)	0.89
10	0.82 (±8%)	0.81
12	0.75 (±12%)	0.74
14	0.67 (±16.75%)	0.662
16	0.54 (±27.5%)	0.527

The calculated power combining efficiencies (green solid dots) are obtained from a recently published model that accounts for the multiple longitudinal modes of individual fiber lasers, the formation of the composite-cavity modes, and the natural selection of the resonant arrays modes that have minimum loss [9]. Since it is based on the amplifying nonlinear Schrödinger equation, effects such as gain saturation, fiber nonlinearity, group velocity dispersion, and loss dispersion of bandwidth limiting elements in the cavity can be readily taken into account (see Section 4.7:Appendix). This new model also exhibits self-adjustment process of beam combining suitable for describing the dynamic features such as power fluctuation and beat spectra.

In fitting the theoretical calculations to the experiment, we had to account for the fact that the individual fiber lengths are not precisely known, as a result of occasional fiber breakage during assembly and splicing and connector uncertainties. We estimate an uncertainty of about 2% in the nominal lengths of the individual fiber amplifier channels. In the simulation, for a given number N of amplifying channels, a set of lengths N were randomly generated that varied within 2% of the nominal length. The simulated

combining efficiency is the best fit of several realizations of length distributions, averaged over the fluctuations described in Section 4.4. From Fig. 4.3, the simulated and experimental results agree very well and both of them indicate a clear evolution of combined-power efficiency with array size: power combining efficiency decreases monotonically with array size.

Prior to this work there have been only three published experimental data points regarding the scalability of this particular scheme of passive beam combining [60]. Two of those points are for 2-and 4-element arrays with a spectral bandwidth of 0.6 nm imposed by fiber Bragg gratings. The third point is for an 8-element array with a broadband mirror and a sprectral bandwidth of 10 nm. In our experiments we hold the bandwidth constant and vary the array size in order to obtain a consistent picture of how combining efficiency scales with number of amplifiers. In Fig. 4.4 we plot the experimental results of Shirakawa et al [60] (red squares), our new measurements (blue dots), and the theoretical estimate proposed by Kouznetsov et al [65] (red line). The simple theoretical estimate appears to predict a faster drop off in combining efficiency with array size than what we observe in our experiments.

The drop of combining efficiency means that the power of individual fiber lasers is not always coherently combined at the straight-cleaved end with a null at the angle-cleaved end. The decrease in combining efficiency reflects the difficulty in finding congruencies among the frequency combs of the individual resonators that make up the overall interferometric cavity laser. From Fig. 4.3 it can be seen that the practically useful maximum number of laser channels that can be coherently combined in this manner is approximately 10-12.

For a given array size, the combining efficiency can be improved by increasing the spectral bandwidth [60]. In our system the bandwidth of 8 nm imposed by the Faraday mirrors is close to the maximum 10 nm of the broadband mirrors used by Shirakawa, et al. [60] The use of Faraday mirrors aids in polarization control.

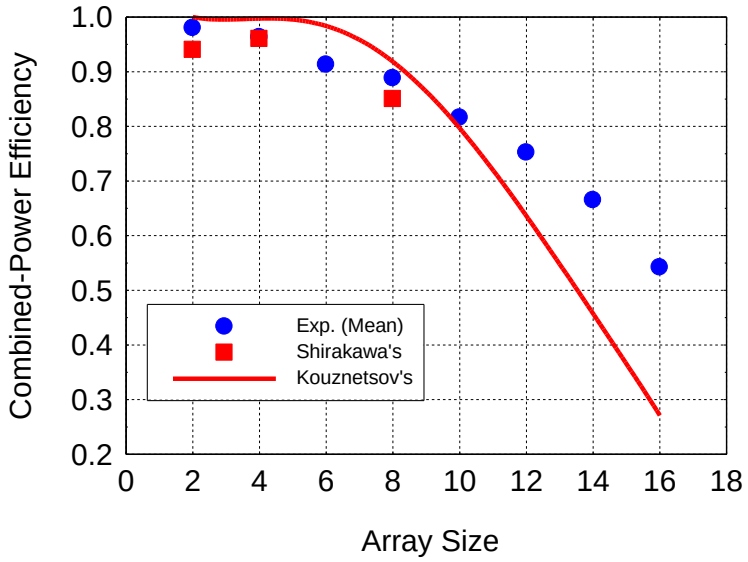

Figure 4.4 Combined-power efficiency versus fiber array size between previous (Shirakawa [60], Kouznetsov [65]) and present works.

4.4 Power Fluctuation

The output of the coherently combined fiber laser array exhibits significant power fluctuations on a time scale of milliseconds. These fluctuations are due to environmental factors such as temperature and pressure changes, the interferometric nature of the fiber array resulting in an efficient sensor for these changes. In Fig. 4.3, the measured power fluctuation, indicated by the experimental error bars, is seen to increase with array size. Here,

$$\text{Relative Power fluctuation (\%)} = \frac{3\sigma}{P_{out}}, \tag{4.2}$$

where σ denotes the statistical standard deviation. The extent of $\pm 3\sigma$ includes approximately the maximum range of power fluctuation.

To simulate the power fluctuations we assume that environmental factors lead to length changes on the order of a wavelength for each channel, or, equivalently, a phase shift of 2π. We let the length of each fiber increase by 0.8 nm per round trip so that after about 1250 roundtrips a length change of about one wavelength has accumulated. The power value per round trip is recorded until several thousand round trips later the overall accumulation of phase shift has reached 2π (~1 μm), then all recorded power values are statistically analyzed to attain the aforementioned definition of power fluctuation range ($\pm 3\sigma$). From Fig. 4.3, the statistical simulation results, using the upper (downward triangles) and lower (upward triangles) limits to represent the maximum and minimum of calculated power combining efficiency, indicate that the fluctuation ranges increase with the increasing array size and they agree well with similar power fluctuation values in experiments. The results indicate that small fluctuations in fiber length can result in substantial power instabilities and fluctuations, especially for arrays with a large number of elements.

To further explore how the rate of fluctuation relates to array size, we plot in Fig. 4.5 the experimental (blue dots) and simulational (red squares) fluctuations versus number of channels in the array, N. We find that the power fluctuations scale with array size as N^3 (green fitting line). This scaling behavior of power fluctuations in coherent beam combining has never been reported. We do not yet have a simple explanation for this cubic dependence on array size but we note that N^3 seems to describe the product of a coherent process (scaling as N^2) and an incoherent process (scaling as N). This rapid

growth of fluctuations with arrays size is one of the factors that may limit the scalability of beam combining by passive coherent phasing. It is important to note, however, that these results are for a particular geometry of passive beam combining involving laser amplifiers in a composite cavity. The behavior of coupled laser oscillators may well be different.

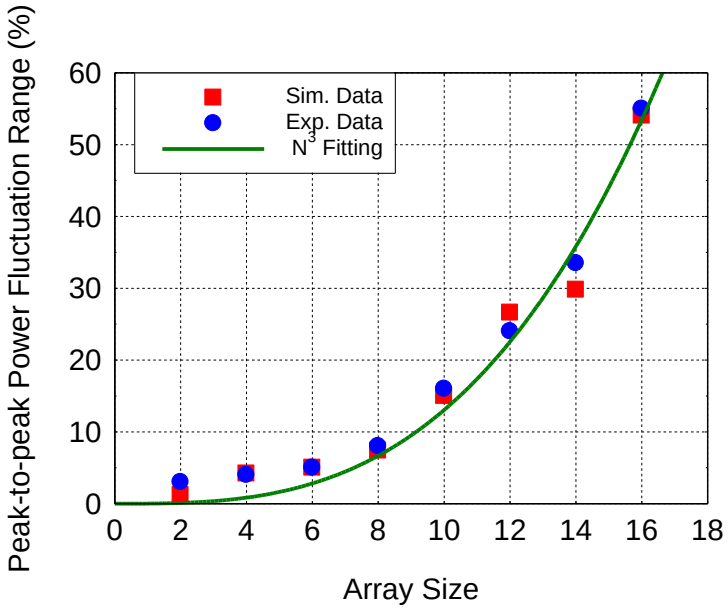

Figure 4.5 Peak-to-peak power fluctuation ranges versus array size from experiments, simulation, and N^3 fitting.

4.5 Beat Spectra

The decline of power combining efficiency with array size believed to be a consequence of the increasing scarcity of coherently combined modes within the laser gain bandwidth. We investigate this scarcity by measuring and calculating beat spectra in fiber-laser arrays. To make it easier to observe beat spectra within the limited spectral bandwidth of an RF spectrometer, an additional 37.5-m single-mode fiber is inserted at the output-end and a 2-m single-mode fiber added to one arm of the fiber-laser array. The greater optical in-fiber length leads to a smaller mode separation of longitudinal modes, and thus more

longitudinal modes are expected to exist and beat with each other in this composite cavity. The schematic is shown in Fig. 4.6 as an example of 4-channel combining. During measurements, a fast photodetector and a 1-GHz RF Spectrum Analyzer are used to detect beat spectra.

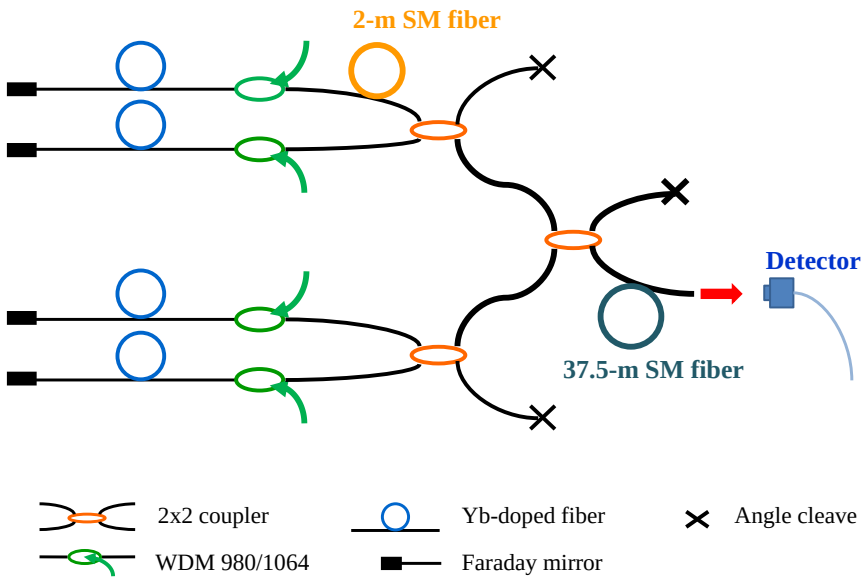

Figure 4.6 Experimental setup for beat spectrum measurements as an example of 4-channel combining.

According to 2-channel laser array theory, the free spectral range (FSR) of adjacent beat packets and mode separation (MS) of adjacent longitudinal modes are defined as:

$$\mathrm{FSR} = \frac{c}{2n\Delta L} \tag{4.3}$$

$$\mathrm{MS} = \frac{c}{2nL} \tag{4.4}$$

where ΔL and L are the length difference and average length of laser array, respectively. In 2-channel beat spectra, the roughly 56 MHz FSR in Fig. 4.7(a) and 2MHz MS in Fig. 4.7(b), based on Eqs. (4.3-4.4), correspond very well to the actual ~1.78-m in-fiber length difference and 46-m average length. In 4-channel spectra, ~2MHz MS in Fig. 7(d) is still observed but FSR is greatly increased up to 475-MHz in Fig. 7(c). The suppression of

multiple beat packets in 2-channel to only one extra packet in 4-channel and zero extra packet in 8-channel or beyond within 1-GHz window directly indicates the number of the coherently-combined modes (supermodes) in the cavity is greatly reduced as array size multiplies, resulting in the drop of combined-power efficiency. In simulation, by selecting 2-channel in-fiber lengths as 47.82m and 46m; and 4-channel as 47.89m, 46m, 46.42m, and 46.21m, the calculated 2-channel beat spectrum in Fig. 4.8(a) exhibits multiple peaks whereas the 4-channel in Fig. 4.8(b) has only one extra peak. These length parameters used for simulation here are quite arbitrarily assigned since the suppression of supermodes from 2-channel to larger channels always holds. Therefore, the simulation result supports the experimental conclusion that the increase in the number of elements in the array leads to a greater suppression of supermodes, resulting in the decrease of power combining efficiency with larger array number.

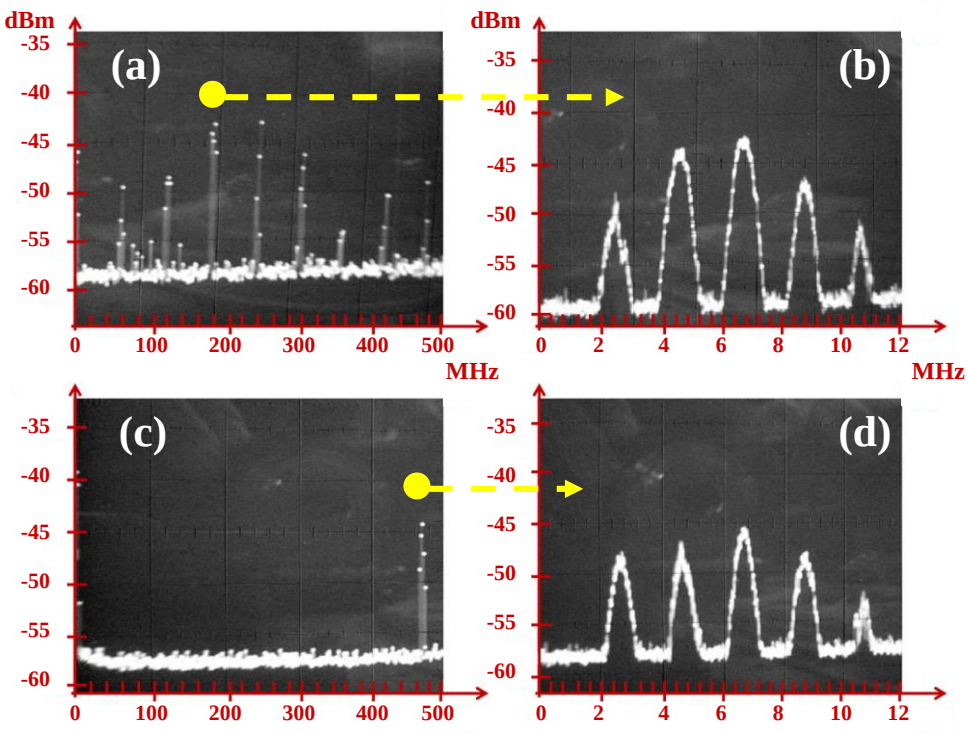

Figure 4.7 Beat spectra of 2-channel (a) and the zoom-in of designated packet (b); and those of 4-channel (c) and the zoom-in of designated packet (d).

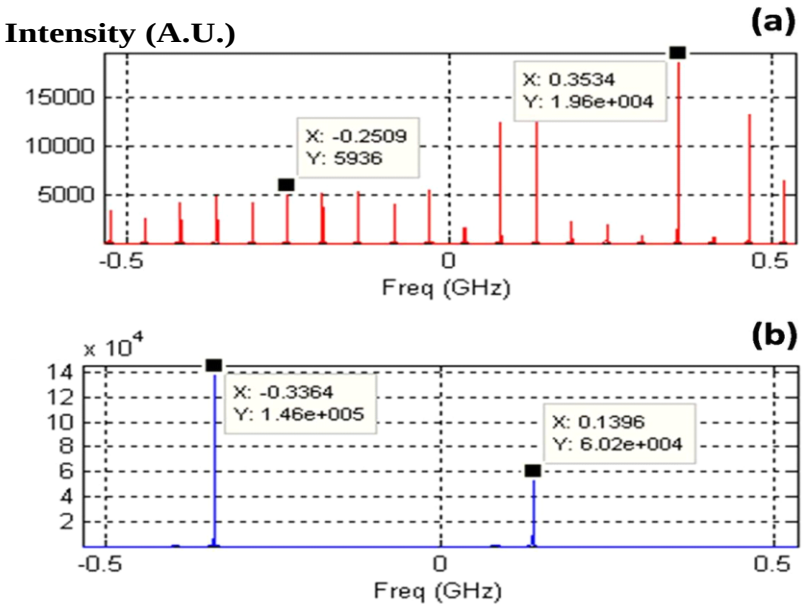

Figure 4.8 Simulation of beat spectra for 2-channel (a) with 47.82 and 46-m in-fiber lengths; and that of 4-channel (b) with 47.89, 46, 46.42, and 46.21-m in-fiber lengths.

4.6 Discussion and Conclusion

The most important question associated with passive coherent phasing of fiber-laser arrays is how the coherent-combing efficiency scales with array size. In this paper, we have studied the detailed evolution of combined-power efficiency and the issue of power fluctuation versus array size from 2 to 16-channel passively coherently combined fiber-laser arrays.

For power combining efficiency, good agreement between our simulation model and experiments is demonstrated for arrays containing up to 16 channels. Small phase shifts resulting from wavelength-scale length variations are verified numerically to be an important factor resulting in fluctuations and instability in output power. The power fluctuations scale with array size as N^3. Investigation of array beat spectra supports the notion that the decrease of power combining efficiency with array size is a result of increasing scarcity of composite-cavity supermodes.

The work here has focused on a particular combining scheme involving separate amplifiers, 50:50 couplers, and uncontrolled fiber lengths. Other approaches to passive beam combining [67,68] may yield different results regarding scalability. In particular, our preliminary theoretical investigations indicate that the use of phase conjugate mirrors can significantly improve the power scaling behavior of passively combined fiber laser amplifiers.

4.7 Appendix

The model used for the beam combining simulations is based on the amplified Nonlinear Schrödinger equation:

$$\frac{\partial E_j}{\partial z} = \frac{1}{2}\left(g_j - \alpha\right)E_j - \beta_1 \frac{\partial E_j}{\partial t} + \frac{1}{2}(b - i\beta_2)\frac{\partial^2 E_j}{\partial t^2} + i\gamma\left|E_j\right|^2 E_j$$

with saturated gain

$$g_j = \frac{g_{0j}}{\left(1 + \frac{\int_0^T \left|E_j\right|^2 dt}{TP_{sat}}\right)}$$

Throughout this paper, the common parameter values used for simulation are λ (working wavelength)=1.064 μm, b (loss dispersion)=0.013 ps^2/m, g_0 (unsaturated gain)=2.67 m^{-1}, γ (nonlinear coefficient)=0.003 $W^{-1}m^{-1}$, α (propagation loss)=8 dB/km, and β_2 (phase dispersion)=0.024 ps^2/m. According to our study, nonlinearity has little effect on power efficiency, power fluctuation, and beat spectra.

CHAPTER 5

Coherent Femtosecond Pulse Combining from Four Parallel Chirped Pulse Fiber Amplifiers

5.1 Introduction

Fiber lasers in general – and ultrashort-pulse fiber lasers in particular – have demonstrated a remarkable increase in average power performance over the past decade [74, 87]. This is due to the fiber geometry, in which a large surface area to volume ratio facilitates rapid heat dissipation and consequently allows for scaling performance to high average powers. But the tradeoff with the fiber geometry is that the optical signal is tightly confined to a relatively small transverse area over relatively long lengths. This sets limits on achieving high pulse energies because of saturation-fluence, optical damage and nonlinear effects such as stimulated Raman scattering (SRS), stimulated Brillouin Scattering (SBS), four-wave-mixing (FWM), or self-phase modulation (SPM). Limitations on pulse energy are particularly severe for chirped-pulse amplification (CPA) of ultrashort pulses in fibers [98], where recompressed-pulse distortions caused by SPM occur at relatively low pulse energies, in the ~mJ range [97].

A general approach to overcome single-laser energy and power limitations is to combine the outputs from an array of lasers [94]. Active coherent phasing appears to be best suited for combining large numbers of individual laser channels [95], and has been

demonstrated with cw [100], pulsed [101], and ultrashort-pulse [70,71] fiber lasers. The two key technical challenges associated with this active coherent combining are (i) how to spatially combine multiple output beams, and (ii) how to temporally combine, i.e. track and correct phasing errors in each individual channel. Multiple beams can be either tiled spatially [96], thus combining only in the far-field, or can be combined into a single beam using binary-tree type of arrangement based on either interferometric 50:50 beam splitters/combiners [86] or polarization beam splitters (PBS) [83], or can be directly converted from a coherently-phased spatially-tiled beam array into a single diffraction-limited beam using diffractive-optics [84] or multi-mode interference effects in hollow-waveguides [85].

There are different strategies that can be used for tracking phasing errors in each individual channel. Applicability of a particular phasing approach, however, does depend on a beam combining method used. For example, one strategy is based on spatial recognition of each-channel phase in a tiled array output by using a detector array and heterodyne phase detection with respect to a reference channel [86,91], which requires spatial monitoring of a tiled-array output. Hänsch-Couillaud detection scheme measuring deviation from a linear polarization can be used to track relative phases between each pair of channels [70], but this strategy is only applicable to PBS combiners in a binary-tree type arrangements and requires a matching tree of detectors. Alternatively, each channel can be "tagged" by individual-frequency modulation which allows tracking relative phases of all the channels with a single detector [4,5], a so-called LOCSET technique (locking of optical coherence by single-detector electronic-frequency tagging). This strategy appears to be the most general approach, applicable to all spatial beam

combining methods, and therefore might be the best path for phasing a large number of channels.

In this paper we report on coherent combining of four parallel femtosecond pulse fiber amplifiers using the LOCSET phasing scheme and a binary-tree type of beam combining. In addition, we explore the combining efficiency of such a system as a function of the number of parallel channels. Understanding the array-size scalability is crucial for the development of high power and high energy ultrashort-pulse fiber laser arrays. Fundamentally, scalability of a combined-array size is determined by the effect of the phase and amplitude noise on the combining efficiency. General statistical analysis indicates [88,89] that if the phase-noise average is zero, then efficiency should converge to a fixed value at very large number of channels; but if this average is different from zero then the combining efficiency continuously degrades with channel number [88]. Here we study the extrapolated performance of coherently combined system at a very large number of parallel channels phased using LOCSET, by first developing a theoretical model, and then validating its accuracy through comparison of its predictions with the experimentally characterized performance of our combining system. Finally, we use this "calibrated" model to predict the combining performance with increasing number of channels in the presence of temporal amplitude and phase variations in each of the parallel-channel signal paths. We show that at very large number of combined channels using the LOCSET phasing arrangement, combining efficiency should converge to a fixed value, determined only by the magnitude of the phase and amplitude errors.

Section 5.2 of this chapter describes the experimental system and the details of its operation. Measured performance of this coherently-combined fiber CPA array system is

presented in Section 5.3. The theoretical model and its experimental validation by comparing it to the measured characteristics of a coherently combined array is given in Section 5.4. In Section 5.5 we analyze the coherent-combining efficiency of such an array with increasing number of channels and explore its dependence on the magnitude of phase and amplitude errors. Conclusions are given in Section 5.6.

5.2 Experiment

5.2.1 Fiber Chirped Pulse Amplifier Array

To explore the coherent phasing of multiple parallel fiber CPA channels, we built an experimental coherently combined system based on an all-fiber, four-channel amplifier array. The system layout is shown in Fig. 5.1. It consists of a mode-locked femtosecond pulse fiber oscillator, a pulse stretcher, a parallel fiber amplifier array, a beam combiner and a pulse compressor. It also contains the control electronics for coherent phasing of the parallel fiber amplifiers.

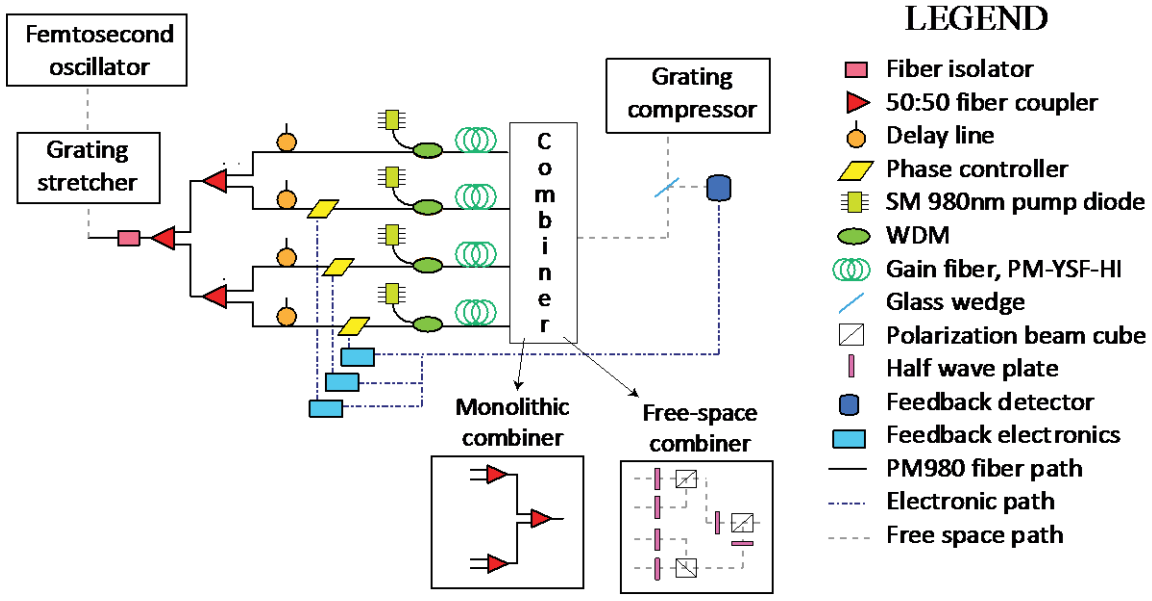

Figure 5.1 Experimental setup for four channel monolithic fiber pulse combining.

The femtosecond oscillator is an All Normal Dispersion (ANDi) femtosecond fiber oscillator [99] producing 7 nm bandwidth pulses at 1050.5 nm central wavelength and 47 MHz repetition rate with an average output power of 30 mW. Since this is a stretched-pulse oscillator, the pulses generated are positively chirped with a pulse duration of ~15 psec. After de-chirping, the duration of these pulses could be reduced to ~500 fsec. The seed pulses from the oscillator are stretched in a standard Martinez-type diffraction-grating pulse stretcher to about 900 psec. The pulse stretcher is arranged in a folded configuration (to reduce its length) and contains a single 10-cm wide grating with 1800 lines/mm groove density. The stretched pulses are coupled into a single-mode polarization maintaining (PM) fiber, and then split with a 50:50 single-mode fiber splitter arrangement, shown in Fig. 5.1, into four separate channels. Parallel amplification channels were built using standard single-mode PM fiber components (based on PM980 fiber for passive components), and all four channels were comprised of identical components with identical fiber lengths to ensure that each optical path is of equal length and with equal amount of linear and higher-order dispersion. To achieve accurate optical-path matching each channel includes a compact adjustable delay line, described in more detail further in the text. For correcting the phase drift between the channels, three of the channels include fiber piezo-stretcher (PZT) based phase modulators. The one channel without the modulator had an equivalent length of identical passive fiber spliced into its path, to match that of a PZT stretcher. Amplification in each of the channels was implemented using standard in-core pumped Yb-doped single-mode PM fibers (PM-YSF-HI from Nufern), WDM components for combining pump and signal paths and

standard telecom-grade single-mode pump diodes with up to 600 mW of pump power at 980 nm. The total length of fiber in each individual channel was about 30 m.

Four parallel amplified signals at the output of the fiber array are beam combined using a binary-tree type of arrangement. In a series of experiments, we interchangeably used both bulk-component and all-fiber based beam combiners. For the bulk combiner, we used a PBS-tree arrangement to implement polarization combining [83]. The all-fiber beam combiner used a 50:50 single-mode PM fiber arrangement, which is essentially a "reverse" of the signal splitter at the array input. It is clear, however, that an all-fiber beam combiner is incompatible with high power combining or high pulse energies. The reason this monolithic arrangement was used was to achieve an accurate measurement of array-phasing performance. Indeed, in this all-fiber beam combiner, complete beam overlap between all combined signals is automatically ensured. Therefore, all the effects on the combining efficiency associated with a non-perfect spatial beam overlap [77] are eliminated, and the combining efficiency is determined solely by interferometric addition of errors between different channels, allowing very accurate measurement of the phasing effects.

A combined beam of stretched and amplified pulses was launched into a standard Treacy-type diffraction grating compressor. Just like the stretcher, the compressor was arranged in a folded configuration, and therefore, uses only a single diffraction grating, identical in specifications to the one used in the stretcher. A small fraction of the output power is "sampled" by either a glass wedge placed prior to the compressor, or alternatively, by zero-order reflection from the compressor grating. The "sampled" beam is directed onto a single detector to provide a feedback signal for active phase locking.

Without phase locking (i.e. free running operation, open control loop) the relative phases between channels drift, resulting in random output power fluctuations after the combiner. This is of course expected, since without phase control, time-varying random constructive or destructive interference occurs between the channels. Using a feedback loop set to maximize the output power forces the channels to interfere constructively. The feedback signal contains the phase error information for each of the three of the channels with PZT modulators (the phase error is with respect to the fourth, i.e. reference, channel). The phase error signals are individually extracted with three separate feedback electronic signal processing units and the appropriate error canceling signals sent to the phase controllers, using the so-called LOCSET scheme, described in more detail further in the text.

5.2.2 Equalization of Parallel-Channel Optical Paths

Coherent combining of ultrashort optical pulses requires not only robust phasing, but also accurate matching of the group delays between parallel channels, so that the combined pulses are exactly overlapped in time. Errors in timing cause both pulse distortions and a loss in combining efficiency. In practice, acceptable group-delay errors should be much smaller than the pulse duration, and for femtosecond pulses should be on the order of few micrometers. Achieving such fiber-length accuracy by simply cutting the fiber is not practical. Instead, an arrangement for adjustable fiber length control should be used. Implementing adjustable length control in an array consisting of a large number of parallel channels has to be compact and cost-effective to manufacture. With this practical constraint in mind, we demonstrate an adjustable and compact delay line built using standard single-mode fiber based micro-optical components. The schematic of this

arrangement and its 3D rendering is shown in Fig. 5.2. The adjustable delay line exploits the non-reciprocal nature of a fiber circulator. An input pulse is sent into port 1 of a fiber circulator, it then travels out of port 2 with a spliced-on fiber collimator, and in free space propagates over a variable length (i.e. the delay) before being retro-reflected back into port 2 with a micro-optic mirror. Adjustment of the double-pass delay in this arrangement has been achieved with a compact micro-optical linear translation stage. After coupling back through the collimator into the single-mode fiber of port 2 the delayed pulse passes the circulator the second time and due to the circulator non-reciprocity is directed out of port 3. This configuration was selected since it minimizes the number of free-space degrees of freedom need for signal back-coupling adjustment – only two angular adjustments of only the reflecting mirror are needed. The insertion loss of this delay line is approximately 6 dB.

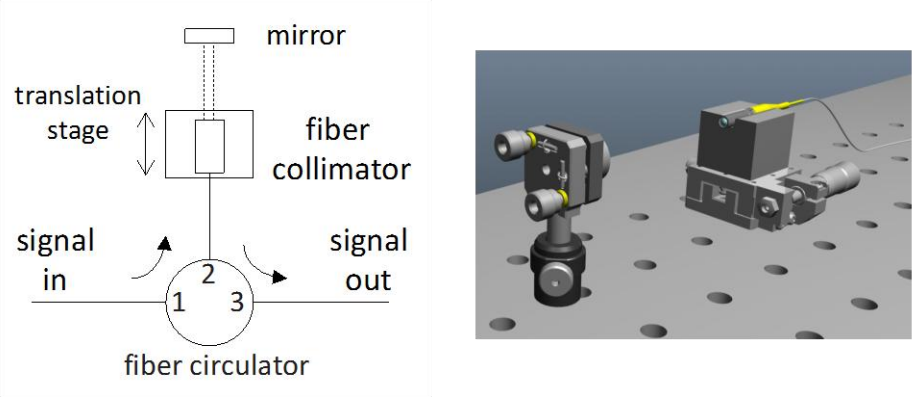

Figure 5.2 Schematic and 3D rendering of the micro-optic delay line.

During combining experiments, we observed that it was very important to match dispersions of the parallel channels. A four-channel array needs only three adjustable delay lines to achieve complete equalization between all four channels. Therefore, in an early implementation of our four channel combining setup we did not include a fiber

circulator delay line in one of the channels (reference channel four). But each circulator introduces significant dispersion, which led to the unbalanced dispersion in the reference channel, and subsequently, inefficient combining of this channel with the other three. This inefficiency was completely eliminated after an identical circulator-based delay line was incorporated in the reference channel to equalize the dispersions between all four channels.

5.2.3 Channel Active-Phasing Control System

As stated earlier, the four-channel fiber CPA array setup was actively phased using a LOCSET approach. The optical phase in three of the channels was controlled using fiber piezo-stretchers (Optiphase, PZ1). The fourth channel was left as a reference for the phase controlled channels to match. The piezo-stretcher gives a π phase shift per 2.6 V of drive voltage. The maximum voltage range of the device is ±500 V and therefore supports up to 384π of continuous phase control. Our feedback electronics was limited to an output of ±5 V and therefore we used high-voltage amplifier chips to reach at least ±100 V (76π) driving voltages. If we just used the limited ±5 V (3.8π) range then there were temporary, once every ~30 sec, moments of unlocked operation lasting less than ~200 msec before the system relocked to a modulo 2π phase. The extended phase control range with the high voltage amplifiers eliminated these temporary unlocks.

In the self-referenced LOCSET technique for active coherent beam combining, a single detector is used to supply a feedback signal to each of the feedback electronic units [72]. The principle of this technique is to modulate each phase controlled channel with a unique radio frequency (RF) value. One channel remains unmodulated. The modulated channels are then phase controlled to track the phase of the unmodulated channel. A

single detector measures a photocurrent that includes a superposition of all the interference effects between the channels. Demodulation of this photocurrent by feedback electronic signal processing units is performed for each modulated channel. Since the channels have different RF modulations the demodulation can be tuned to isolate the error signal for just a particular channel. The result of the LOCSET scheme is an RF phase locked loop that stabilizes the phases of the modulated channels with respect to the unmodulated channel.

The choice of values for RF modulation depends on how quickly the phase of a channel fluctuates. To determine the appropriate RF values, we first monitored the interferometric power fluctuations from the channels without feedback control (i.e. in the free running state, open control loop). In this case, the interference varies randomly over time and gives an indication of the phase noise. Fig. 5.3 shows measurements of the fluctuating power in both the time and frequency domains. The frequency domain data was obtained by taking a ten second interval of data at 1 kHz sampling rate, subtracting out the mean, and then performing a Fast Fourier Transform. The DET data shows our detector noise when there is no optical power on the detector.

We see that the interferometric power fluctuations drift slowly, indicating that the primary sources of noise are acoustic vibrations and temperature drifts. Experiments with cw fiber laser combining also confirm that noise is dominated by frequencies below 1 kHz [75,76]. We determined that RF modulation frequencies in the kilohertz range are sufficiently within the low-noise regime of our environment. In our multi-channel experiments, the modulation frequencies were set to 5 kHz, 6 kHz, and 7.5 kHz. The

integration time of the feedback electronics was set to 50 msec. This allowed the phase control loop to cancel phase disturbances up to 20 Hz in frequency.

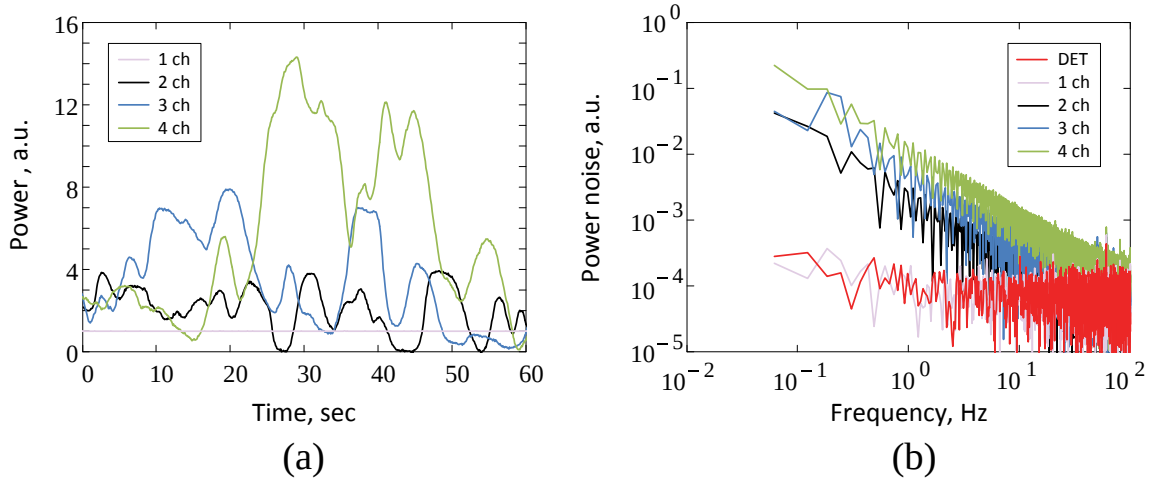

Figure 5.3 Power noise in the unlocked state for one, two, three, and four channels: (a) time domain, (b) frequency domain. The DET data indicates our detector noise floor.

5.3 Results

5.3.1 Combined Pulse Temporal Quality

The first performance metric for our multi-channel pulse combining system was the combined pulse quality. We measured the spectrum and autocorrelation for the recombined pulse and compared them to the individual channel measurements. Fig. 5.4 shows that the spectra and autocorrelation traces of the individual and combined four channels overlap with each other. Deconvolving the measured autocorrelation trace of the four channel combined pulse with a calculated pulse shape factor gives a pulse duration of 524 fsec. This compares to 410 fsec for the bandwidth limited pulse duration. The overlap of individual and combined channel autocorrelations shows that the temporal pulse quality is preserved in our multi-channel combining system.

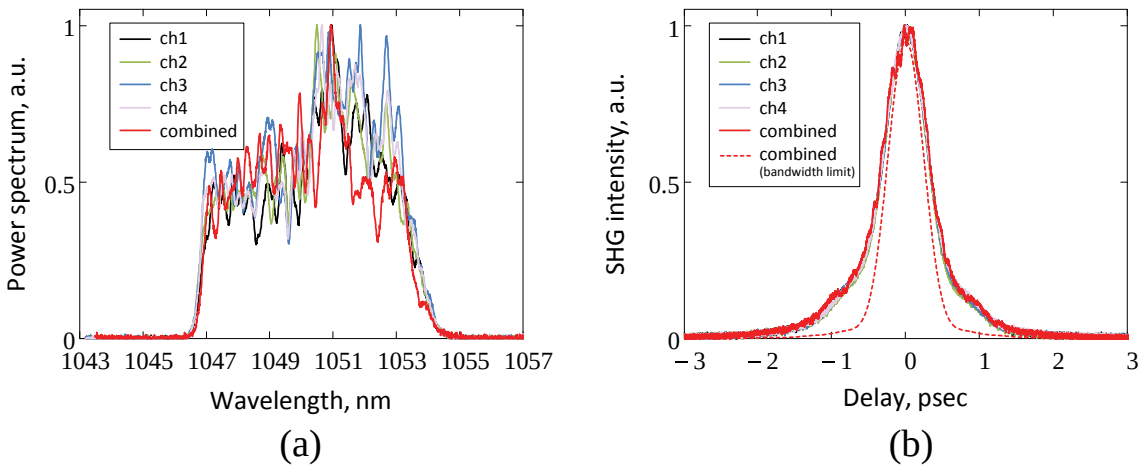

Figure 5.4 Pulse quality results: (a) normalized spectrum of individual channels and all four channels combined, (b) normalized autocorrelation traces of individual channels and all four channels combined – the dashed line shows the calculated (from the spectral measurement) bandwidth limited autocorrelation of the combined pulse.

5.3.2 Combining Efficiency vs. Time

Aside from combined pulse quality, the most important benchmark for pulse combining is the combining efficiency. Since the experimental setup was monolithically integrated, we only measured the power at the output of the system. To determine the combining efficiency, we first measured the power P_k from each channel k individually (i.e. we turned off the pump diodes and blocked the seed at the delay line for all channels $m \neq k$). Then, a coherent combining system with N+1 channels gives a *relative* combining efficiency that is

$$\eta = P_{\text{combined}} \Big/ \left(\sum_{k=0}^{N} P_k + \sum_{k=0}^{N} \sum_{\substack{m=0, \\ m \neq k}}^{N} \sqrt{P_m P_k} \right) \tag{5.1}$$

where P_{combined} is the measured combined power. For example, two channels that are individually measured to be 1 mW give a theoretical maximum coherent output power of 4 mW according to Eq. (5.1). This is not a violation of energy conservation because in

our experimental arrangement we are measuring the power *after* beam splitting elements. Thus a measured power of 1 mW from a single channel corresponds to 2 mW *before* splitting by an ideal 50:50 lossless coupler. Two channels, each with 2 mW can therefore provide a maximum output power of 4 mW. The individual channels, as well as the combined channels, exhibited a polarization extinction ratio of about 20.5 dB. The relative combining efficiency is calculated with the power at a single polarization state. The absolute efficiency of the system requires including the 1.2 dB insertion loss from each 50:50 fiber coupler.

Fig. 5.5(a) shows the relative combining efficiency for two, three, and four channels over a time period of five minutes. The mean efficiency is 96.4%, 94.0%, and 93.9% for two, three, and four channel combining respectively. Even though different combinations of channels can be used for two and three channel combining, the results are within 1% of each other. In the four channel experiment the mean combining efficiency corresponded to 58.6 mW of optical power. Observing the electronic error signals on an oscilloscope indicated that the channel phase errors drifted over a range of less than 20π during this time. Fig. 5.5(b) compares the power noise of the locked four channel result with the previous, Fig. 5.3(b), unlocked four channel measurement. We see that at the frequencies measured, the locked result is within the measurement floor of our detector.

Fig. 5.6 shows that four channel combining is efficient over a longer period of time and even when we occasionally block the signal to the feedback detector. Without feedback the system drifts, but immediately recovers when the feedback signal is restored. These feedback ‘blocks’ lasted for less than one second and show that the combining efficiency can be re-stabilized with our electronic feedback system.

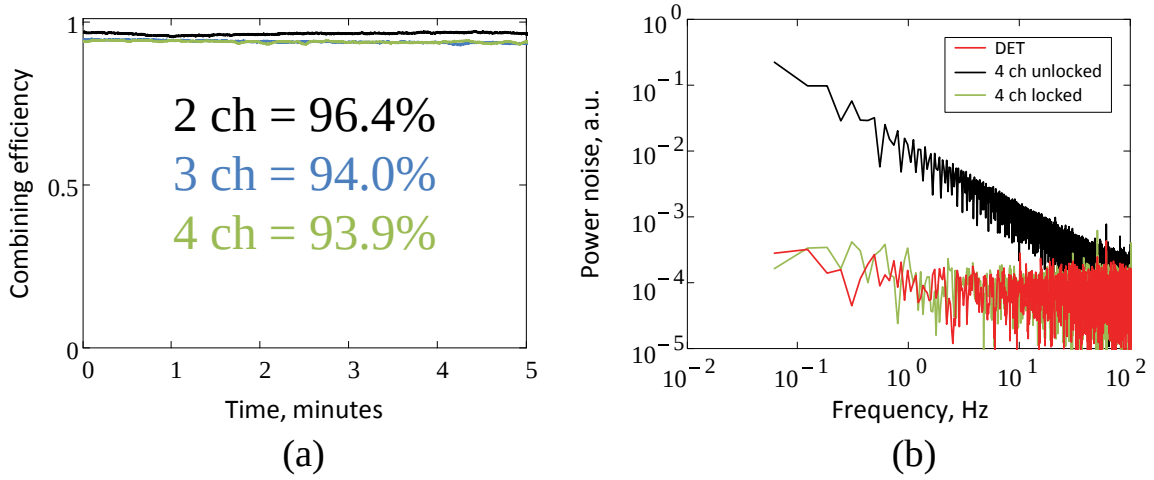

Figure 5.5 Combining efficiency and power noise: (a) combining efficiency for two, three, and four channel locking over a five minute time period, (b) four channel locked and unlocked noise.

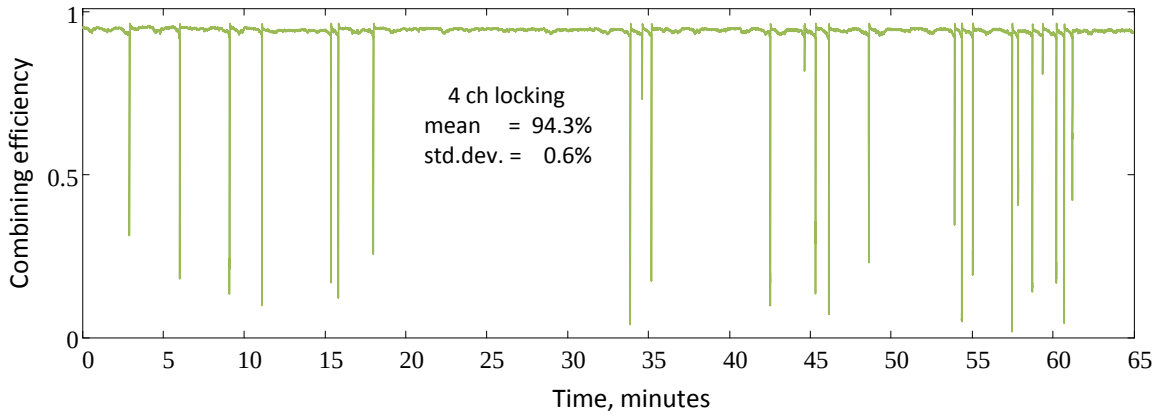

Figure 5.6 Four channel combining efficiency with feedback blocks. The momentary decrease in efficiency due to blocking and subsequent overshoot of our detector occurs in less than one second.

5.3.3 Combining Efficiency vs. Phase Modulation Amplitude

In the LOCSET method of active phase control, a small phase modulation is purposely applied to each of the phase controlled channels. The electric field of a phase controlled channel then varies as $cos\ (\omega_L t + \phi + \beta\ sin(\omega_{RF} t))$, where ω_L is the laser frequency, ϕ is an initial phase, ω_{RF} is an RF modulation frequency, and β is the phase modulation amplitude. An important question to address is how the phase modulation amplitude

affects the combining efficiency. Analytically, the combining efficiency as a function of modulation amplitude can be shown to be (see Section 5.6: Appendix)

$$\eta(\beta) = \left\{ \sum_{k=0}^{N} P_k + \sum_{k=1}^{N} 2\sqrt{P_0 P_k}\, J_0(\beta) + \sum_{k=1}^{N} \sum_{\substack{m=1,\\ m\neq k}}^{N} \sqrt{P_m P_k}\, J_0^2(\beta) \right\} \Big/ \left(\sum_{k=0}^{N} \sqrt{P_k} \right)^2 \qquad (5.2)$$

where J_0 is a Bessel function of order zero of the first kind and P_i is the individual output power from channel i. Fig. 5.7(a) compares the theoretical combining efficiency given by Eq. (5.2) to experimentally measured values of combining efficiency at different phase modulation amplitudes. Results are given for two, three, and four channel combining. We see that the experimental efficiency follows the theoretical trend towards decreasing combining efficiency. It is therefore desirable to operate at the smallest phase modulation amplitude that supports stable locking. In our system, this value was $\beta \approx 0.25$. Other electronic implementations of LOCSET feedback control have demonstrated stable locking of cw fiber lasers at $\beta = 0.10$ [73].

For a fixed β value, the theoretical combining efficiency given by Eq. (5.2) is plotted in Fig. 5.7(b) as a function of the number of channels under the assumption that all individual channel powers are equal. Figure 5.7(b) shows the dependence on channel number for three different β values. What is noteworthy is that the efficiency converges to a stable value as the number of channels is increased. In fact, by taking the limit of Eq. (5.2) as N goes to ∞ we get $\eta(\beta) = J_0^2(\beta)$. At $\beta = 0.25$ the theoretical efficiency converges to 96.9%.

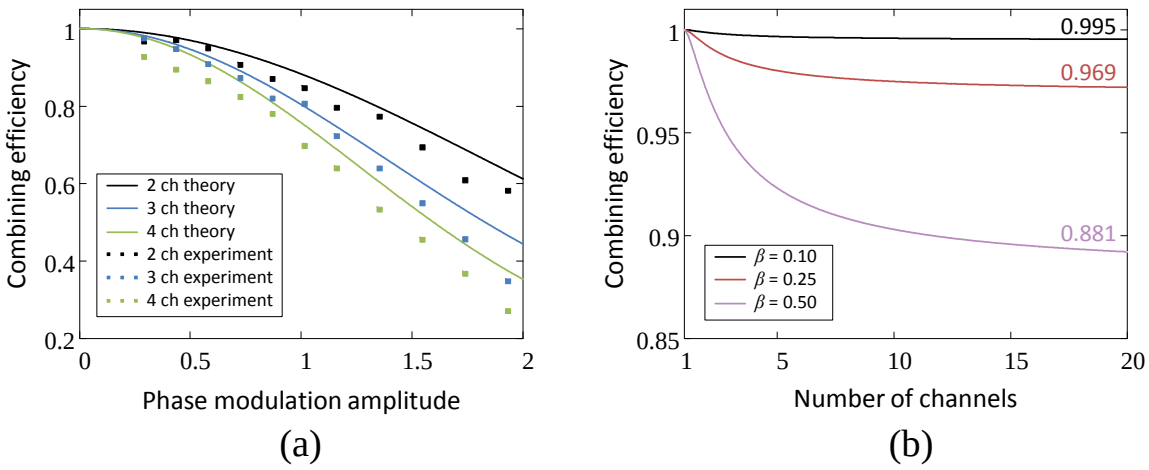

Figure 5.7 Effect of phase modulation on the combining efficiency: (a) experimental and theoretical combining efficiency as a function of phase modulation amplitude, (b) theoretical combining efficiency as a function of number of channels for different values of phase modulation amplitude.

5.4 Discussion on Scalability

The scalability of our fiber pulse combining system to larger numbers of channels was considered theoretically in Fig. 5.7(b) for different phase modulation amplitudes only. That analysis assumed equal channel powers (P_i = const) and perfect phase locking ($\phi_i = 0$). To generalize the situation we need to revisit the derivations in the section 5.6: Appendix. First of all, Eq. (5.5) expresses the electric field only *after* combining. Likewise, Eq. (5.8) expresses the maximum power only *after* combining. But we really want to compare the output combined power to the total power *before* combining. To do so, consider an N+1 combiner that operated in reverse has a uniform splitting ratio among the channels. This requires us to replace the powers P_i in Eq. (5.2) with $P_i/(N+1)$. Second, we do not set the phases ϕ_i equal to zero when going from Eq. (5.5) to Eq. (5.11) and therefore Eq. (5.2) includes ϕ_i as variables. Finally, the maximum power given by Eq. (5.8) is replaced by the sum of the powers P_i. Then, the generalized efficiency is

$$\eta = \frac{1}{(N+1)\sum_{k=0}^{N} P_k}\left[\sum_{k=0}^{N} P_k + \sum_{k=1}^{N} 2\sqrt{P_0 P_k}\cos(\phi_k - \phi_0) J_0(\beta) + \sum_{k=1}^{N}\sum_{\substack{m=1,\\ m\neq k}}^{N} \sqrt{P_m P_k}\cos(\phi_k - \phi_m) J_0^2(\beta)\right] \tag{5.3}$$

To analyze Eq. (5.3) from a statistically viewpoint, we make the assumption that the channel powers P_i are independent Gaussian random variables with mean P_{avg} and standard deviation σ_P, and that the phases ϕ_i are independent Gaussian random variables with zero mean and standard deviation σ_ϕ. For these random variables, the following expressions for expected value are useful in simplifying Eq. (5.3): $E\{cos(\phi_i - \phi_j)\} = exp(-\sigma_\phi^2)$ and $E\{\sqrt{P_i P_j}\} = P_{avg}\left[1 - \frac{1}{8}\left(\frac{\sigma_P}{P_{avg}}\right)^2 - \frac{3}{16}\left(\frac{\sigma_P}{P_{avg}}\right)^4\right]^2$. The expected value of Eq. (5.3) is

$$< \eta >= \frac{N + 1 + \left[1 - \frac{1}{8}\left(\frac{\sigma_P}{P_{avg}}\right)^2 - \frac{3}{16}\left(\frac{\sigma_P}{P_{avg}}\right)^4\right]^2 e^{-\sigma_\phi^2} J_0(\beta)[2N + N(N-1)J_0(\beta)]}{(N+1)^2} \tag{5.4}$$

With Eq. (5.4) we have a formula for combining efficiency in terms of the variables N, σ_P/P_{avg}, σ_ϕ, and β. For calculations, we assume that locking occurs at $\beta = 0.25$ (the value we currently are able to achieve stable locking). Fig. 5.8 plots Eq. (5.4) versus number of channels for different power variations σ_P and different phase errors σ_ϕ. In both cases the efficiency saturates for large numbers of channels. We see that the combining efficiency is relatively insensitive to power errors, as is well known in the literature [81]. The scalable efficiency with phase errors, shown in Fig. 5.8(b), remains above 80% for root-mean-square errors smaller than λ/15.

It is important to note that this scalability analysis is limited to errors in the time domain (recall that the electric field in Eq. (5.5) is written only with time as a variable). For our monolithically integrated combining system it is appropriate to neglect spatial errors since the waveguide geometry automatically overlaps Gaussian spatial modes of different channels. But high power systems must use free-space combining arrangements. For a filled-aperture architecture, the possibilities include using polarization beam splitters [83], a diffractive optical element [84], or a hollow-core waveguide [85]. In these cases, spatial errors, particularly wavefront errors, have a dominant effect on reducing the combining efficiency [77].

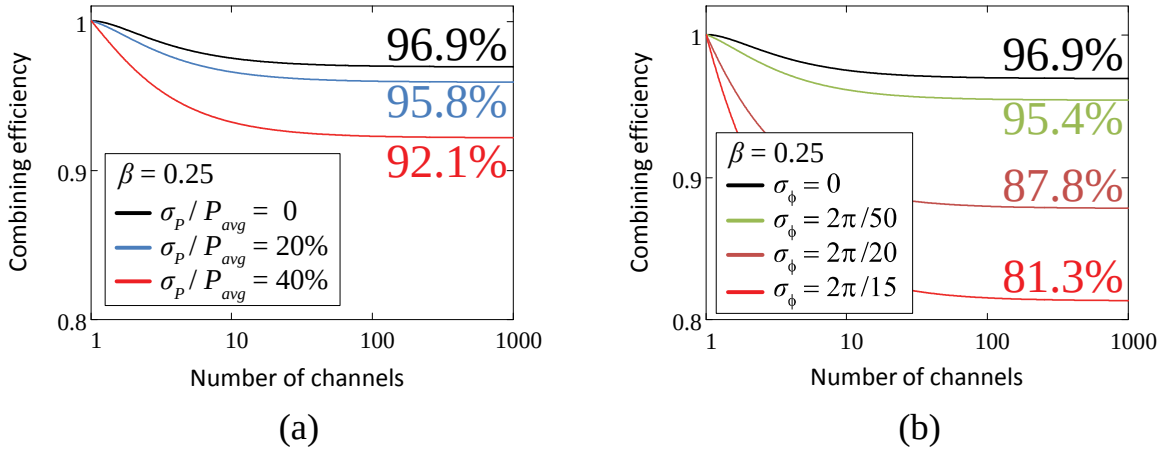

Figure 5.8 Scalability of a multi-channel combining system with LOCSET locking at $\beta = 0.25$ and different magnitudes of errors: (a) only power variation errors, (b) only temporal phase errors.

Nevertheless, what separates pulse combining from cw combining are temporal/spectral effects. Thus the same strategies used to minimize spatial errors in cw combining architectures can be used for pulse combining architectures. In the time domain we have shown that LOCSET feedback control is scalable to large numbers of channels. Moreover, the broad spectral bandwidth of ultrashort pulses offers new opportunities in coherent combining previously unexplored with cw combining systems.

5.5 Conclusion

We have demonstrated a multi-channel fiber femtosecond pulse combining system with 96.4%, 94.0%, and 93.9% relative combining efficiencies for two, three, and four channels respectively. The design of the system is simple, compact, cost efficient and scalable to larger numbers of channels in the future. The pulse duration of the combined pulses (524 fsec) matches the pulse duration from individual channels, showing that pulse quality is preserved in a multi-channel pulse combining system. Our analysis of temporal amplitude and phase errors shows that LOCSET feedback control is scalable to larger numbers of channels. Coherent combining of femtosecond pulses in multi-channel parallel fiber CPA systems offers a possible path towards simultaneously generating high energy and high average power ultrashort laser pulses.

5.6 Appendix

Here we show how the analytical expression for combining efficiency as a function of phase modulation amplitude, Eq. (5.2), is derived. The combined electric field in the time domain from a system employing the self-referenced LOCSET technique [73] can be written as

$$E_{\text{Total}}(t) = E_0 \cos(\omega_L t + \phi_0) + \sum_{k=1}^{N} E_k \cos(\omega_L t + \phi_k + \beta_k \sin(\omega_k t)), \qquad (5.5)$$

where N is the total number of phase-modulated elements, E_0 and E_k are the field amplitudes for the unmodulated and k^{th} phase modulated elements, ϕ_0 and ϕ_k are optical phases, ω_L is the laser frequency, ω_k is an RF modulation frequency, and β_k is a phase modulation amplitude.

For calculations we assume the phase locked condition and set ϕ_0 and ϕ_k equal to zero. The phase modulation amplitudes are all set to the same value β. The combined power P

is equal to the total field squared (to within a proportionality constant) and when averaged over a time T that is larger than the optical period ($2\pi/\omega_L$) but smaller than any of the modulation periods ($2\pi/\omega_k$) gives

$$P(t,\beta) = \frac{1}{T}\int_{t-\frac{1}{2}T}^{t+\frac{1}{2}T} |E_{\text{Total}}(\tau)|^2 d\tau$$

$$= \frac{1}{2}\sum_{k=0}^{N} E_k^2 + \sum_{k=1}^{N} E_0 E_k \cos(\beta \sin(\omega_k t)) + \frac{1}{2}\sum_{k=1}^{N}\sum_{\substack{m=1,\\ m\neq k}}^{N} E_m E_k [\cos(\beta \sin(\omega_k t)) \quad (5.6)$$

$$\times \cos(\beta \sin(\omega_m t)) + \sin(\beta \sin(\omega_k t)) \sin(\beta \sin(\omega_m t))].$$

As seen in Eq. (5.6) the combined power is still time dependent and depends on the phase modulation amplitude β. Our feedback detector does indeed measure the time dependent combined power (this is necessary because the feedback electronics have to demodulate the individual RF modulations), but when measuring combining efficiencies we used a slower detector that did not respond to the modulation time dependence. Therefore the measured time averaged power is given by

$$P(\beta) = \frac{1}{T_2}\int_0^{T_2} P(t,\beta) dt, \quad (5.7)$$

where T_2 (the response time of the slow detector) is several times greater than $2\pi/|\omega_k - \omega_m|$ for any possible k and m values. The theoretical maximum combined power occurs in the limit of β equal to zero and is given by

$$P_{\max} = \frac{1}{2}\left(\sum_{k=0}^{N} E_k\right)^2. \quad (5.8)$$

The combining efficiency as a function of β becomes

$$\eta(\beta) = P(\beta)/P_{\max}. \quad (5.9)$$

Using the Fourier series expansions

$$\cos(\beta \sin(\omega_k t)) = J_0(\beta) + 2\sum_{m=1}^{\infty} J_{2m}(\beta)\cos(2m\omega_k t)\,,$$
$$\sin(\beta \sin(\omega_k t)) = 2\sum_{n=1}^{\infty} J_{2n-1}(\beta)\sin((2n-1)\omega_k t), \tag{5.10}$$

where J_m is a Bessel function of order m of the first kind to rewrite the terms in Eq. (5.6), we substitute Eq. (5.6) into Eq. (5.7), take the asymptotic limit for large T_2, and calculate the combining efficiency from Eq. (5.9) to give

$$\eta(\beta) = \left\{\sum_{k=0}^{N} E_k^2 + \sum_{k=1}^{N} 2E_0 E_k J_0(\beta) + \sum_{k=1}^{N}\sum_{\substack{m=1,\\ m\neq k}}^{N} E_m E_k J_0^2(\beta)\right\} \Big/ \left(\sum_{k=0}^{N} E_k\right)^2 . \tag{5.11}$$

Eq. (5.11) is equivalent to the desired result, Eq. (5.2), when written in terms of powers rather than electric field amplitudes.

CHAPTER 6

Femtosecond Pulse Spectral Synthesis in Coherently Combined Multi-Channel Fiber Chirped Pulse Amplifiers

6.1 Introduction

Gain narrowing is a critical issue for laser community since it reduces the optical bandwidth and therefore increases the pulse duration. Like Yb-doped fiber exhibiting a gain bandwidth of over 100 nm, chirped pulse amplification (CPA) of such a broad bandwidth pulse is not possible with a single Yb-doped fiber amplifier because gain narrowing limits the amplified spectrum to approximately 10-20 nm in high gain systems.

For years, in the continuous-wave domain, some solution like gain flattening to compensate the gain narrowing has been widely studied in the wavelength-division-multiplexed communication systems [102-108]. However, in the ultrafast domain, there is no promising method to surpass this barrier yet.

The most important feature of gaining narrowing is the large gain excursion over the gain profile. If the overall bandwidth of a chirped femtosecond pulse can be divided by several spectral slices, amplify each individual slices and synthesize from them coherently combined with the same whole bandwidth, then it is expected the gain excursion in each spectral slice can be minimized and therefore gain narrowing can be eradicated.

In a recent decade, two independent femtosecond lasers with different spectra have been coherently combined to synthesize a wider bandwidth pulse with shorter pulse duration than either of the two lasers individually [109-111]. Furthermore, efficient active coherent combining of multi-channel fiber CPA systems has also been demonstrated [12,71,112]. Progress on ultrashort pulse coherent combining, in particular [111], seems to create some possibility to implement the aforementioned new idea to beat gain narrowing. However, due to the complexity of setup and low combining efficiency for two-channel result, it is difficult to use their setup for multi-channel spectral synthesis. A better method for scalability and good efficiency is required.

In this chapter, we first explain conceptually how to implement this new idea by exploring phase locking scheme and combining efficiency under a scalable configuration. Then, we experimentally realize this new idea by demonstrating femtosecond pulse synthesis based on coherently combined three parallel fiber CPA channels with three partial-overlapped or three adjacent non-overlapped spectral slices using linear or two-photon-absorption (TPA) operations, respectively. Later, we compare the individual experimental results and discuss their pros and cons. Since this demonstration can achieve high combining efficiency, it opens a new way to defeat the gain narrowing limitation.

6.2 Concept

The key issue to implement the new idea of spectral pulse synthesis for defeating gain narrowing relies on a scalable architecture as proposed in Fig. 6.1. A broadband modelocked laser source is first stretched and then split into N-channel distinct spectra via N-channel spectral splitter. After the amplification of each channel, all N channels are

coherently recombined via N-channel spectral combiner into a combined pulse with the same original bandwidth, which is later recompressed as the output pulse. To perform N-channel coherently combined, a feedback system is required to compensate the phase difference of individual channel relative to the reference one so that N-channel phase locking can be achieved. Moreover, to make N-channel combining practical, high combining efficiency is also required. Therefore, phase locking strategies and combining elements plays the most critical roles to make this scalable layout working.

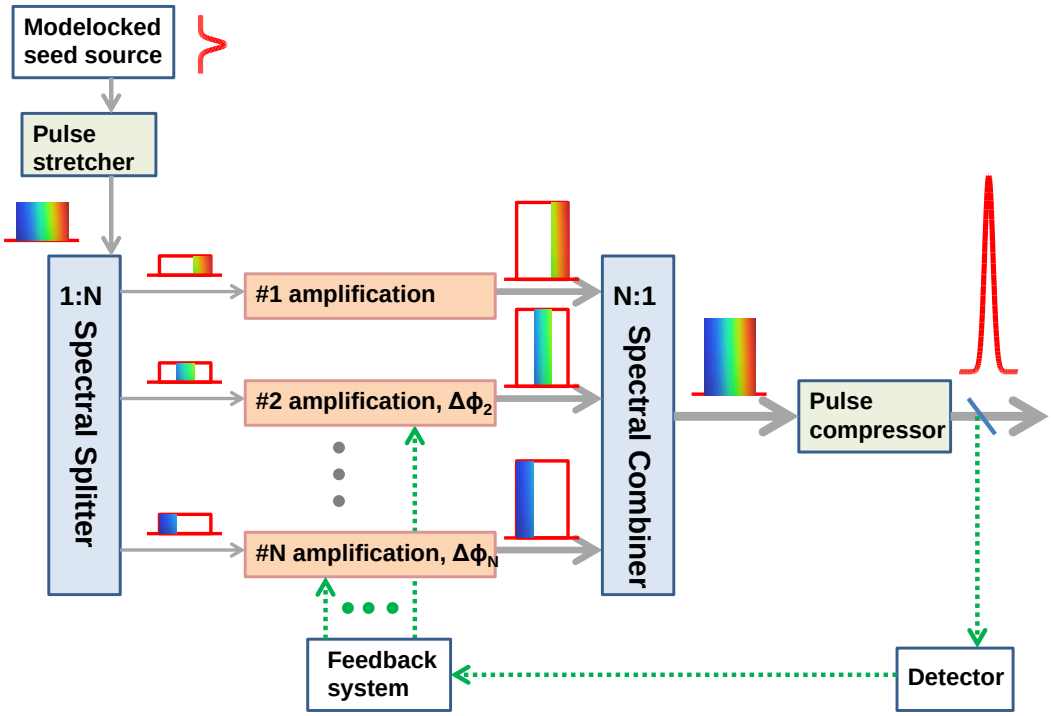

Figure 6.1 The schematic N-channel setup for pulse synthesis. $\Delta\phi_i$=ith channel phase error with respect to the reference channel, channel 1.

6.2.1 Phase Locking Strategies

There are two approaches for the feedback system to identify the phase error and thus to attain phase locking: One is partial spectral overlap approach in which distinct spectral slices are arranged partially overlapped to provide some interference for regular linear

detector to detect the phase-induced power variation; the other is no spectral overlap approach in which separate spectral pieces are assigned to be adjacent non-overlapped to one another. Due to no interference, only nonlinear processes are possible to track down the phase difference. In this experiment, we consider two-photon-absorption (TPA) processes and investigate 2-channel condition as follows since multi-channels can always break down to multiple pairs of 2-channel.

Assume P_1 and P_2 as the first and second power spectra amplitude having ω_1 and ω_2 central angular frequencies and $\Delta\omega_1$ and $\Delta\omega_2$ bandwidths, respectively, then their individual E-fields in the frequency domain can be denoted by Eqs. (6.1) and (6.2).

$$E_1(\omega - \omega_1) = \sqrt{P_1(\omega - \omega_1)} \tag{6.1}$$

$$E_2(\omega - \omega_2) = \sqrt{P_2(\omega - \omega_2)} \tag{6.2}$$

Assume two spectra have θ phase difference, then the instantaneous intensity in time domain I(t,θ) can be evaluated by the absolute square of the Fourier transform $\mathcal{F}$ of the sum of two E-fields with phase difference as Eq. (6.3). Since the linear detector is a slow detector, it actually detects the time-averaged intensity $I_{avg}(\theta)$ over a sufficient enough time window T as Eq. (6.4). Then the linear visibility (V_{Linear}) between in-phase (θ=0) and out-of-phase (θ=π) time-averaged intensities can be defined as Eq. (6.5).

$$I(t,\theta) = \left|\mathcal{F}\left\{E_1(\omega - \omega_1) + E_2(\omega - \omega_2)e^{i\theta}\right\}\right|^2 \tag{6.3}$$

$$I_{avg}(\theta) = \frac{1}{T}\int_{-T/2}^{T/2} I(t,\theta)dt \tag{6.4}$$

$$V_{Linear} = \frac{I_{avg}(\theta = 0) - I_{avg}(\theta = \pi)}{I_{avg}(\theta = 0) + I_{avg}(\theta = \pi)} \tag{6.5}$$

For TPA process as a quadratic intensity effect, its instantaneous intensity in time domain $I^T(t,\theta)$ can be formulated by the absolute quadruple of the Fourier transform $\mathcal{F}$ of

sum of two E-fields with phase difference as Eq. (6.6). Since the TPA detector is also a slow detector, it actually detects the time-averaged TPA intensity $I_{avg}^{T}(\theta)$ over a sufficient enough time window T as Eq. (6.7). Then the TPA visibility (V_{TPA}) between in-phase ($\theta=0$) and out-of-phase ($\theta=\pi$) time-averaged TPA intensities over a sufficient enough time window T can be defined as Eq. (6.8).

$$I^T(t,\theta) = \left|\mathcal{F}\left\{E_1(\omega-\omega_1) + E_2(\omega-\omega_2)e^{i\theta}\right\}\right|^4 \tag{6.6}$$

$$I_{avg}^T(\theta) = \frac{1}{T}\int_{-T/2}^{T/2} I^T(t,\theta)dt \tag{6.7}$$

$$V_{TPA} = \frac{I_{avg}^T(\theta=0) - I_{avg}^T(\theta=\pi)}{I_{avg}^T(\theta=0) + I_{avg}^T(\theta=\pi)} \tag{6.8}$$

Eq. (6.5) follows the definition of fringe visibility in fundamental optics theory and thus ranges from 0 to 1. When there is no coherence, V_{Linear} =0; when there is total coherence, V_{Linear} =1; when there is partial coherence, V_{Linear} is between 0 and 1. For Eq. (6.8), we can regard it as a generalized sense of fringe visibility based on quadratic intensity.

In principle, when two spectra are totally non-overlapped, no feedback signal will be detected due to no coherence for linear condition; therefore, $V_{Linear=}0$. This result is verified in Fig. 6.2 where two spectra are assumed to be identical with 4-nm bandwidth as the parameter used in our experimental condition. Either rectangular or triangular spectral shapes, their linear visibility come to zero at zero spectral overlap. However, their TPA exhibits nonzero visibility, indicating that TPA can be used for phase locking under non-overlapped adjacent spectra if this nonzero visibility is larger than the signal-to-noise (SNR) ratio of TPA detector that decides the minimal required visibility for phase detection in the real experiments.

In general, rectangular spectral shape has better visibility than triangular since the former one is for ideal conditions whereas the latter one is close to real conditions after considering the edge steepness of spectral filters. As two spectra are totally overlapped, $V_{Linear}=V_{TPA}=1$ for both spectral shapes, which is an important benchmark to ensure the validity of Eqs. (6.5) and (6.8).

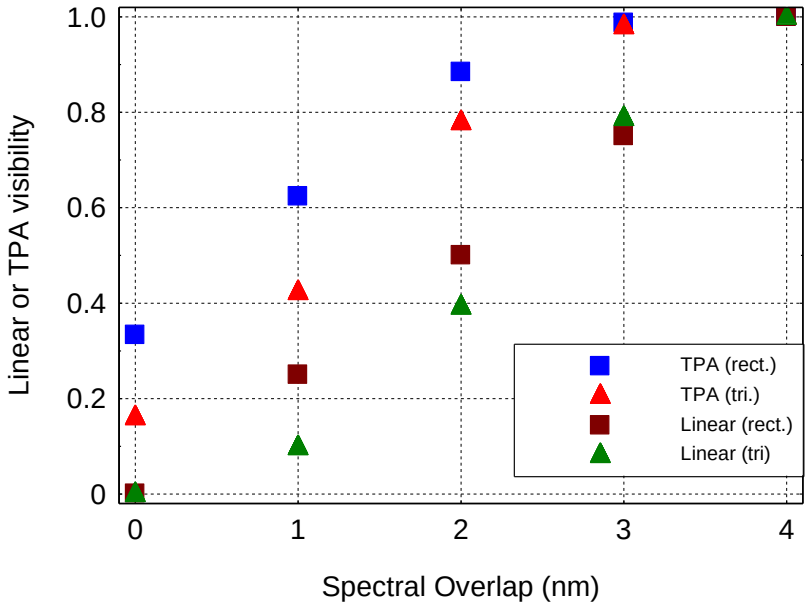

Figure 6.2 Linear visibility (V_{Linear}) and TPA visibiltiy (V_{TPA}) versus spectral overlap for rectangular and triangular spectral shapes.

6.2.2 Combining Elements

From the point of view of efficient combining for broadband multi-channel pulse synthesis like Fig. 6.1, uncompensated phase errors and lossy combining elements are the two major concerns for efficiency loss. Since our pulse synthesis experiment is established on the foundation of our 4-channel pulse coherent combining, the phase errors can be reasonably manageable to even large channel number due to the saturation predicted in our scalability formula [12]. However, for the lossy combining elements such as typical 50:50 beam splitters that can achieve at best 50% efficiency for two-

channel result [111], a better alternative becomes necessary. We therefore target on spectral filters-based combiner.

In principle, if the spectral filter behaves just like rectangular spectral function, either partial-overlap or non-overlap for any two adjacent spectra, the combining efficiency always reaches 100%. However, a real filter comes with a finite-width spectral steepness, which may contribute some efficiency loss due to unavoidable slope mismatch between spectra and the filter; therefore, in practice adjacent non-overlap spectral slices tend to have better efficiency than partial-overlap ones owing to the lower ratio of steepness mismatch.

In theory, we still can have 100% efficiency under the edgy spectral filter for the partial-overlap condition. Assume a super-gaussian spectrum (blue line in Fig. 6.3) with spectral intensity I_0 is split into two portions with an edge of a spectral filter. At each spectral position this filter acts as X:(1-X) splitter (magnitude of X is a function of wavelength), splitting the spectrum at a particular spectral position in Fig. 6.3 into two slices with spectral intensities I_1 and I_2 at this wavelength equal to $X \cdot I_0$ and $(1-X) \cdot I_0$, respectively.

Now consider the same filter being used as a beam combiner for exactly the same halves of the split spectrum. Then the combining efficiency (η) can be defined as Eq. (6.9)

$$\eta = \frac{\left(\sqrt{I_1 \cdot X} + \sqrt{I_2 \cdot (1-X)}\right)^2}{I_1 + I_2}. \tag{6.9}$$

After plugging $I_1 = X \cdot I_0$ and $I_2 = (1-X) \cdot I_0$ into Eq. (6.9), we get η=100%. In other words, if one considers X:Y splitter and two optical signals with the corresponding intensities

proportional to X and Y respectively, all incident power can be coherently combined into a single beam without any power loss

So the general conclusion is that for coherent spectral combining in principle one does not need to separate spectral slices apart to get 100% efficiency! 100% combining is in principle achievable in coherent combining of overlapping spectral splices, regardless of the spectral slope *provided that split-edge spectral shape is perfectly preserved between splitting and combining.* The latter condition of course puts practical constraints that might be not completely straightforward to implement, but it is still feasible.

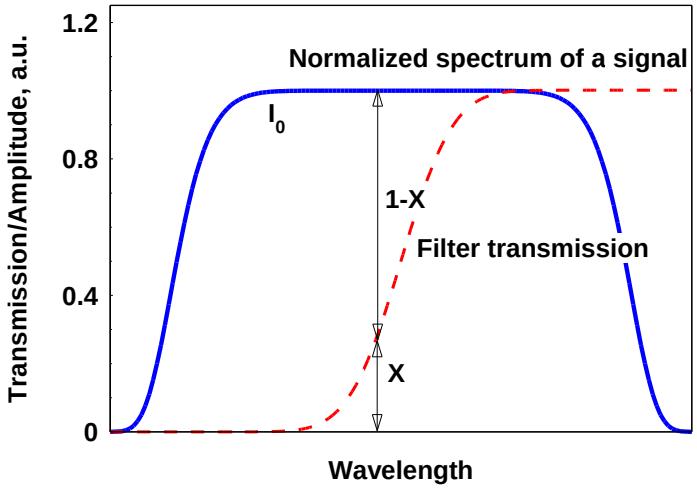

Figure 6.3 The schematic of a super-gaussian spectrum over the spectral filter transmission function.

6.3 Experimental Setup

The experimental setup of 3-channel pulse synthesis is shown in Fig. 6.4. A femtosecond seed source from the Nd:glass oscillator (central wavelength at 1059 nm, 72 MHz repetition rate, 12 nm spectral width) generates pulses that are stretched by a conventional diffraction-grating stretcher to around 500 ps in duration and coupled into a fiber CPA system. The stretched pulses are split into 3 channels and proceed to delay lines. The delay lines are composed of non-reciprocal fiber circulators, micro-optic

mirrors, and 4-nm bandwidth bandpass spectral filters (Semrock, LL01-1064-25). The first two are used to fine tune the delay within a range of 1 cm whereas the last one is placed in a free space portion to divide the channel spectra in to distinct parts.

In the linear detector case, we slightly overlap the spectra of adjacent channels so that without phase locking, some output power fluctuates due to random constructive and destructive interference from partially overlapped spectra, and thus can be used for feedback control. In the TPA detector case, we just slice the spectra into three non-overlap adjacent pieces.

After the delay line the pulses in two of three channels go to fiber piezo-stretchers (Optiphase, PZ1) for phase control. Following the piezo-stretchers the pulses are amplified with standard telecom grade single-mode pump diodes and PM fiber components. After amplification, the three separate channels are collimated out of the fibers into a free- space spectral combiner composed of 2 edge spectral filters (Semrock, LP02-1064RS-25). The combined pulse is then recompressed with a diffraction grating compressor. A small portion of the compressed output power is detected by the linear or TPA detector and served as a feedback signal with phase error information for two of three channels with respect to the reference channel. Through the self-referenced LOCSET technique [72,73] and two sets of home built feedback electronics, the phase error signal is individually extracted and sent to piezo-stretchers for phase compensation. A feedback loop that maximizes the linear or TPA intensity forces the channels to interference constructively and hence locks the phases of the separate channels.

In feedback system, the piezo-stretcher can provide a π phase shift per 2.6 V driving voltage and can be driven up to ±500 V equivalent to 384π continuous phase control.

Since our electronics are limited to an output of ±5 V (3.8π), we thus use the high-voltage amplifiers to reach at least ±100 V (76π) to attain long-time stable locking. Moreover, due to low-noise (<10 Hz) environment for slow phase drift and high repetition rate (72 MHz) of our oscillator, the integration time of 50 msec and the RF modulation/demodulation frequencies at 5 kHz and 6 kHz in feedback electronics are suitable for maintaining the self-referenced LOCSET techniques.

Owing to two different off-the-shelf types of spectral filters for splitting and combining the spectra, it is inevitable to consider their steepness mismatch. To achieve the best combining efficiency, for the linear case, we adjust bandpass and edge filters to let any two adjacent spectra to overlap the minimal detectable range so that phase locking still can be fulfilled as well as the power loss can be minimized.

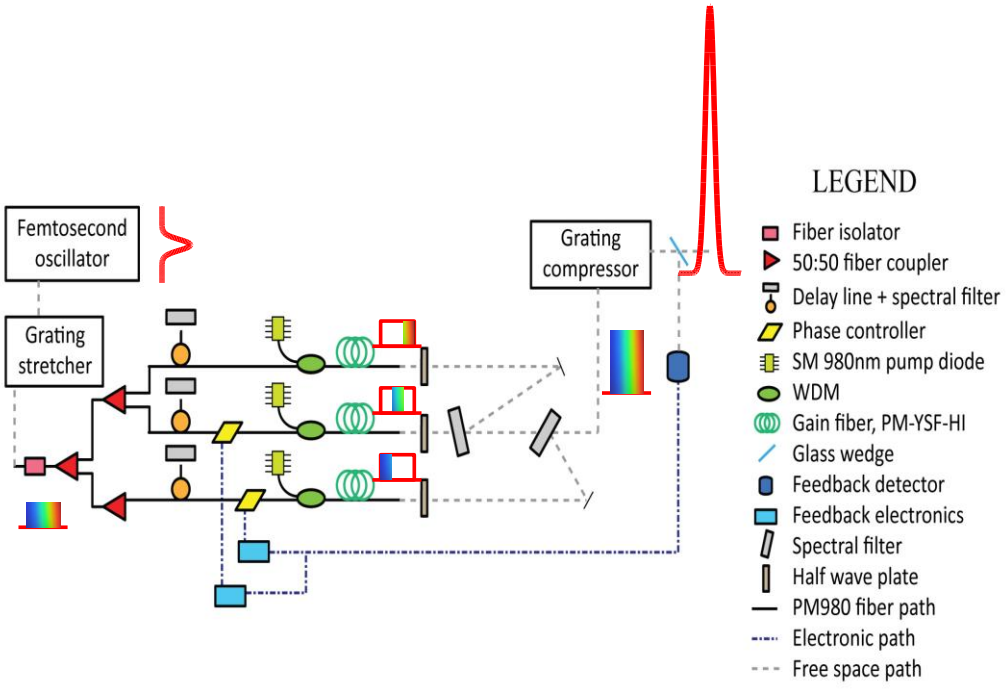

Figure 6.4 Experimental setup for three-channel pulse synthesis.

6.4 Experimental Results

The benchmarks of pulse synthesis are the coherently combined pulse with the duration much shorter than that of each individual channel and the combined pulse temporal quality.

In the linear detector case, the individual and combined channel spectra are shown in Fig. 6.5(a) where the overlap range between any two adjacent individual spectra is around 1 nm, which sets the minimal detectable range in our feedback system. The overall spectrum after combining three close-to-equal-width spectral slices is around 8 nm (full width half maxmium, FWHM). All individual spectral shapes look like triangular thanks to the edge steepness of bandpass and edge filters. The pulse quality is shown in Fig. 5(b) where the autocorrelation (AC) trace is measured by a SHG background-free autocorrelator. The deconvolved individual and combined pulse durations are 829 fs, 777 fs, 871 fs, and 403 fs, indicating the combined pulsewidth is approximately 2 to 3 times shorter than each individual ones. This combined pulse duration is close to the calculated transform-limited one, 363 fs, representing its good temporal pulse quality. The absolute combining efficiency and combined power are measured to be 76.3% and 257 mW. Since the spectral combiner have intrinsic loss from each filter with transmission (95%) and reflection (99.7%), it gives a theoretical maximum absolute efficiency of 94.9% in a 3-channel setup, referring to 18.6% additional efficiency loss from the slope mismatch between the bandpass and edge filters in each channel.

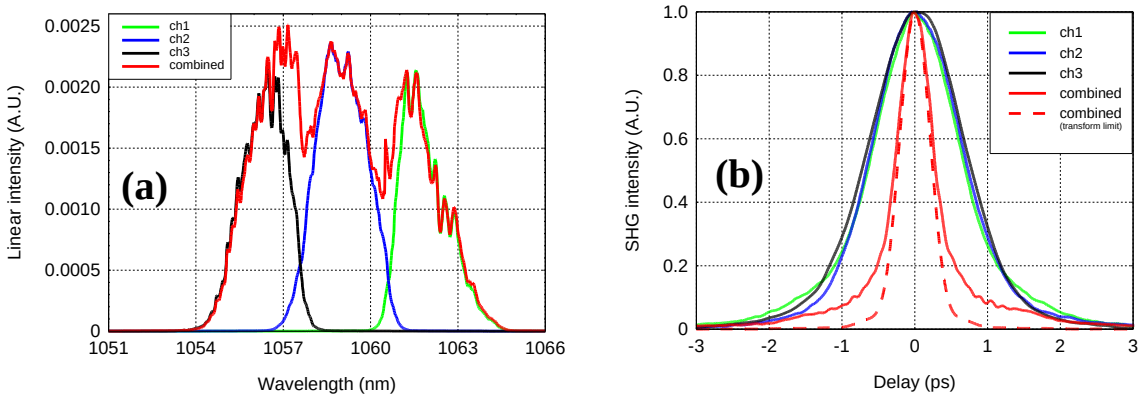

Figure 6.5 Linear detector results. (a) Spectra for the individual and combined channels; (b) normalized autocorrelation traces for the individual and combined channels. The dash line shows the calculated transform limited autocorrelation of the combined pulse.

Similarly, in TPA detector case, the individual and combined channel spectra are shown in Fig. 6.6(a) where two spectral gaps lie between three individual non-overlap triangular-like spectra. The overall combined spectrum FWHM span is around 10 nm over 3 close-to-equal-width individual spectra. The pulse quality is shown in Fig. 6.6(b) where the deconvolved separate and combined pulse durations are 1071 fs, 761 fs, 834 fs, and 356 fs. The combined pulsewidth is also approximately 2 to 3 times shorter than each individual ones and close to the calculated transform-limited one, 278 fs. However, unwanted pedestals in the combined as well as bandwidth-limited traces are observed. To clearly explore their origin, we thus use 2 identical 4-nm adjacent non-overlap spectra to calculate the AC traces for rectangular and triangular spectral shapes and discover that the spectral gap between two triangular spectra is the key to contribute the wings of the combined pulse in Fig. 6.7. This conclusion can be verified by the linear detector case for no pedestals in its combined AC trace since there is no down-to-valley spectral gap in Fig. 6.5(a). Moreover, higher wings are also observed in the measured trace than that of transform-limited due to the uncompensated high-order dispersion in the system. The

absolute combining efficiency and combined power are measured to be 85.8% and 273 mW. With 94.9% theoretical efficiency, 9.1% additional efficiency loss is from the steepness mismatch, which is lower than that of the linear detector case as expected and addressed in Section 6.2.2.

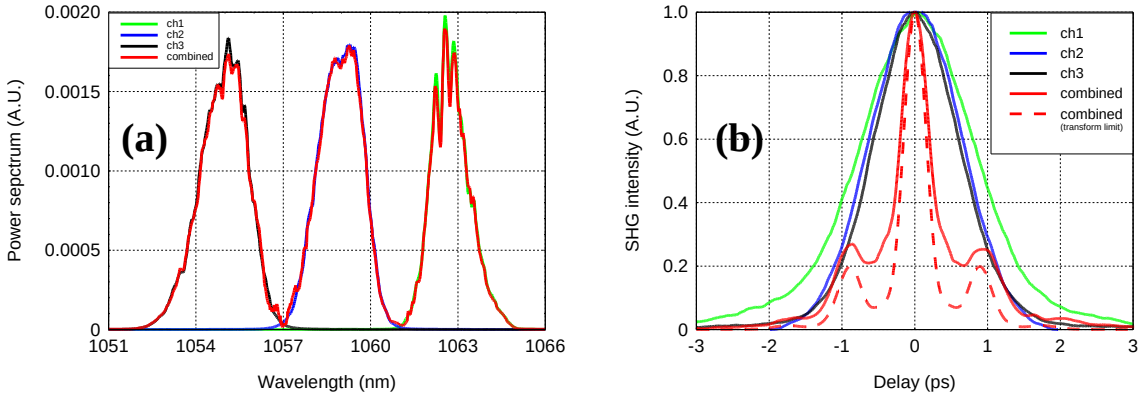

Figure 6.6 TPA detector results. (a) Spectra for the individual and combined channels; (b) normalized autocorrelation traces for the individual and combined channels. The dash line shows the calculated transform limited autocorrelation of the combined pulse.

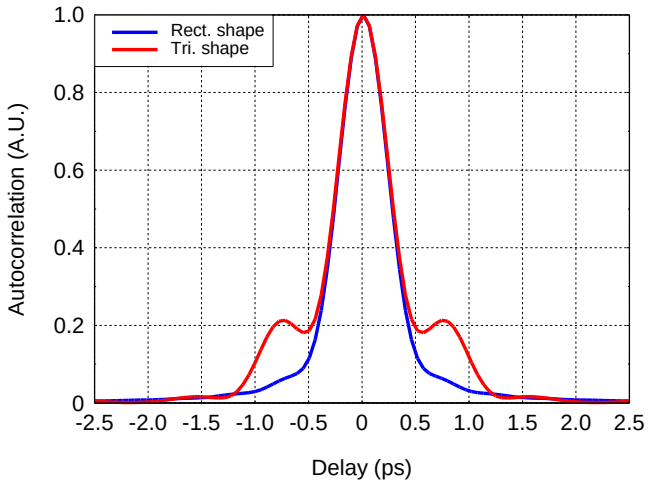

Figure 6.7 Autocorrelation trace of 2 adjacent non-overlap spectra for different spectral shapes.

Our pulse synthesis system exhibits stable locking for both cases as seen in Fig. 6.8. Since our setup is arranged to achieve the best combining efficiency, the ratio of overlap in the linear detector case is reduced up to the minimal detectable power fluctuation for

feedback control under the free running operation; therefore, the linear contrast of free-running intensity variation is expected to be small (~0.06 using Eq. (6.5)). On the other hand, the TPA contrast is relatively more promising (~0.16 using Eq. (6.8)).

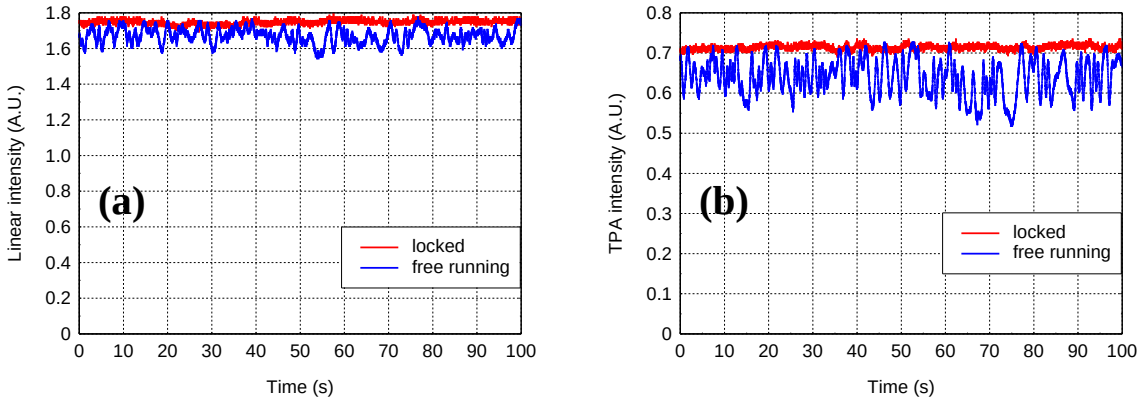

Figure 6.8 Locked and unlocked intensity variations for (a) linear detector case, and (b) TPA detector case.

6.5 Discussion

Although non-overlap approach by a TPA detector can detect feedback signal for adjacent non-overlap spectra and display better combining efficiency than that of partial-overlap approach by a linear detector when steepness mismatch between filters occurs, its bad pulse fidelity makes a linear detector case a better choice for pursuing good temporal pulse quality. Besides, if any two neighboring spectra can be designed closer to complement each other over a spectral combiner, then the combining efficiency of linear detector case can also be improved without sacrificing the pulse quality.

For feedback system, in addition to evaluating TPA contrast for phase locking, we also investigate the demodulation signal magnitude of $2\omega_{RF}$ and ω_{RF} from LOCSET theory to see whether $2\omega_{RF}$ has higher magnitude, assuming the responsitivity for both case is the same. It turns out that the demodulated magnitude of ω_{RF} is roughly double that of $2\omega_{RF}$ in this 3-channel setup so that it is better to use ω_{RF} as demodulated frequency.

In this chapter, we demonstrate the synthesis of femtosecond pulses by coherently combining spectrally distinct pulses from 3 parallel Yb-doped fiber CPA channels using linear and TPA detectors. This proof-of-concept demonstration with high combining efficiencies suggests a promising path for multi-channel pulse synthesis to potentially achieving pulses as short as ~30 fs with spectra accommodating complete gain band of Yb-doped or other fibers. In principle, the synthesis of signals simultaneously from different gain media can also be achieved.

CHAPTER 7

Summary and Future Work

7.1 Summary

In broadband passive coherent combining, the most important question is the scalability of coherent-combining efficiency with array size. To resolve this issue, we implement a systematic experimental study and propose a new propagation model.

Owing to the multiple-longitudinal-mode nature of fiber lasers and the natural selection of the resonant arrays modes that have minimum loss, this new model can characterize the dynamics of coherently combined modes so that the formation of supermodes can be understood. Meanwhile, the scalable experimental setup using 50:50 couplers makes it possible to explore the evolution of combining efficiency up to 16 channels with a 2-channel building block. The consistent conclusion between experiments and simulation indicate the combined-power efficiency falls off with array size due to the increasing scarcity of supermodes within the laser gain bandwidth. In the absence of an exact coincidence, the system will still find the least lossy mode but the significant energy will be coupled into the lossy ports due to the residual phase mismatch at the couplers.

The increasing power fluctuation with array size is also observed from experiments and numerically verified that small phase shift induced from the wavelength-scale fiber

length variation is an important factor to the instability of output power. For the hotly debated issue of intensity-dependent nonlinear phase shift in the literature to aid the combining efficiency, in our configuration, we notice the non-resonant nonlinearity broadens the spectral packet considerably in the power spectrum but generates larger phase mismatch in the multiple-coupler interferometer, resulting in the drop in combining efficiency.

To pursue practical multi-kW power scaling, the decreasing combining efficiency and the increasing power fluctuation with large array sizes are the two limitations for broadband passive coherent beam combining to be implemented.

In femtosecond pulse coherent combining, we demonstrate the four-channel pulse combining with simple, compact, cost efficient, and scalable configuration. Besides the detail discussion of experimental arrangements and concerns such as group delay matching using a delay line for fine tuning, noise measurement for deciding appropriate RF modulation frequencies and integration time of feedback electronics, channel dispersion matching, combined pulse temporal quality, and stable locking, another critical issue is to address the scalability of combining efficiency in terms of phase modulation depth, temporal amplitude, and phase error based on an analytical mathematical expression.

From this expression, we find out the combining efficiency saturates at large numbers of channels, meaning that this combining scheme can be scaled up to huge array sizes and present the potential to achieve the future goal of high-peak-high-average-power ultrashort laser pulses.

In pulse synthesis, we explore a scalable configuration by investigating the combining elements and phase locking strategies. We experimentally synthesize femtosecond pulses by coherently combining three channels with distinct spectra using spectral filters for splitting and combining. Partial spectral overlap by a linear detector and no spectral overlap by a TPA detector are justified based on different phase locking conditions. Although no spectral overlap method has better combining efficiency, the spectral gap between adjacent spectra resulting from the steepness mismatch of filters makes the combined pulse with unwanted pedestals. On the other hand, partial spectral overlap method can achieve 100% efficiency in principle if any two adjacent spectra are complementary. The scalable partial spectral overlap configuration with high combining efficiency and good pulse quality is thus a better choice to implement multi-channel pulse synthesis for defeating the gain narrowing limitations imposed on a single fiber amplifier.

7.2 Future Work

Like active coherent combining working in pulsed regime, passive coherent combining can also be extended to this regime using a saturable absorber. Although some experiment has been demonstrated [113], its dynamical behavior is still unknown. Our new propagation model therefore can be modified to explore this mode-locking and beam-combining dynamics of multi-element interferometric fiber laser structures [114] as well as the subsequent experimental investigations.

The scalable configuration of pulse coherent combining and pulse synthesis can also be augmented to larger array sizes. In particular, pulse synthesis can be arranged to coherently combine a wider spectral bandwidth from, for instance, the supercontinuum source and truly overcome the gain narrowing effect .

Since all the work done in this thesis is all-single-mode-fiber configurations for proof-of-principle demonstrations as we mentioned in the Introduction chapter, it can be replaced by large-core fibers such as CCC fibers to fully explore high energy/average power operations.

BIBLIOGRAPHY

1. T. Tajima and G.A. Mourou, "Zettawatt-exawatt lasers and their applications in ultrastrong-field physics," Phys. Rev. ST AB 5, 031301 (2002).

2. G.A. Mourou and T. Tajima, "More Intense, Shorter Pulses," Science 331, 41-42 (2011).

3. G.A. Mourou, D. Hulin, and A. Galvanauskas, "The Road to High Peak Power and High Average Power Lasers: Coherent Amplification Network (CAN)," AIP Conf. Proc. 827, 152-163 (2006).

4. C. Labaune, D. Hulin, A. Galvanauskas, and G.A. Mourou, "On the feasibility of a fiber-based inertial fusion laser driver," Opt. Commun. 281, 4075-4080 (2008).

5. H. Injeyan and G.D. Goodno, High-Power Laser Handbook, McGraw-Hill (2011).

6. R.A. Motes and R.W. Berdine, Introduction to High Power Fiber Lasers, Directed Energy Professional Society (2009).

7. T.Y. Fan, "Laser beam combining for high-power, high-radiance sources," IEEE J. Sel. Top. Quantum Electron. 11, 567-577 (2005).

8. S.M. Redmond, T.Y. Fan, D.J. Ripin, P.A. Thielen, J.E. Rothenberg, and G.D. Goodno, "Diffractive Beam Combining of a 2.5-kW Fiber Laser Array," Advanced Solid-State Photonics (ASSP) AM3A.1 (2012)

9. T.W. Wu, W.Z. Chang, A. Galvanauskas, and H.G. Winful, "Model for passive coherent beam combining in fiber laser arrays," Opt. Express 17, 19509-19518 (2009).

10. T.W. Wu, W.Z. Chang, A. Galvanauskas, and H.G. Winful, "Dynamical, bidirectional model for coherent beam combining in passive fiber laser arrays" Opt. Express 18, 25873-25886 (2010).

11. W.Z. Chang, T.W. Wu, H.G. Winful, and A. Galvanauskas, "Array size scalability of passively coherently phased fiber laser arrays," Opt. Express 18, 9634-9642 (2010).

12. L. Siiman, W.Z. Chang, T. Zhou, and A. Galvanauskas, “Coherent combining of 4 parallel chirped pulse femtosecond fiber amplifiers,” *In preparation for Opt. Express (2012).*

13. W.Z. Chang, T. Zhou, L. Siiman, and A. Galvanauskas, “Femtosecond pulse spectral synthesis in coherently combined multi-channel fiber chirped pulse amplifiers,” *In preparation for Opt. Express (2012).*

14. P.K. Cheo, A. Liu, and G. G. King, "A high-brightness laser beam from a phase-locked multicore Yb-doped fiber laser array," IEEE Photon. Technol. Lett. **13**, 439-441 (2001).

15. D. Sabourdy, V. Kermene, A. Desfarges-Berthelemot, L. Lefort, A. Barthelemy, C. Mahodaux, and D. Pureur, "Power scaling of fibre lasers with all-fibre interferometric cavity," Electron. Lett. **38**, 692-693 (2002).

16. A. Shirakawa, T. Saitou, T. Sekiguchi, and K. Ueda, "Coherent addition of fiber lasers by use of a fiber coupler," Opt. Express **10**, 1167-1172 (2002).

17. T.B. Simpson, A. Gavrielides, and P. Peterson, "Extraction characteristics of a dual fiber compound cavity," Opt. Express **10**, 1060-1073 (2002).

18. D. Sabourdy, V. Kermene, A. Desfarges-Berthelemot, L. Lefort, A. Barthelemy, P. Even, and D. Pureur, "Efficient coherent combining of widely tunable fiber lasers," Opt. Express **11**, 87-97 (2003).

19. A. Shirakawa, K. Matsuo, and K. Ueda, "Fiber laser coherent array for power scaling, bandwidth narrowing, and coherent beam direction control," in Conference on Fiber Lasers II, L. N. Durvasula, A. J. W. Brown, and J. Nilsson, eds. (San Jose, CA, 2005), pp. 165-174.

20. A.E. Siegman, "Resonant modes of linearly coupled multiple fiber laser structures",unpublished.

21. D. Kouznetsov, J. F. Bisson, A. Shirakawa, and K. Ueda, "Limits of coherent addition of lasers: Simple estimate," Opt. Review **12**, 445-447 (2005).

22. J.E. Rothenberg, "Passive coherent phasing of fiber laser arrays," Proc. SPIE 6873, (2008).

23. J.Q. Cao, J. Hou, Q.S. Lu, and X.J. Xu, "Numerical research on self-organized coherent fiber laser arrays with circulating field theory," J. Opt. Soc. Am. B **25**, 1187-1192 (2008).

24. J.L. Rogers, S. Peles, and K. Wiesenfeld, "Model for high-gain fiber laser arrays," IEEE J. Quantum Electron. **41**, 767-773 (2005).

25. W. Ray, J.L. Rogers, and K. Wiesenfeld, "Coherence between two coupled lasers from a dynamics perspective," Opt. Express **17**, 9357-9368 (2009).

26. H. Bruesselbach, D.C. Jones, M.S. Mangir, M. Minden, and J.L. Rogers, "Self-organized coherence in fiber laser arrays," Opt. Lett. **30**, 1339-1341 (2009).

27. V. Roy, M. Piche, F. Babin, and G.W. Schinn, "Nonlinear wave mixing in a multilongitudinal-mode erbium-doped fiber laser," Opt. Express **13**, 6791-6797 (2005).

28. S.P. Chen, Y.G. Li, K.C. Lu, and S.H. Zhou, "Efficient coherent combining of tunable erbium-doped fibre ring lasers," J. Opt. A **9**, 642-648 (2007).

29. T.B. Simpson, F. Doft, P.R. Peterson, and A. Gavrielides, "Coherent combining of spectrally broadened fiber lasers," Opt. Express **15**, 11731-11740 (2007).

30. E. Desurvire, "Anlysis of ebium-doped fiber amplifiers pumped in the I-4(15/2)-I-4(13/2) band," IEEE Photon.Technol. Lett. **1**, 293-296 (1989).

31. E. Desurvire, C.R. Giles, and J.R. Simpson, "Gain saturation effects in high-speed, multichannel erbium=doped fiber amplifiers at λ = 1.53 μm," J. Lightwave Technol. **7**, 2095-2104 (1989).

32. C.R. Giles, E. Desurvire, and J.R. Simpson, "Transient gain and cross talk in erbium-doped fiber amplifiers," Opt. Lett. **14**, 880-882 (1989).

33. D. Sabourdy, V. Kermene, A. Desfarges-Berthelemot, M. Vampouille, and A. Barthelemy, "Coherent combining of two Nd : YAG lasers in a Vernier-Michelson-type cavity," Appl. Phys. B **75**, 503-507 (2002).

34. Didomenico.M, "A single-frequency TEM00-mode gas laser with high output power," Appl. Phys. Lett. **8**, 20-22 (1966).

35. T. Wu, W. Chang, A. Galvanauskas, and H. G. Winful, unpublished.

36. H. Bruesselbach, D. C. Jones, M. S. Mangir, M. Minden, and J. L. Rogers, "Self-organized coherence in fiber laser arrays," Opt. Lett. 30, 1339-1341 (2005).

37. D. Sabourdy, V. Kermene, A. Desfarges-Berthelemot, L. Lefort, A. Barthelemy, P. Even, and D. Pureur, "Efficient coherent combining of widely tunable fiber lasers," Opt. Express 11, 87-97 (2003).

38. A. Shirakawa, K. Matsuo, and K. Ueda, "Fiber laser coherent array for power scaling, bandwidth narrowing, and coherent beam direction control," in Conference on Fiber Lasers II, L. N. Durvasula, A. J. W. Brown, and J. Nilsson, eds. (San Jose, CA, 2005), pp. 165-174.

39. A. Shirakawa, T. Saitou, T. Sekiguchi, and K. Ueda, "Coherent addition of fiber lasers by use of a fiber coupler," Opt. Express 10, 1167-1172 (2002).

40. J.Q. Cao, J. Hou, Q.S. Lu, and X.J. Xu, "Numerical research on self-organized coherent fiber laser arrays with circulating field theory," J. Opt. Soc. Am. B 25, 1187-1192 (2008).

41. D. Kouznetsov, J.F. Bisson, A. Shirakawa, and K. Ueda, "Limits of coherent addition of lasers: Simple estimate," Opt. Rev. 12, 445-447 (2005).

42. W. Ray, J. L. Rogers, and K. Wiesenfeld, "Coherence between two coupled lasers from a dynamics perspective," Opt. Express 17, 9357-9368 (2009).

43. J.L. Rogers, S. Peles, and K. Wiesenfeld, "Model for high-gain fiber laser arrays," IEEE J Quantum Electron. 41, 767-773 (2005).

44. K. Wiesenfeld, S. Peles, and J.L. Rogers, "Effect of Gain-Dependent Phase Shift on Fiber Laser Synchronization," IEEE J Sel. Top. Quantum Electron. 15, 312-319 (2009).

45. G.P. Agrawal, "Nonlinear fiber optics, third edition," (Academic Press, 2001), pp. 263-264.

46. A.E. Siegman, "Lasers," (University Science Books (January 1986)), pp. 485-487.

47. A. Yariv, "Photonics: Optical Electronics in Modern Communications, 6th Edition," (Oxford University Press, USA, 2007), pp. 563-565.

48. V. Roy, M. Piche, F. Babin, and G.W. Schinn, "Nonlinear wave mixing in a multilongitudinal-mode erbium-doped fiber laser," Opt. Express 13, 6791-6797 (2005).

49. D. Hollenbeck, and C.D. Cantrell, "Parallelizable, bidirectional method for simulating optical-signal propagation," J Lightwave Technol. 27, 2140-2149 (2009).

50. J. Kanka, "Numerical-simulation of subpicosecond soliton formation in a nonlinear coupler laser," Opt. Lett. 19, 1873-1875 (1994).

51. E. Marti-Panameno, L.C. Gomez-Pavon, A. Luis-Ramos, M.M. Mendez-Otero, and M.D. I. Castillo, "Self-mode-locking action in a dual-core ring fiber laser," Opt. Commun. 194, 409-414 (2001).

52. B.N. Upadhyaya, U. Chakravarty, A. Kuruvilla, A.K. Nath, M.R. Shenoy, and K. Thyagarajan, "Effect of steady-state conditions on self-pulsing characteristics of Yb-doped cw fiber lasers," Opt. Commun. 281, 146-153 (2008).

53. D. Sabourdy, V. Kermene, A. Desfarges-Berthelemot, M. Vampouille, and A. Barthelemy, "Coherent combining of two Nd : YAG lasers in a Vernier-Michelson-type cavity," Appl. Phys. B-Lasers. O. 75, 503-507 (2002).

54. E.J. Bochove, "Effect of nonlinear phase on the passive phase locking of an array of fiber lasers of random lengths," in Integrated Photonics and Nanophotonics Research and Applications (IPNRA) (Honolulu, Hawaii, 2009).

55. C.J. Corcoran, and K.A. Pasch, "Output phase characteristics of a nonlinear regenerative fiber amplifier," IEEE J Quantum Electron. 43, 437-439 (2007).

56. B.S. Wang, E. Mies, M. Minden, and A. Sanchez, "All-fiber 50 W coherently combined passive laser array," Opt. Lett. 34, 863-865 (2009).

57. H. Bruesselbach, M. Minden, J.L. Rogers, D. C. Jones, and M.S. Mangir, "200 W self-organized coherent fiber arrays," in 2005 Conference on Lasers & Electro-Optics (2005), pp. 532-534.

58. A.E. Siegman, "Resonant modes of linearly coupled multiple fiber laser structures," http://www.stanford.edu/~siegman/Coupled%20Fiber%20Lasers/coupled_fiber_modes.pdf, unpublished (2004).

59. P.K. Cheo, A. Liu, and G.G. King, "A high-brightness laser beam from a phase-locked multicore Yb-doped fiber laser array," IEEE Photon. Tech. Lett. 13, 439-441 (2001).

60. A. Shirakawa, K. Matsuo, and K. Ueda, "Fiber laser coherent array for power scaling, bandwidth narrowing, and coherent beam direction control," Proc. of SPIE 5709, 165-174 (2005).

61. M.L. Minden, H. Bruesselbach, J.L. Rogers, M.S. Mangir, D.C. Jones, G.J. Dunning, D.L. Hammon, A.J. Solis, and L. Vaughan, "Self-organized coherence in fiber laser arrays," Proc. SPIE 5335, 89-97 (2004).

62. C.J. Corcoran and F. Durville, "Experimental demonstration of a phase-locked laser array using a self-Fourier cavity," App. Phys. Lett. 86, 201118 (2005).

63. J. Cao, J. Hou, Q. Lu, and X. Xu, "Numerical research on self-organized coherent fiber laser arrays with circulating field theory," J. Opt. Soc. Am. B, 25, 1187-1192 (2008).

64. A.E. Siegman, "Resonant modes of linearly coupled multiple fiber laser structures," unpublished (2004).

65. D. Kouzentsov, J. Bisson, A. Shirakawa, and K. Ueda, "Limits of Coherent Addition of Lasers: Simple Estimate," Optical Review 12, 445-447 (2005).

66. J.E. Rothenberg, "Passive coherent phasing of fiber laser arrays," Proc. of SPIE 6873 (2008).

67. M.Khajavikhan and J.R. Leger, "Modal Analysis of Path Length Sensitivity in Superposition Architectures for Coherent Laser Beam Combining," IEEE J. Sel. Topics Quantum Electron. 15(2), 281-290 (2009).

68. C.J. Corcoran and F. Durville, "Passive Phasing in a Coherent Laser Array," IEEE J. Sel. Topics Quantum Electron. 15(2), 294-300 (2009).

69. K. Krushelnick, E.L. Clark, F.N. Beg, A.E. Dangor, Z. Najmudin, P.A. Norreys, M. Wei, and M. Zepf, "High intensity laser-plasma sources of ions-physics and future applications," Plasma Physics and Controlled Fusion **47**, B451-B463 (2005).

70. E. Seise, A. Klenke, J. Limpert, and A. Tünnermann, "Coherent addition of fiber-amplified ultrashort laser pulses," Opt. Express **18**, 27827-27835 (2010).

71. L. Daniault, M. Hanna, L. Lombard, Y. Zaouter, E. Mottay, D. Goular, P. Bourdon, F. Druon, and P. Georges, "Coherent beam combining of two femtosecond fiber chirped-pulse amplifiers," Opt. Lett. **36**, 621-623 (2011).

72. T.M. Shay, V. Benham, J.T. Baker, A.D. Sanchez, D. Pilkington, and C.A. Lu, "Self-synchronous and self-referenced coherent beam combination for large optical arrays," IEEE Journal of Selected Topics in Quantum Electronics **13**, 480-486 (2007).

73. T.M. Shay, "Theory of electronically phased coherent beam combination without a reference beam," Opt. Express **14**, 12188-12195 (2006).

74. T. Eidam, S. Hanf, E. Seise, T.V. Andersen, T. Gabler, C. Wirth, T. Schreiber, J. Limpert, and A. Tünnermann, "Femtosecond fiber CPA system emitting 830 W average output power," Opt. Lett. **35**, 94-96 (2010).

75. S.J. Augst, T.Y. Fan, and A. Sanchez, "Coherent beam combining and phase noise measurements of ytterbium fiber amplifiers," Opt. Lett. **29**, 474-476 (2004).

76. H. Tünnermann, J.H. Pöld, J. Neumann, D. Kracht, B. Willke, and P. Weßels, "Beam quality and noise properties of coherently combined ytterbium doped single frequency fiber amplifiers," Opt. Express **19**, 19600-19606 (2011).

77. G.D. Goodno, C.C. Shih, and J.E. Rothenberg, "Perturbative analysis of coherent combining efficiency with mismatched lasers," Opt. Express **18**, 25403-25414 (2010).

78. G.A. Mourou, T. Tajima, and S.V. Bulanov, "Optics in the relativistic regime," Rev. Mod. Phys. **78**, 309-371 (2006).

79. I.N. Ross, J.L. Collier, P. Matousek, C.N. Danson, D. Neely, R.M. Allott, D.A. Pepler, C. Hernandez-Gomez, and K. Osvay, "Generation of terawatt pulses by use of optical parametric chirped pulse amplification," Appl. Opt. **39**, 2422-2427 (2000).

80. C.X. Yu, S.J. Augst, S.M. Redmond, K.C. Goldizen, D.V. Murphy, A. Sanchez, and T.Y. Fan, "Coherent combining of a 4 kW, eight-element fiber amplifier array," Opt. Lett. **36**, 2686-2688 (2011).

81. T. Y. Fan "The effect of amplitude (power) variations on beam combining efficiency for phased arrays", IEEE J. Sel. Topics Quantum Electron., **15**, 291 (2009).

82. E.W. Gaul, M. Martinez, J. Blakeney, A. Jochmann, M. Ringuette, D. Hammond, T. Borger, R. Escamilla, S. Douglas, W. Henderson, G. Dyer, A. Erlandson, R. Cross, J. Caird, C. Ebbers, and T. Ditmire, "Demonstration of a 1.1 petawatt laser based on a hybrid optical parametric chirped pulse amplification/mixed Nd:glass amplifier," Appl. Opt. **49**, 1676-1681 (2010).

83. R. Uberna, A. Bratcher, and B.G. Tiemann, "Coherent polarization beam combination," IEEE J. Quantum Electron. **46**(8), 1191–1196 (2010).

84. E.C. Cheung, J.G. Ho, G.D. Goodno, R.R. Rice, J. Rothenberg, P. Thielen, M. Weber, and M. Wickham, "Diffractive-optics-based beam combination of a phase-locked fiber laser array," Opt. Lett. **33**, 354-356 (2008).

85. R. Uberna, A. Bratcher, T.G. Alley, A.D. Sanchez, A.S. Flores, and B. Pulford, "Coherent combination of high power fiber amplifiers in a two-dimensional re-imaging waveguide," Opt. Express **18**, 13547-13553 (2010).

86. M. Tempus, W. Luthy, and H.P. Weber, "Coherent recombination of laser beams with interferometrical phase control," Appl. Phys. B: Photophys. Laser Chem. **56**, 79 (1993).

87. D.J. Richardson, J. Nilsson, and W.A. Clarkson, "High power fiber lasers: current status and future perspectives [Invited]," J. Opt. Soc. Am. B **27**, B63-B92 (2010).

88. W. Liang, N. Satyan, F. Aflatouni, A. Yariv, A. Kewitsch, G. Rakuljic, and H. Hashemi, "Coherent beam combining with multilevel optical phase-locked loops," J. Opt. Soc. Am. B **24**, 2930-2939 (2007).

89. C.D. Nabors, "Effects of phase errors on coherent emitter arrays," Appl. Opt. **33**, 2284-2289 (1994).

90. A. Maréchal, "Étude des effets combinés de la diffraction et des aberrations géometriques sur l'image d'un point lumineux," Rev. Opt. Theor. Instrum. **26**, 257-277 (1947).

91. G.D. Goodno, H. Komine, S.J. McNaught, S.B. Weiss, S. Redmond, W. Long, R. Simpson, E.C. Cheung, D. Howland, P. Epp, M. Weber, M. McClellan, J. Sollee, and H. Injeyan, "Coherent combination of high-power, zigzag slab lasers," Opt. Lett. **31**, 1247-1249 (2006).

92. M.A. Vorontsov, G.W. Carhart, and J.C. Ricklin, "Adaptive phase-distortion correction based on parallel gradient-descent optimization," Opt. Lett. **22**, 907-909 (1997).

93. P. Zhou, Z. Liu, X. Wang, Y. Ma, H. Ma, X. Xu, and S. Guo, "Coherent beam combining of fiber amplifiers using stochastic parallel gradient descent algorithm and its application," IEEE J. Sel. Top. Quantum Electron. **15**, 248-256 (2009).

94. T.Y. Fan, "Laser beam combining for high-power, high-radiance sources," IEEE J. Sel. Top. Quantum Electron **11**, 567-577 (2005).

95. G.D. Goodno, C.P. Asman, J. Anderegg, S. Brosnan, E.C. Cheung, D. Hammons, H. Injeyan, H. Komine, W.H. Long, M. McClellan, S.J. McNaught, S. Redmond, R. Simpson, J. Sollee, M. Weber, S.B. Weiss, and M. Wickham, "Brightness-scaling potential of actively phase-locked solid-state laser arrays," IEEE J. Sel. Top. Quantum Electron **13**, 460–472 (2007).

96. G.J. Swanson, J.R. Leger, and M. Holz, "Aperture filling of phase-locked laser arrays," Opt. Lett. **12**, 245-247 (1987).

97. T. Schreiber, D. Schimpf, D. Müller, F. Röser, J. Limpert, and A. Tünnermann, "Influence of pulse shape in self-phase-modulation-limited chirped pulse fiber amplifier systems," J. Opt. Soc. Am. B 24, 1809-1814 (2007).

98. J. Limpert, F. Roser, D.N. Schimpf, E. Seise, T. Eidam, S. Hädrich, J. Rothhardt, C.J. Misas, and A. Tünnermann, "High Repetition Rate Gigawatt Peak Power Fiber Laser Systems: Challenges, Design, and Experiment," IEEE J. Sel. Top. Quantum Electron. **15**, 159 (2009).

99. W.H. Renninger, A. Chong, and F.W. Wise, "Pulse Shaping and Evolution in Normal-Dispersion Mode-Locked Fiber Lasers," IEEE J. Sel. Top. Quantum Electron. **18**, 389-398 (2012).

100. J. Anderegg, S. Brosnan, M. Weber, H. Komine, and M. Wickham, "8-W coherently phased 4-element fiber array," Proc. SPIE, **4974**, 1–6 (2003).

101. E.C. Cheung, M. Weber, and R.R. Rice, "Phase Locking of a Pulsed Fiber Amplifier," in Advanced Solid-State Photonics (2008, paper WA2.

102. M. Yamada, T. Kanamori, Y. Terunuma, K. Oikawa, M. Shimizu, S. Sudo, and K. Sagawa, "Fluoride-based erbium-doped fiber amplifier with inherently flat gain spectrum," IEEE Photon. Technol. Lett. **8**, 882–884 (1996).

103. H. Masuda and S. Kawai, “Wide-band and gain-flattened hybrid fiber amplifier consisting of an EDFA and a multiwavelength pumped Raman amplifier,” IEEE Photonics Technol. Lett. **11**, 647-649 (1999).

104. Y.B. Lu, P.L. Chu, A. Alphones, and P. Shum, “A 105-nm ultrawide-band-gain-flattened amplifier combining C- and L-band dual-core EDFAs in a parallel configuration,” IEEE Photonics Technol. Lett. 16, 1640-1642 (2004).

105. M. Harurnoto, M. Shigehara, and H. Suganurna, “Gain-flattening filter using long-period fiber gratings,” J. Lightwave Technol. **20**, 1027-1033 (2002).

106. S. K. Liaw, K. P. Ho, and S. Chi, “Dynamic power-equalized EDFA module based on strain tunable fiber Bragg gratings,” IEEE Photon. Technol. Lett. **11**, 797–799 (1999).

107. S. K. Yun, B. W. Lee, H. K. Kim, and B. Y. Kim, "Dynamic erbium-doped fiber amplifier based on active gain flattening with fiber acoustooptic tunable filter", IEEE Photon. Technol. Lett. **11**, 1229 - 1231 (1999).

108. K. Inoue, T. Kominato, and H. Toba, “Tunable gain-equalization using a Mach–Zehnder optical filter in multistage amplifiers,” IEEE Photon. Technol. Lett. 3, 718-720 (1991).

109. R.K. Shelton, L.S. Ma, H.C. Kapteyn, M.M. Murnane, J.L. Hall, and J. Ye, “Phase-coherent optical pulse synthesis from separate femtosecond lasers,” Science **293**, 1286-1289 (2001).

110. G. Krauss, S. Lohss, T. Hanke, A. Sell, S. Eggert, R. Huber, and A. Leitenstorfer, “Synthesis of a single cycle of light with compact erbium-doped fibre technology,” Nature Photon. **4**, 33-36 (2010).

111. S.W. Huang, G. Cirmi, J. Moses, K.H. Hong, S. Bhardwaj, J.R. Birge, L.J. Chen, E. Li, B.J. Eggleton, G. Cerullo, and F.X. Kartner, “High-energy pulse synthesis with sub-cycle waveform control for strong-field physics,” Nature Photon. **5**, 475-479 (2011).

112. A. Klenke, E. Seise, S. Demmler, J. Rothhardt, S. Breitkopf, J. Limpert, and A. Tünnermann, “Coherently-combined two channel femtosecond fiber CPA system producing 3 mJ pulse energy,” Opt. Express **19**, 24280-24285 (2011).

113. J. Lhermite, D. Sabourdy, A. Desfarges-Berthelemot, V. Kermene, A. Barthelemy, and J.L. Oudar, "Tunable high-repetition-rate fiber laser for the generation of pulse trains and packets," Opt. Express 32, 1734-1736 (2007).

114. C. Zhang, W.Z. Chang, A. Galvanauskas, and H.G. Winful, "Simultaneous Passive Coherent Combining and Mode Locking in Fiber Laser Arrays," *Submitted to Opt. Express (2012).*